CZECH TECHNICAL UNIVERSITY IN PRAGUE

Faculty of Nuclear Sciences and Physical Engineering

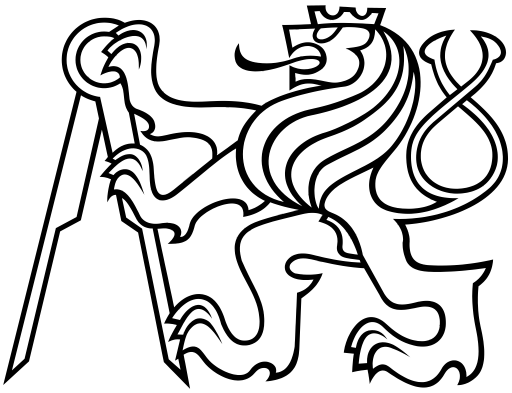

Doctoral Thesis

Laser-generated short-wavelength coherent sources and their applications

2023

Martin Albrecht

Bibliographic Entry

Title of Dissertation:	**Laser-generated short-wavelength coherent sources and their applications**
Author:	Ing. Martin Albrecht
	Czech Technical University in Prague (CTU),
	Faculty of Nuclear Sciences and Physical Engineering (FNSPE),
	Department of Physical Electronics
Degree programme:	Applications of Natural Sciences
Field of study:	Physical Engineering
Supervisor:	doc. Ing. Ladislav Pína, DrSc.
	CTU, FNSPE, Department of Physical Electronics
Supervisor-Specialist:	Ing. Jaroslav Nejdl, Ph.D.
	CTU, FNSPE, Department of Physical Electronics
	Extreme Light Infrastructure ERIC (ELI ERIC)
Academic Year:	2023
Number of Pages:	123
Key words:	Plasma-based soft X-Ray lasers (SXRLs), Spatial coherence retrieval, HHG Beamline, EUV coherent diffractive imaging (CDI), EUV ptychography

Bibliografický záznam

Název disertační práce:	**Laserem generované zdroje koherentního krátkovlnného záření a jejich aplikace**
Autor:	Ing. Martin Albrecht České vysoké učení technické v Praze (ČVUT), Fakulta jaderná a fyzikálně inženýrská (FJFI), Katedra fyzikální elektroniky
Studijní program:	Aplikace přírodních věd
Studiní obor:	Fyzikální inženýrství
Školitel:	doc. Ing. Ladislav Pína, DrSc. ČVUT, FJFI, Katedra fyzikální elektroniky
Školitel-Specialista:	Ing. Jaroslav Nejdl, Ph.D. ČVUT, FJFI, Katedra fyzikální elektroniky Extreme Light Infrastructure ERIC (ELI ERIC)
Akademický rok:	2023
Počet stran:	123
Klíčová slova:	Plazmové lasery měkkého rentgenové záření (SXRLs), rekonstrukce prostorové koherence, HHG Beamline, EUV koherentní difraktivní zobrazování (CDI), EUV ptychografie

I hereby declare that this thesis was carried out by me. I also declare that all the sources of information used to complete the thesis are included in the list of references.

Prague, 25.8.2023 Martin Albrecht

Abstract

This doctoral thesis focuses on the development of novel techniques for investigating the coherence characteristics of laser-driven short-wavelength radiation. Additionally, the thesis is devoted to the application of this radiation in the field of coherent diffractive imaging.

One of the laser-driven sources of coherent soft X-rays is a plasma-based X-ray laser, operating on the principle of amplified spontaneous emission (ASE) at transitions of multiply ionized atoms. However, the radiation emitted by such a source possesses only partial coherence, emphasizing the significance of characterizing its coherence for further applications.

Within this work, a study of the far-field intensity profile of a molybdenum plasma-based X-ray laser was performed. By employing a statistical analysis of the intensity pattern, which allows the estimation of the number of longitudinal coherence modes, and utilizing prior knowledge of the spectral profile of the radiation, we successfully estimated the duration of the X-ray laser pulse.

A novel method was also developed to characterize the spatial coherence of a plasma-based X-ray laser. This method relies on diffraction through a non-redundant mask of simple apertures. By designing the mask appropriately, the spatial coherence function of each laser pulse can be measured. Our method was experimentally verified using the plasma-based Zn X-ray laser.

An alternative source of short-wavelength radiation, utilized for experimental investigation in this study, involves high-order harmonic generation. Using an appropriate monochromatizing device, a single harmonic frequency can be isolated from the generated radiation and utilized for monochromatic coherent diffractive microscopy. The successful image reconstruction of a binary sample was demonstrated using the 21-st high harmonic frequency.

Another lensless imaging method is ptychographic coherent diffractive imaging, which offers greater universality. This technique is demonstrated in the work with a variant utilizing a beam composed of all high harmonics, eliminating the need for monochromatization and considerably simplifying the experimental setup. In this configuration, monochromatization is substituted by an algorithm capable of reconstructing information from the recorded diffraction pattern formed by multiple harmonic frequencies.

Abstrakt

Tato disertační práce se zabývá návrhem nových metod pro studium koherenčních vlastností laserem čerpaných zdrojů krátkovlnného záření a jejich aplikací v oblasti koherentního difraktivního zobrazení.

Jedním z laserem čerpaných zdrojů koherentního měkkého rentgenového záření je plazmový rentgenový laser, který využívá zesílené spontánní emise (ASE) na přechodech energetických hladin mnohonásobně ionizovaných atomů. Záření emitované takovýmto zdrojem je však pouze částečně koherentní, a proto je znalost jeho koherence důležitá s ohledem na další aplikace.

V první části této práce byl zkoumán intenzitní profil molybdenového plazmového rentgenového laseru ve vzdálené zóně, kde bylo ukázáno, že pomocí intenzitní statistické analýzy lze nalézt odhad délky laserového impulzu za předpokladu znalosti jeho spektrálního profilu.

Rovněž byla navržena nová metoda zkoumající prostorovou koherenci plazmového rentgenového laseru, která je založená na difrakci na neredundantní masce složené z jednoduchých apertur. Pomocí vhodného návrhu masky může být prostorová koherenční funkce změřena během jednoho laserového impulzu. Metoda byla úspěšně otestována na změřených experimentálních datech plazmového zinkového rentgenového laseru.

Alternativním zdrojem krátkovlnného záření, který byl rovněž použit v této práci, je generace vysokých harmonických frekvencí.Vhodným monochromatizačním zařízením lze zvolit pouze jedinou harmonickou frekvenci a realizovat koherentní difraktivní mikroskopii (CDI) s monochromatický svazkem. Úspěšná rekonstrukce binárního testovacího vzorku je demonstrována s 21. harmonickou frekvencí.

Další metodou bezčočkového zobrazení je takzvaná ptychografie, která je mnohem univerzálnější a je schopna překonat některá omezení předchozí (CDI) metody. Tato technika je v práci demonstrována ve spojení se svazkem vysokých harmonických bez nutnosti monochromatizace, čímž se značeně zjednodušuje celá experimentální sestava. Monochromatizace je v tomto případě nahrazena algoritmem, který je schopen rekonstruce ze záznamu difrakčního obrazce vytvořeného z více harmonických frekvencí.

Dedicated to my parents, Josef and Hana,
for their lifelong support.

Acknowledgments

I would like to thank to *L. Pína* and *J. Nejdl* for supervising this thesis, suggestions for text improvement, and for their invaluable support, without whom this work would not have been possible. Next, I would like to express my gratitude to *D.-D. Mai* for his invaluable assistance in operating the multi-color ptychography algorithm and for his guidance in making my own CDI algorithm functional. I would also like to thank *Eva Klimešová* for her help with the automated acquisition during ptychography, and *Smijesh N. Achary* for the assistance provided during the long shifts of ptychography data acquisitions.

My further thanks are dedicated to the HHG Beamline team, of which I am also a part: *O. Hort*, *O. Finke*, *M. Staněk* and *L. Jurkovičová*, for the successful experiments and great results we have achieved together from the initiation of HHG Beamline operations. I also extend my gratitude to other colleagues of X-ray group: *J. Vábek*, *U. Chaulagain*, *M. Lamač*, *M. Raclavský*, *Y. Pulnova*, *K. R. Hemantha*, for team work, friendly talks and the fun we have enjoyed together.

I would like to express my acknowledgment to the entire team that was responsible for the operation of the PALS laboratory during my experimental measurements: *M. Kozlová*, *M. Krůs*, *T. Medřík*, *J. Golasowski*, and *J. Hřebíček*.

Last but not least, I would like to thank my close family members for their support and the trust they had in me, specifically my parents *Josef* and *Hana*, and my sister *Hana* along with her husband *Jan* and their children *Adélka* and *Tomášek*.

Contents

1 Introduction

A significant advancement in extreme ultraviolet (EUV/XUV) radiation sources has been achieved over the past few decades [1], driven by the demand for novel scientific and semiconductor industry applications [2]. Short pulses of short-wavelength radiation are required to study the nature on smaller spatial scales and shorter timescales, as well as to investigate the atomic physics of inner-shell electrons. Initially, incoherent sources suitable for EUV lithography were developed [3]. Subsequently, as applications expanded from visible light to the EUV spectral region, the requirement for coherent sources gained significance. Currently, a unique source of EUV radiation, X-ray free electron lasers (XFELs) [4], provides high-flux ultrashort pulses, which can be fully coherent. However, due to their high cost and limited availability, smaller laboratory sources such as high-harmonic generation or plasma-based X-ray lasers [5,6] are gaining importance.

The main goals of this thesis include coherence studies of particular laser-driven EUV sources using newly proposed techniques. Additionally, the thesis also focuses on the application of EUV radiation in the field of coherent diffractive imaging (CDI) which offers a lensless approach to imaging, eliminating the need for conventional imaging optics. This not only avoids optical aberrations and reduces the necessity for expensive EUV optics but also simplifies the experimental setup.

In the introductory sections of this doctoral thesis, we briefly discuss the most commonly used partially coherent EUV sources relevant to research involving short-wavelength light-matter interactions. Additionally, we introduce the theory of coherence of electromagnetic radiation, the free-space propagation of both fully and partially coherent light, and the theory of coherent diffractive imaging. These theoretical concepts were essential for evaluating the experimental results presented in this thesis and for developing algorithms for partially and fully coherent field propagation.

Next, in this work, we introduce a novel approach to estimating the pulse duration of partially coherent soft X-ray pulses, utilizing information obtained from a far-field intensity pattern. The method, which was published in [7], is based on the analysis of intensity statistics at a single point in space and time. This method was applied to estimate the pulse duration of the laser-driven nickel-like molybdenum soft X-ray laser, which relies on amplified spontaneous emission from a narrow plasma column and emits at a wavelength of 18.9 nm.

We also introduce another novel method for single-shot spatial coherence measurement, with results that were submitted for publication at the time when this thesis was finalized. The method has been successfully demonstrated within the soft X-ray spectral range. Our approach is based on a far-field diffraction pattern obtained from a binary transmission mask containing a well-defined non-redundant array of elementary apertures. The coherence function is then retrieved through an iterative algorithm similar to the one employed in [8], and coherent diffractive imaging techniques [9–11]. This algorithm, optimized for our specific conditions, was developed by the author of this thesis, tested through simulations, and utilized to evaluate the experimental results of a laser-driven zinc plasma soft X-ray laser.

The final objective of this doctoral thesis is to experimentally realize EUV coherent diffractive imaging and multi-color ptychography on the HHG beamline at the ELI Beamlines[1], thereby validating its feasibility for future advanced diffraction-based imaging techniques. In the context of CDI, a phase retrieval algorithm based on Fienup's Hybrid Input Output approach was implemented by the author of this thesis and successfully tested through experimental measurements. Moreover, successful demonstration of multi-color ptychography was achieved using an algorithm developed at the University of California [12, 13].

[1] ELI Beamlines Facility is a laser research center and part of The Extreme Light Infrastructure ERIC, a pan-European research Infrastructure

2 Overview of current partially coherent EUV sources

There are numerous methods available for generating EUV radiation based on various physical principles. This chapter provides a brief overview of the most commonly used partially coherent EUV sources. The radiation emitted from these sources possesses different properties, which are briefly discussed as well.

2.1 Synchrotron radiation

In modern scientific research, synchrotron radiation plays a crucial role as it provides electromagnetic radiation in a wide range of wavelengths, from terahertz to X-rays [1, 14]. This radiation is produced when charged particles, typically electrons, are accelerated to nearly the speed of light and forced to travel in curved trajectories (are accelerating) by strong magnetic fields.

In principle, synchrotron radiation is produced by three types of commonly used magnetic structures [1,15]: bending magnets, undulators, and wigglers. Bending magnets guide accelerated particles along a single curved trajectory, while undulators and wigglers have periodic magnetic fields, causing particles to oscillate. The main difference between undulators and wigglers lies in the strength of their magnetic fields. Wigglers have stronger magnetic fields, leading to larger amplitude oscillations. As a consequence, the resulting spectrum is similar to bending magnets but shows a larger photon flux and is shifted towards shorter wavelengths.

In the case of the bending magnet, we can estimate the divergence of the emitted radiation of relativistic charged particles by considering Lorentz transformations [1]. The upper limit of the half-cone divergence angle θ is given by the following equation

$$\tan\theta \approx \theta \simeq \frac{1}{2\gamma} \quad , \tag{2.1}$$

where γ is the relativistic Lorentz factor. Next, it is possible to approximately determine the wavelength of the radiation based on Heisenberg's uncertainty principle. It can be shown [1] that the inaccuracy of the measured photon energy must satisfy the

relation

$$\Delta E \geq \frac{2e\hbar B\gamma^2}{m_e} \quad , \tag{2.2}$$

where e is the charge of the electron, m_e is the mass of the electron, B is the magnetic field of the bending magnet, and $\hbar$ is reduced Planck's constant. By substituting typical values where γ reaches several thousand and $B \geq 1$ T, we can obtain that emitted photons energy is in the order of keV (nanometer wavelengths).

The schematic diagram illustrating the evolution from the first synchrotron radiation devices to modern ones is shown in Fig. 2.1. Initially, electrons are accelerated by a linear accelerator (linac), and then their energy is further increased by a circular accelerator (booster) to a speed close to the speed of light. In the last segment (storage ring), the energy of the particles is maintained constant, and the emitted radiation (when particles lose energy) is distributed to individual laboratories. The acceleration of the particles is achieved using strong electric fields, while a system of magnets controls their trajectory.

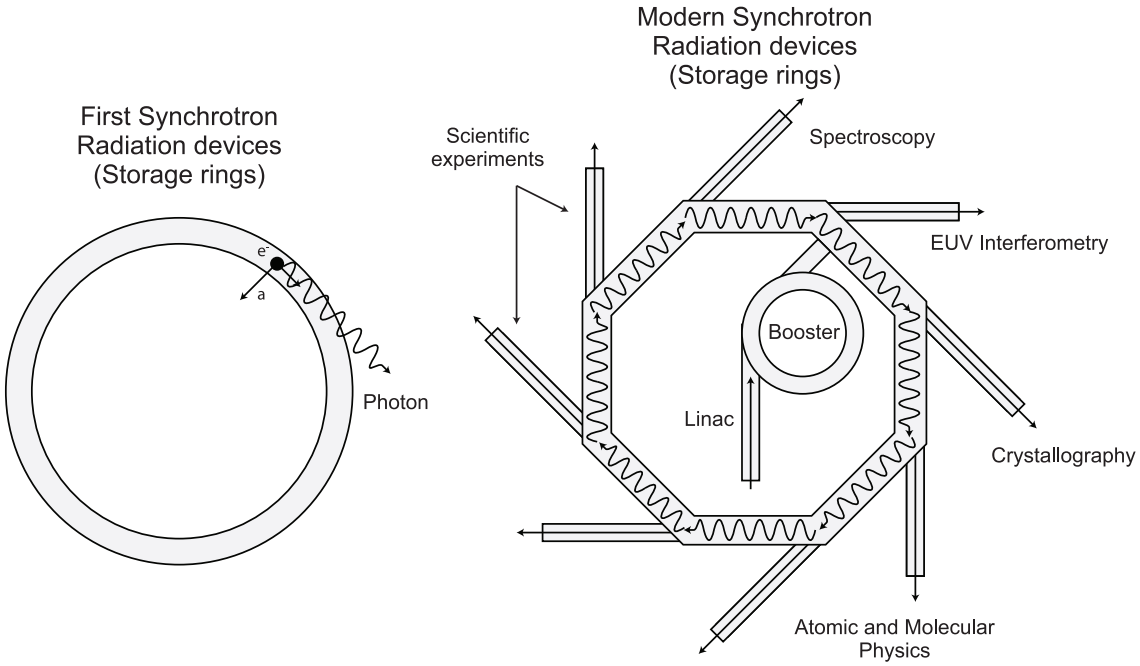

Fig. 2.1: The schematic shows the evolution from the first synchrotron radiation devices to modern ones. In the past, radiation was mainly generated by bending magnets in circular storage rings. In modern devices, storage rings consist of many straight sections with undulators and wigglers.

To date, storage rings (SRs) have made significant progress and have advanced to their fourth generation, known as diffraction-limited SRs [16, 17]. Third-generation storage rings (3GSRs) are commonly based on lattice[1] designs with either double-bend

[1]The lattice is the system of magnetic lenses responsible for guiding and focusing an electron beam.

achromat (DBA) or triple-bend achromat (TBA). On the other hand, fourth-generation storage rings (4GSRs) utilize multi-bend achromat (MBA) lattices, enabling the production of X-ray radiation with high brilliance and flux [17]. The X-ray beams generated in these advanced storage rings exhibit remarkable spatial coherence. Additionally, they possess a narrow energy spread of the electron bunches, leading to exceptional spectral resolution.

The main advantages of synchrotron radiation include its high average brightness, which is challenging to achieve using other methods, and the small divergence of the beam. The generated pulses typically have lengths in the order of tens of picoseconds. However, synchrotrons have some main disadvantages, such as their high cost and large size, with dimensions in the order of hundreds of meters.

2.1.1 Free electron laser (FEL)

The operation of a free electron laser involves the acceleration of electrons, similar to synchrotron radiation devices and many other particle accelerators [1, 18, 19]. These accelerated electrons then enter an undulator, where they follow oscillations within a periodic magnetic field. As a result of these oscillations, electron microbunches are formed. Thus the radiation is amplified by the self-amplified spontaneous emission (SASE) and all created microbunches emit correlated radiation. Output radiation power for SASE is scaled as squared number of emitting electrons N_e^2. The undulator is a device composed from magnets with an alternating magnetic field described by the undulator period λ_u. The FEL scheme is shown in Fig. 2.2.

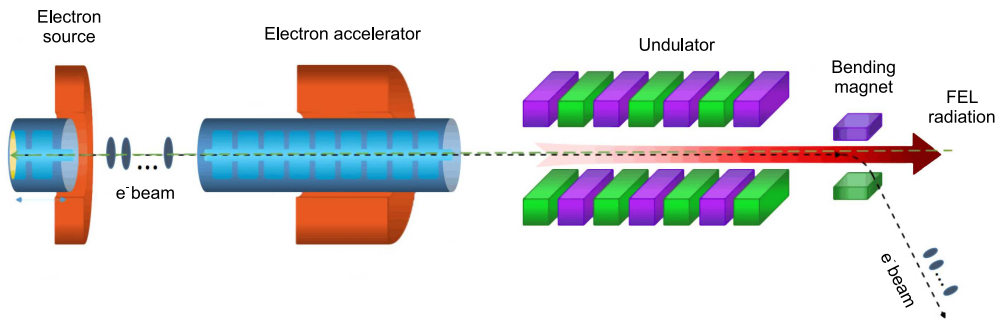

Fig. 2.2: The schematic of the FEL, where electrons are accelerated by a conventional way and then undergo oscilations in the undulator section inducing an X-ray pulse to build up. (Adapted from [20])

The resulting emitted spectrum is primarily influenced by two significant effects: the relativistic shift of the wavelength and the Doppler effect. The wavelength of the

undulator radiation can be determined using the undulator equation [1,19], which takes into account the harmonic frequencies of the n-th order. By considering these effects, the wavelength of the undulator radiation can be derived as

$$\lambda_n = \frac{\lambda_u}{2\gamma^2 n}\left(1 + \frac{K^2}{2} + \gamma^2\theta^2\right) \quad , \tag{2.3}$$

where θ is the off-axis angle of the observation measured from direction of the beam propagation, and K is the magnetic strength parameter. In the case of undulator $(K < 1)$, the spectral linewidth [1] is narrowing with number of magnetic periods N according

$$\frac{\Delta\lambda_n}{\lambda_n} = \frac{1}{nN} \quad , \tag{2.4}$$

which implies a very narrow spectral line as the number of periods increases. The main advantage of FELs are a high beam brightness, small beam divergence, short pulse duration, and tunability [1,4,21].

Coherence properties generally depend on a process of generation. While spatial coherence is very high, the temporal coherence for the free electron laser is not high, mainly due to a startup amplification from a stochastic origin known as self-amplified spontaneous emission. However, this temporal coherence can be significantly improved by using seeding radiation tuned to the resonance FEL frequency [22], resulting in full coherence (both spatial and temporal).

2.2 High harmonic generation (HHG)

One currently very promising approach to a compact coherent EUV source is a process of the high harmonic generation. This kind of source is based on a nonlinear interaction between a linearly polarized strong laser field and a gas medium. Although the technique of the HHG in solids was published during last years [23], the HHG generation is usually performed in a gas cell or gas jet which is placed inside a vacuum chamber. An appropriate nonlinear gas medium typically consists of inert gases such as Ar, Ne or He with a pressure of the order of tens of mbar. Noble gases are particularly suitable because of their high ionization potential that enables presence of non-ionized atoms in high laser intensities.

The generation of EUV radiation is well described by the three step model in the semi-classical approximation of the interaction of a strong laser field with an atom [24]. This model is illustrated in Fig. 2.3. In the first step, the most weakly bound electron of the atom is released by tunnel ionization. Next, the laser field accelerates the free electron. At the end of the process, when the laser field change its polarity, the electron is returning back and recombines with the parent ion. During this recombination, the sum of the excessive kinetic energy E_{kin} and the ionization energy is radiated in the

form of electromagnetic radiation

$$h\nu = E_{kin} + W_p \quad , \tag{2.5}$$

where W_p is the ionization potential, h is Planck's constant and ν is the frequency of the emitted radiation.

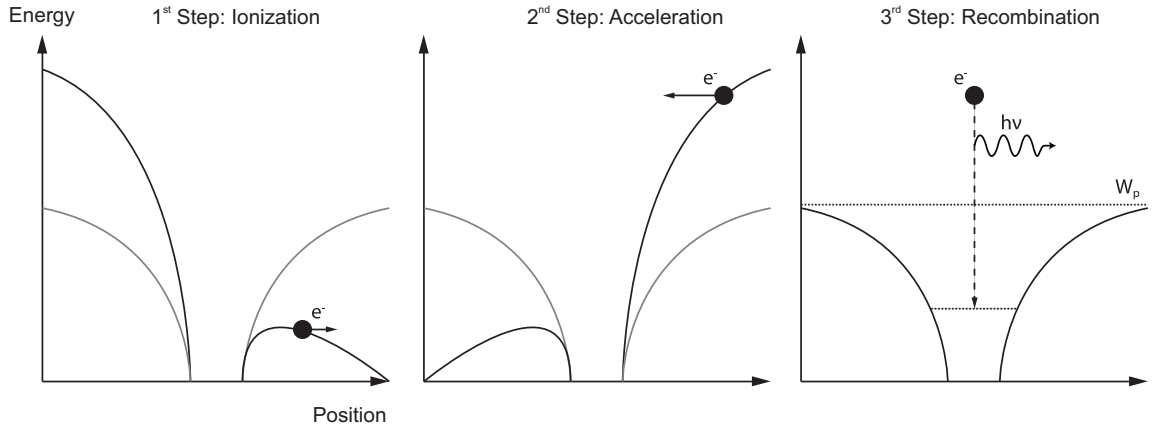

Fig. 2.3: The semi-classical three step model describing the process of the high harmonic generation, where solid lines depict the Coulomb potential of an atom that is disturbed by electric field of the laser.

The region of such high intensities is inevitably accompanied by other nonlinear processes and different ionization mechanisms. These ionization mechanisms can be classified according to the Keldysh parameter [25]

$$K_p = \sqrt{\frac{W_p}{2U_p}} \quad , \tag{2.6}$$

When $K_p \gg 1$, multi-photon ionization dominates, whereas $K_p \ll 1$ ionization is mainly achieved through tunneling.

The typical spectrum of HHG is shown in Fig. 2.4, where harmonics with characteristic plateau distribution and sharp cutoff can be seen. It is noteworthy that only odd harmonics are generated due to the centrosymmetricity of atoms. The frequency at which the highest harmonic (cutoff harmonic) occurs [26] can be determined as follows

$$h\nu_{max} = 3.17U_p + W_p \quad , \tag{2.7}$$

where U_p is the ponderomotive potential (the mean electron kinetic energy in an oscillating laser field).

The ponderomotive potential for an external electric field with an amplitude E_0 and angular frequency ω is given by [25, 27]

$$U_p = \frac{e^2 E_0^2}{4 m_e \omega^2} \quad . \tag{2.8}$$

The relation (2.8) can be rearranged into a more practical form

$$U_p[eV] = 0,933 \cdot 10^{-13} I\left[\frac{W}{cm^2}\right]\lambda^2[\mu m^2] \quad , \tag{2.9}$$

where amplitude of linearly polarized electric field is expressed using the vacuum impedance $Z_0 = \sqrt{\frac{\mu_0}{\epsilon_0}} = 377\ \Omega$ and the equation

$$E_0 = \sqrt{2IZ_0} \quad , \tag{2.10}$$

where I is the intensity of the electric field, ϵ_0 and μ_0 are the vacuum permittivity and permeability, respectively.

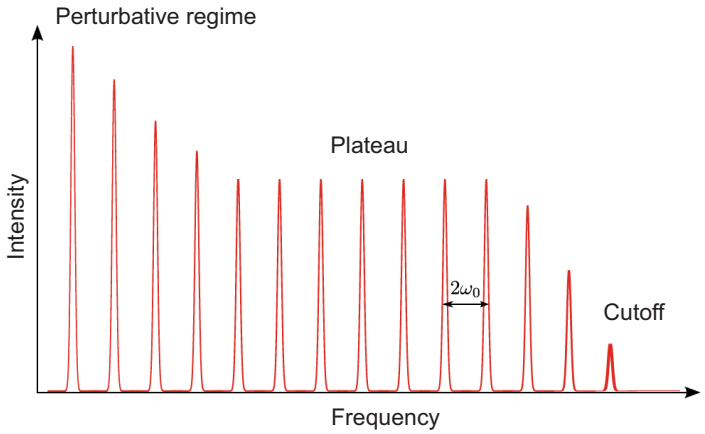

Fig. 2.4: The typical spectrum of high harmonic generation with characteristic plateau distribution, cutoff harmonic frequency and only odd harmonic frequencies. (Adapted from [28])

For many applications, the HHG beam is a very interesting EUV source of radiation because of the high spatial and temporal coherence. However, the main disadvantages are the low conversion efficiency and polychromatic spectrum which is generally not suitable for many applications. To overcome these challenges, current investigations are focused on developing advanced techniques such as quasi-phase matching [29–31], which intends to enhance the conversion efficiency.

2.3 Plasma-based soft X-Ray lasers (SXRLs)

The continuous development of laser technology, initiated by the first demonstration of the ruby laser [32] in 1960, achieved significant advancements towards shorter wavelengths. This progress ultimately led to the first demonstration of an X-ray laser nearly thirty years later [33].

The active medium of SXRLs is a highly ionized plasma with electron temperature of several hundreds eV and the very short lifetime of the population inversion from

picosecond to nanosecond (depending on material of the target and pumping scheme) [5, 6, 34, 35]. This short lifetime duration allows radiation to be amplified only in one or two passes through the active medium. Thus, the EUV beam is generated by the amplified spontaneous emission (ASE) [34] in the direction of a plasma column axis which is illustrated in Fig. 2.5. Such plasma active medium can be created by pinching discharge or high-intensity laser pulse. Currently, the most successful scheme is based on achieving the population inversion by the electron collisional excitation [35]. This process can be described by kinetics with quasi-steady state approximation when using longer (approximately ns) pumping, or by transient collisional excitation in the case of approximately (sub-)ps pumping.

As in most lasers, the generated radiation is highly monochromatic with $\frac{\Delta\lambda}{\lambda} \approx 10^{-4}$ and Doppler effect being the dominant spectral broadening mechanism [34]. Therefore, the temporal coherence of SXRLs is rather high, while their spatial coherence is relatively low [1]. Another disadvantage of SXRLs is the presence of a highly inhomogeneous far-field intensity pattern, which exhibits numerous speckles. The specific characteristics of these speckles depend on the chosen pumping scheme, as mentioned in [36]. Despite these limitations, SXRLs remain well-suited for many applications due to their high pulse energy ranging from a μJ to mJ.

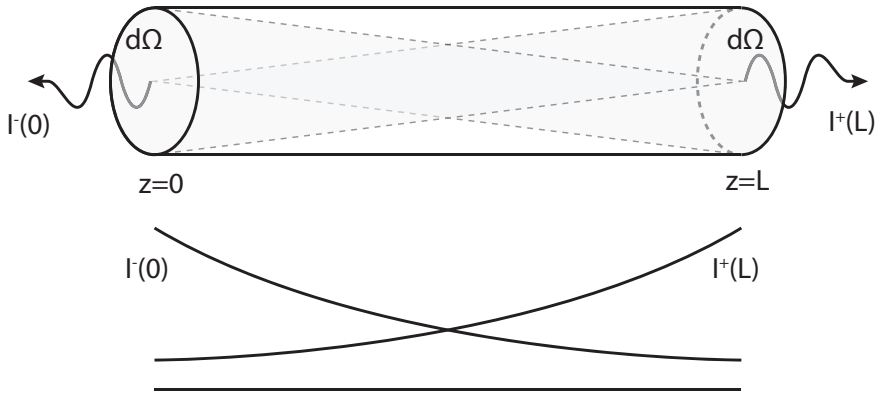

Fig. 2.5: The EUV beam generated by the amplified spontaneous emission (ASE) in a plasma column. It can be observed generation from both sides of the plasma column.

2.3.1 Quasi-steady state pumping

For long pumping with pulses typically of the order of ns, the quasi-steady state approximation is employed [5, 6]. The ionization level in a plasma approaches steady state while population inversion follows fast changes. Pumping can be performed just with one or more pulses, the process of ionization and population inversion is generally achieved within one intense laser pulse. This pumping scheme can be implemented either by pinching capillary discharge or by pumping the laser pulse with energies in

the range of hundreds of joules.

2.3.2 Transient pumping

For many years after the first successful demonstration of the lasing, the great interest was devoted to the sophisticated pumping schemes and recently the transient pumping has been firstly proposed [37] and experimentally demonstrated [38,39]. This pumping scheme separates the process of ionization and achieving population inversion. First a plasma is created with a long pulse in order of a ns and immediately after the long pulse follows a main pumping pulse which rapidly heats the plasma and induces the population inversion. In this pumping scheme, both ions concentration and population inversion are strongly non-stationary (transient). The transient pumping scheme significantly reduces the pumping requirements from kJ to the order of J.

2.3.3 SXRLs seeding

Currently, there is one very interesting possibility for the improvement of SXRLs output beam properties. Instead of the radiation originating from amplified spontaneous emission, the SXRL can serve as an amplifier for EUV beam with very good spatial and temporal properties [40]. For example, the HHG source is very suitable to generate a seed beam so that the main disadvantage of a low output energy can be significantly enhanced. On the other hand, there are many difficulties related to an experimental implementation such as precise timing, EUV beam alignment to the plasma amplifier (typically a few tens of micrometers in diameter), and spectral overlap of the seed with the lasing transition of the amplifier.

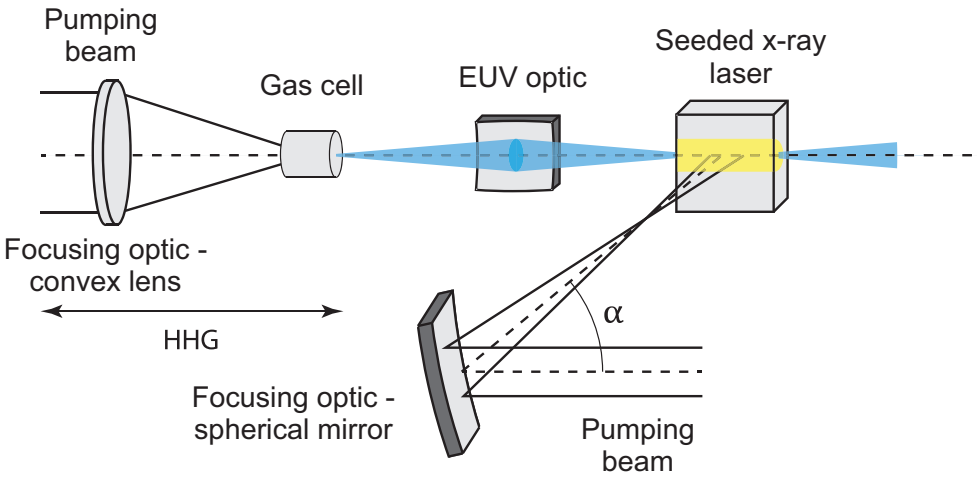

Fig. 2.6: The experimental setup of SXRL seeding chain with a beam injected from the high harmonic generation.

3 Coherence of electromagnetic radiation and free-space propagation of fully and partially coherent light

The main characteristics of coherent waves are their deterministic behavior during propagation and hence a relatively simple mathematical description. The coherence of electromagnetic radiation is, therefore, one of its crucial characteristics that has a significant impact on various applications based on imaging, holography, interferometry, diffraction, etc. The coherent properties are typically quantified using the mutual coherence function, which reflects the statistical properties of light.

In this section, we briefly describe coherence theory of optical fields, covering both temporal and spatial coherence. We also discuss the free-space propagation of fully and partially coherent beams, with a main focus on spatial coherence.

3.1 Mutual coherence function and complex degree of coherence

In this paragraph, we present a summary of the general outcomes from the theory of coherence introduced in [41]. For stationary field[1], the radiation properties are typically described by the mutual coherence function (cross-correlation function)

$$\Gamma(\boldsymbol{x_1}, \boldsymbol{x_2}, \tau) = \lim_{T\to\infty} \frac{1}{2T} \int_{-T}^{T} E(\boldsymbol{x_1}, t) E^*(\boldsymbol{x_2}, t-\tau) \mathrm{d}t \tag{3.1}$$

$$= \langle E(\boldsymbol{x_1}, t) E^*(\boldsymbol{x_2}, t-\tau) \rangle \quad . \tag{3.2}$$

This function is the time average[2] of a product of an optical field $E(\boldsymbol{x_1}, t)$ and its complex conjugate $E^*(\boldsymbol{x_2}, t-\tau)$ at two spatial points, $\boldsymbol{x_1}$, $\boldsymbol{x_2}$, and two temporal

[1] In the case of stationary fields, the character of the fluctuations does not change over time.

[2] In practice, there are stationary processes where the time average can be replaced by the ensemble average. Such processes are then referred as ergodic processes. All the fields will be considered stationary and ergodic throughout this thesis.

points, t, $(t-\tau)$ (which is the complex cross-correlation of two fields). It is suitable to normalize (3.2) and define the complex degree of coherence given by the relation

$$\mu(\boldsymbol{x_1}, \boldsymbol{x_2}, \tau) = \frac{\Gamma(\boldsymbol{x_1}, \boldsymbol{x_2}, \tau)}{\sqrt{I(\boldsymbol{x_1})I(\boldsymbol{x_2})}} \quad , \tag{3.3}$$

where intensity, according to (3.2), is given by

$$I(\boldsymbol{x_i}) = \Gamma(\boldsymbol{x_i}, \boldsymbol{x_i}, 0) \quad . \tag{3.4}$$

By the normalization, the complex degree of coherence satisfies the following inequality

$$0 \leq |\mu(\boldsymbol{x_1}, \boldsymbol{x_2}, \tau)| \leq 1 \quad . \tag{3.5}$$

Frequently, under certain circumstances (cross-spectrally pure light)[3] function (3.3) can be factorized [41] and then the temporal (longitudinal) and spatial (transverse) coherence are separated of each other

$$\mu(\boldsymbol{x_1}, \boldsymbol{x_2}, \tau) = \mu(\boldsymbol{x_1}, \boldsymbol{x_2}, 0)\mu(\boldsymbol{x_1}, \boldsymbol{x_1}, \tau) \quad . \tag{3.6}$$

There are several definitions for the coherence time τ_{coh} and spatial coherence length l_{coh}. The most frequent definition is the point at which the absolute value of the complex degree of coherence drops to the specified value, such as $\frac{\sqrt{2}}{2}$ or e^{-1}. Additionally, it is worth mentioning another formula defined in terms of the normalized root-mean square by the relation

$$\tau_{coh}^2 = \frac{\int_{-\infty}^{\infty} \tau^2 |\Gamma(\boldsymbol{x_1}, \boldsymbol{x_1}, \tau)|^2 \mathrm{d}\tau}{\int_{-\infty}^{\infty} |\Gamma(\boldsymbol{x_1}, \boldsymbol{x_1}, \tau)|^2 \mathrm{d}\tau} \quad . \tag{3.7}$$

Equivalently, the normalized root-mean square can be used to define spatial coherence length for special types of beams (assuming 1D Schell beams) where the mutual coherence function is spatially-shift invariant and rotational symmetric (the mutual coherence is a function of a single spatial variable). These sources are described in the following paragraphs.

3.1.1 Temporal coherence function and complex degree of temporal coherence

The temporal coherence function (sometimes referred to as the self-coherence function), is understood as the mutual coherence function evaluated at equal-space points

$$\Gamma(\tau) \equiv \Gamma(\boldsymbol{x_1}, \boldsymbol{x_1}, \tau) \quad , \tag{3.8}$$

where the dependence on spatial coordinate can be omitted. Equivalently, by the complex degree of temporal coherence is meant

$$\mu(\tau) \equiv \mu(\boldsymbol{x_1}, \boldsymbol{x_1}, \tau) \quad . \tag{3.9}$$

[3] All the fields will be considered as cross-spectrally pure light throughout this thesis. More information regarding the concept of cross-spectrally pure light can be found in [41].

3.1.2 Spatial coherence function and complex degree of spatial coherence

Analogically, the spatial coherence function (sometimes referred to as the equal-time correlation function or the mutual intensity), is understood the mutual coherence function evaluated at equal-time

$$\Gamma(\boldsymbol{x_1}, \boldsymbol{x_2}) \equiv \Gamma(\boldsymbol{x_1}, \boldsymbol{x_2}, 0) \quad , \tag{3.10}$$

where the dependence on time can be omitted. Similarly, by the complex degree of spatial coherence is meant

$$\mu(\boldsymbol{x_1}, \boldsymbol{x_2}) \equiv \mu(\boldsymbol{x_1}, \boldsymbol{x_2}, 0) \quad . \tag{3.11}$$

3.1.3 Conventional measurement of temporal coherence by Michelson interferometer

The well-known method for measuring the temporal coherence is based on experiments using the Michelson interferometer. In this method, an input beam is divided into two arms of the interferometer, and a delay τ is introduced in one arm due to a difference in their optical paths. The two delayed optical fields overlap and form interference fringes. To characterize the function $\mu(\tau)$, a visibility scan must be performed by varying the difference in arm lengths. The absolute value of the complex degree of coherence $\mu(\tau)$ can be determined from the interference pattern using the following formula

$$|\mu(\tau)| = \frac{1}{2}\frac{I_1 + I_2}{\sqrt{I_1 I_2}} V(\tau) \quad , \tag{3.12}$$

where I_1, I_2 are intensities of each beams with time delay τ and V is the visibility of the interference pattern defined as

$$V = \frac{I_{max} - I_{min}}{I_{max} + I_{min}} \quad . \tag{3.13}$$

The I_{max} and I_{min} are maximal and minimal intensity of the interference fringes. Obviously, it can be easily found by using (3.12) and (3.5) that $V \in [0, 1]$.

The method based on the Michelson interferometer cannot be directly used for EUV radiation due to the absence of suitable EUV optical elements. Therefore, an alternative approach employing wavefront division interferometry was developed.

3.1.3.1 Wavefront-division variable path difference interferometr for EUV

In the last decade, the EUV interferometer was designed and successfully employed for the temporal coherence measurement [42]. This interferometer consists of two dihedral mirrors in a grazing incidence geometry where one is fixed and the second one

is mobile so that a difference path is introduced (Fig. 3.1). The main idea is to split the beam spatially into two halves and then overlap them, resulting in the formation of an interference fringe pattern.

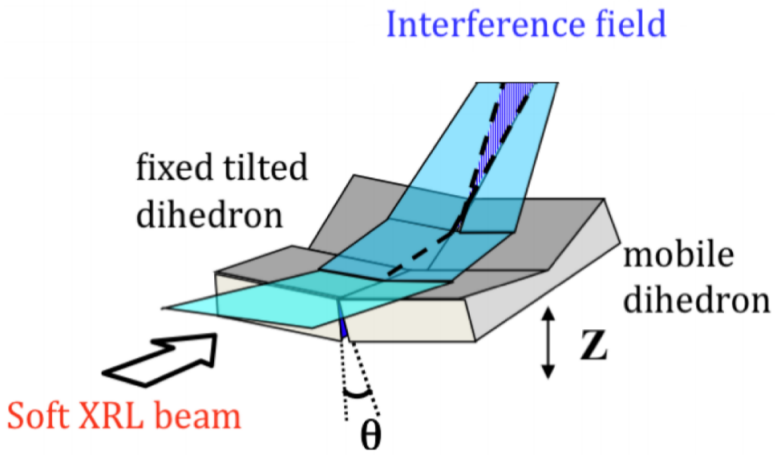

Fig. 3.1: The path difference interferometer for an EUV beam consists of two dihedral mirrors. One mirror is fixed, while the second can change the beam path of the spatially split beam. (Adapted from [43])

3.1.4 Conventional measurement of spatial coherence by Young's double-slit experiment

Similarly to the temporal coherence, the method for the determination spatial coherence can be based on the traditional Young's double slit experiment. The interference pattern is created by a radiation emitted from spatially separated slits and observed on the output screen. Equivalently, the absolute value of the complex degree of coherence $\mu(\boldsymbol{x_1}, \boldsymbol{x_1} + \boldsymbol{\Delta x})$ is measured by a varying distance $\boldsymbol{\Delta x}$ between slits and can be obtained from the interference pattern by the following formula [41]

$$|\mu(\boldsymbol{x_1}, \boldsymbol{x_1} + \boldsymbol{\Delta x})| = \frac{1}{2}\frac{I_1 + I_2}{\sqrt{I_1 I_2}} V(\boldsymbol{\Delta x}) \quad , \tag{3.14}$$

where I_1, I_2 are intensities on slits with positions vectors $\boldsymbol{x_1}$ resp. $\boldsymbol{x_1} + \boldsymbol{\Delta x}$ and V is the visibility of the interference pattern.

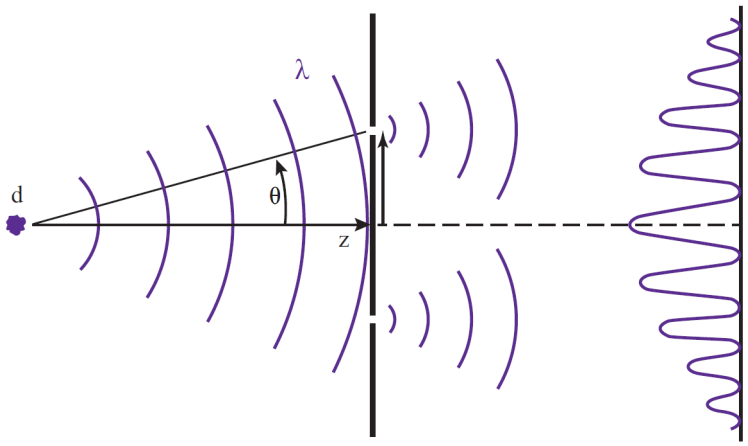

Fig. 3.2: Experimental setup for measuring spatial coherence using Young's double-slit experiment. (Adapted from [1])

3.2 Free-space propagation of spatially coherent monochromatic beams

The most general description of electromagnetic waves is provided by the well-known free-space Maxwell's equations. However, directly solving these equations using any state-of-the-art numerical method demands a significant amount of computation time. This system of vector partial differential equations (PDEs) describes the evolution of the electric field vector $\boldsymbol{E}(\boldsymbol{x}, t)$ and the magnetic field vector $\boldsymbol{B}(\boldsymbol{x}, t)$ and is expressed as

$$\nabla \boldsymbol{E}(\boldsymbol{x}, t) = 0 \tag{3.15}$$

$$\nabla \boldsymbol{B}(\boldsymbol{x}, t) = 0 \tag{3.16}$$

$$\nabla \times \boldsymbol{E}(\boldsymbol{x}, t) = -\frac{\partial}{\partial t}\boldsymbol{B}(\boldsymbol{x}, t) \tag{3.17}$$

$$\nabla \times \boldsymbol{B}(\boldsymbol{x}, t) = \frac{1}{c^2}\frac{\partial^2}{\partial^2 t}\boldsymbol{E}(\boldsymbol{x}, t) \quad , \tag{3.18}$$

where $c = \frac{1}{\sqrt{\epsilon_0 \mu_0}}$ is the vacuum speed of light. Fortunately, there is no need to solve this system of vector PDEs, and for our purposes, it will be sufficient to use approximate methods.

Furthermore, in the next paragraphs of this thesis, we do not need to deal with fully vector wavefields, and we can restrict ourselves to selected scalar approximate methods for free-space propagation, such as angular spectrum propagation, Fresnel diffraction integral, and Fraunhofer diffraction integral [44–46]. These methods and their main outputs are briefly introduced in the following paragraphs.

3.2.1 Fresnel number and approximations in regions of light propagation

Firstly, it is very important to choose the optimal scalar method of propagation for an optical field due to its validity in different regions depending on propagation distance and border conditions. The Fresnel number [44–47] is used to distinguish between these regions, depending on the propagation distance, wavelength and the specific size of an aperture. This number is defined as

$$N_F = \frac{a_{max}^2}{\lambda z} \quad , \tag{3.19}$$

where z is the propagation distance, λ is the diffracted radiation wavelength and a_{max} is the maximal aperture size. The field propagation characteristics, based on the Fresnel number, can be categorized into three specific regions:

1. **Near field**, where $N_F \gg 1$
   The near field is a region of geometric shadow where the field intensity exhibits significant oscillating microstructure within the overall object envelope.

2. **Fresnel region**, where $N_F \approx 1$
   This region is a transitional zone where signs of diffraction can be observed behind an opaque aperture, and the optical field intensity begins to smooth out.

3. **Fraunhofer region**, where $N_F \ll 1$
   The Fraunhofer region, also known as the far-field, is characterized by the dominance of the full wave behavior of electromagnetic waves. In this region, radiation is diffracted behind the geometrical shadow of the aperture, resulting in a smoothed-out optical field intensity.

3.2.2 Field propagation by angular spectrum method

The propagation of the field using the angular spectrum method is carried out through the principles of Fourier optics. Let us assume that $\mathcal{A}(\xi, \eta, z)$ represents the angular spectrum at a distance z, obtained by performing a Fourier transform of the optical field $A(x, y, z)$. The propagation of the angular spectrum along the z axis, originating from the angular spectrum $\mathcal{A}(\xi, \eta, 0)$, is described by

$$\mathcal{A}(\xi, \eta, z) = \mathcal{A}(\xi, \eta, 0)\mathcal{H}_0(\xi, \eta, z) \quad , \tag{3.20}$$

where the free-space optical transfer function is

$$\mathcal{H}_0(\xi, \eta, z) = \begin{cases} e^{-ikz\sqrt{1-\lambda^2\xi^2-\lambda^2\eta^2}} & , \quad \text{if} \quad \sqrt{\eta^2+\xi^2} < \frac{1}{\lambda} \\ 0 & , \quad \text{if} \quad \sqrt{\eta^2+\xi^2} \geq \frac{1}{\lambda} \end{cases} \quad . \tag{3.21}$$

The optical field after propagation can be simply obtained by applying the inverse Fourier transform to equation (3.20). This method is mainly suitable for the near field and Fresnel region. While propagation across the Fraunhofer region is feasible, it may lead to significant computational load when utilizing the fast Fourier transform algorithm. This is due to the requirement of a wide computational window, resulting from the identical sampling used for both the small object and the diffracted field at wide angles. For instance, enhanced angular spectrum methods capable of handling propagation across both near field and far-field regions have been proposed in the following studies [48, 49].

3.2.3 Field propagation by Fresnel diffraction integral

The Fresnel diffraction integral, which is only valid in Fresnel region, can be expressed via Fourier transform by relation

$$A(x,y,z) = \frac{i}{\lambda z} e^{-\frac{i\pi}{\lambda z}(x^2+y^2)} \bar{\mathcal{A}}(\xi,\eta) \quad , \tag{3.22}$$

where spatial frequencies are evaluated at $\xi = \frac{x}{\lambda z}$, $\eta = \frac{y}{\lambda z}$ and $\bar{\mathcal{A}}(\xi,\eta)$ is Fourier transform of the modified input field $A(x_0,y_0,0)$ given by

$$\bar{\mathcal{A}}(\xi,\eta) = \mathscr{F}\{A(x_0,y_0,0) e^{-\frac{i\pi}{\lambda z}(x_0^2+y_0^2)}\}(\xi,\eta) \quad . \tag{3.23}$$

Note that the input field is modified only by a quadratic phase term, which approaches a value of one as the radiation propagates to the Fraunhofer region.

3.2.4 Field propagation by Fraunhofer diffraction integral

The propagation in the case of Fraunhofer diffraction is realized only by Fourier transform, as quadratic phase term in (3.23) becomes negligible in the Fraunhofer region. As a result, the diffracted field is given by

$$A(x,y,z) = \frac{i}{\lambda z} e^{-\frac{i\pi}{\lambda z}(x^2+y^2)} \mathcal{A}(\xi,\eta) \quad , \tag{3.24}$$

where spatial frequencies are evaluated at $\xi = \frac{x}{\lambda z}$, $\eta = \frac{y}{\lambda z}$ and $\mathcal{A}(\xi,\eta)$ is Fourier transform of the input field

$$\mathcal{A}(\xi,\eta) = \mathscr{F}\{A(x,y,0)\}(\xi,\eta) \quad . \tag{3.25}$$

3.3 Free-space propagation of partially coherent light

Propagation of a partially coherent light can be generally treated by a three different methods [41, 50]: solving Helmholtz equation for the mutual coherence function, modal

expansion of the mutual coherence function or propagation of Wigner function in a phase space. In this thesis, we will discussed only first two methods since propagation of coherence function by modal expansion was further considered in the following chapters.

3.3.1 Propagation of the mutual coherence function by wave equations

In this paragraph, we will introduce the general free-space propagation of the mutual coherence function. It can be easily found, by deriving from the free-space wave equation [41], that such propagation is expressed by following wave equations for the mutual coherence function

$$\nabla_{\boldsymbol{x_1}}\Gamma(\boldsymbol{x_1},\boldsymbol{x_2},\tau) = \frac{1}{c^2}\frac{\partial^2}{\partial\tau^2}\Gamma(\boldsymbol{x_1},\boldsymbol{x_2},\tau) \tag{3.26}$$

$$\nabla_{\boldsymbol{x_2}}\Gamma(\boldsymbol{x_1},\boldsymbol{x_2},\tau) = \frac{1}{c^2}\frac{\partial^2}{\partial\tau^2}\Gamma(\boldsymbol{x_1},\boldsymbol{x_2},\tau) \quad . \tag{3.27}$$

Next, we can apply the Fourier transform to equations (3.26) and (3.27) which results in time-independent wave equations known as the free-space Helmholtz equations

$$\nabla_{\boldsymbol{x_1}}W(\boldsymbol{x_1},\boldsymbol{x_2},\omega) + k_0^2 W(\boldsymbol{x_1},\boldsymbol{x_2},\omega) = 0 \tag{3.28}$$

$$\nabla_{\boldsymbol{x_2}}W(\boldsymbol{x_1},\boldsymbol{x_2},\omega) + k_0^2 W(\boldsymbol{x_1},\boldsymbol{x_2},\omega) = 0 \quad , \tag{3.29}$$

where $W(\boldsymbol{x_1},\boldsymbol{x_2},\omega)$ is the cross-spectral density given by the Fourier transform of the mutual coherence function as

$$W(\boldsymbol{x_1},\boldsymbol{x_2},\omega) = \mathscr{F}\{\Gamma(\boldsymbol{x_1},\boldsymbol{x_2},\tau)\}(\boldsymbol{x_1},\boldsymbol{x_2},\omega) \tag{3.30}$$

and $k_0 = \frac{\omega}{c}$ is the vacuum wavenumber.

Directly solving such a system of equations is computationally very demanding, again making it inconvenient for practical purposes. Therefore, additional techniques are necessary to simplify the propagation of mutual coherence function.

3.3.2 Propagation of the spatial coherence function by modal expansion

Let assume that spatial coherence function belongs to the class of functions fulfilling a square-integrability

$$\iint |\Gamma(\boldsymbol{x_1},\boldsymbol{x_2},z)|^2 \mathrm{d}\boldsymbol{x_1}\mathrm{d}\boldsymbol{x_2} < \infty \quad . \tag{3.31}$$

It can be shown from the previous equation (3.31) and (3.2) that function $\Gamma(\boldsymbol{x_1},\boldsymbol{x_2},z)$ is a Hilbert-Schmidt kernel and the kernel is Hermitian and non-negative definite [41].

Thus the spatial coherence function can be written, according to the Mercer's theorem, in the following expansion

$$\Gamma(\boldsymbol{x_1}, \boldsymbol{x_2}, z) = \sum_{n=1}^{+\infty} \alpha_n \phi_n^*(\boldsymbol{x_1}, z)\phi_n(\boldsymbol{x_2}, z) = \sum_n f_n^*(\boldsymbol{x_1}, z) f_n(\boldsymbol{x_2}, z) \quad , \tag{3.32}$$

where the symbol * denotes the complex conjugate, $f_n(\boldsymbol{x}, z) = \sqrt{\alpha_n}\phi_n(\boldsymbol{x}, z)$ and α_n, ϕ_n are eigenvalues and eigenfunctions of the integral equation

$$\int_{-\infty}^{+\infty} \Gamma(\boldsymbol{x_1}, \boldsymbol{x_2}, z)\phi_n(\boldsymbol{x_1}, z)\mathrm{d}\boldsymbol{x_1} = \alpha_n \phi_n(\boldsymbol{x_2}, z) \quad . \tag{3.33}$$

In other words, the light in certain plane z can be described as an incoherent sum of coherent fields (modes) f_n, so knowing these fields in one plane, we can solve their propagation to another plane by well-known scalar field methods using e.g. Fresnel approximation of the diffraction integral [44–47]. Therefore, the relation (3.32) allows us to propagate the spatial coherence function by independent propagation of multiple coherent modes f_n.

3.3.3 Schell beams

One of the common classes of partially coherent sources are called Schell beams where the mutual coherence function depends only on spatial coordination difference

$$\Gamma(\boldsymbol{x_1}, \boldsymbol{x_2}, \tau) = f(\boldsymbol{x_1} - \boldsymbol{x_2}, \tau) \quad , \tag{3.34}$$

these type of sources are usually called shift-invariant.

3.3.4 Gaussian Schell-model beams

As a further specification of Schell beams, it can be assumed that both the beam intensity and coherence function follow a Gaussian profile. In this case, we can refer such beams as a Gaussian Schell-model beam. For the sake of simplicity, we can consider one-dimensional case, which is represented by following equation

$$\Gamma(x_1, x_2) = A^2 e^{-\frac{x_1^2+x_2^2}{4w_0^2}} e^{\frac{-(x_2-x_1)^2}{2l_{coh}^2}} \quad , \tag{3.35}$$

where A is amplitude, l_{coh} is the spatial coherence length and w_0 is the intensity beam waist. If we express Gaussian Schell-model beam according to modal expansion (3.32), it can be found that the integral equation (3.33) can be analytically solved [51, 52]. We

can obtain the following eigenvalues and eigenfunctions from the analytical solution

$$f_n = \left(\frac{2c_0}{\pi}\right)^{\frac{1}{4}} \frac{1}{\sqrt{2^n n!}} H_n(x\sqrt{2c_0}) e^{-c_0 x^2} \tag{3.36}$$

$$\alpha_n = A^2 \left(\frac{\pi}{a_0 + b_0 + c_0}\right)^{\frac{1}{2}} \left(\frac{b_0}{a_0 + b_0 + c_0}\right)^n \quad , \tag{3.37}$$

where $H_n(x)$ are Hermite polynomials and the corresponding coefficients are

$$a_0 = \frac{1}{4w_0^2} \tag{3.38}$$

$$b_0 = \frac{1}{2l_{coh}^2} \tag{3.39}$$

$$c_0 = \sqrt{a_0^2 + 2a_0 b_0} \quad . \tag{3.40}$$

Next, we can easily find the contribution of different modes to the modal expansion of the Gaussian Schell-model beam by evaluating the ratio α_n/α_0, that can be expressed as

$$\frac{\alpha_n}{\alpha_0} = \left(\frac{b}{a + b + c}\right)^n \tag{3.41}$$

This equation can be rearranged to a more understandable form

$$\frac{\alpha_n}{\alpha_0} = \left(\frac{1}{\frac{q^2}{2} + 1 + q\sqrt{(\frac{q}{2})^2 + 1}}\right)^n \quad , \tag{3.42}$$

where

$$q = \frac{l_{coh}}{w_0} \tag{3.43}$$

represents the ratio of two Gaussian profiles, determined by the parameters of the coherence length and the beam waist. The equation (3.42), as a function of the q, is depicted in Fig. 3.3. By assessing the value of q, we can determine the number of modes needed to represent partially coherent light according to the Gaussian Schell-model. Sources with $q \gg 1$ are nearly fully spatially coherent, and only one or a few modes are required to adequately describe them. On the other hand, sources with $q \ll 1$ are considered nearly incoherent, requiring a large number of modes for their representation.

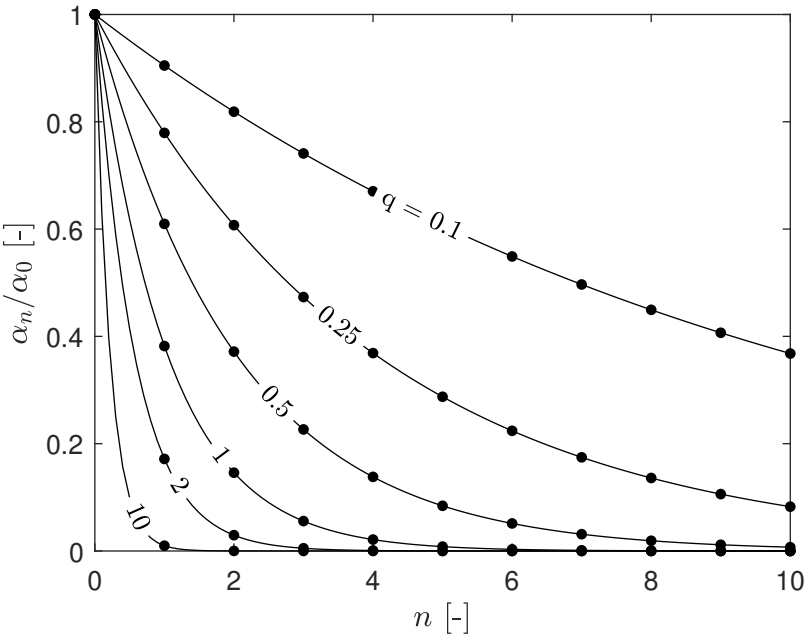

Fig. 3.3: The eigenvalues ratio $q = \alpha_n/\alpha_0$ of the Gaussian Schell-model beam. Sources with $q \gg 1$ can be considered as spatially coherent, while sources with $q \ll 1$ can be considered as incoherent.

4 Pulse duration of SXRL based on temporal coherence influencing the speckle intensity pattern

In this chapter, a novel method for estimating the pulse duration of partially coherent soft X-ray pulses from a far-field intensity pattern is presented. These results were already published in [7]. The method is based on intensity statistics at a single point in space and time, which allows the number of coherent longitudinal modes to be measured. Utilizing the knowledge of the coherence time of the radiation, either from measurement of the spectral bandwidth or from numerical simulations, the duration of each individual pulse can be evaluated. This method was used to estimate the pulse duration of the laser-driven nickel-like molybdenum soft X-ray laser that is based on amplified spontaneous emission from a narrow plasma column and emits at wavelength of 18.9 nm. By varying the length of the gain medium a clear dependence of number of modes caused mainly by the spectral line narrowing was observed.

4.1 Method of far-field intensity analysis from SXRL

Our method is based on statistical analysis of the far-field intensity pattern consisting of many speckles, which are either naturally present in the beam or can be produced by inserting a suitable scatterer into a highly transversally coherent beam [53]. Such a scattering mask can be designed for each particular experimental configuration following the theory of the Speckle statistics [44,54]. The origin of these intensity fluctuations in the far-field can be explained through the interference of elementary coherent components of the radiation with random phase change. In the case of ASE based SXRLs these random phase changes result from propagation of the radiation through the amplifying plasma gain medium with inhomogeneities in the refractive index causing optical path differences shorter than the coherent length that is determined by the coherence time τ_{coh} [36]. From the theory of first order speckle statistics [44, 55, 56], which is the intensity statistics at a single point in space and time, the sum of N independent speckle patterns each with mean intensity I_0 follows the probability distribution p of

intensities I given by

$$p(I) = \frac{I^{N-1}}{\Gamma_f(N) I_0^N} \exp\left(-\frac{I}{I_0}\right) \quad , \tag{4.1}$$

where $\Gamma_f(N)$ is the gamma function. The number N corresponds to an effective number of longitudinal coherence modes for a single polarization. Thus, the measured number of modes needs to be corrected in dependence on the polarization state of the detected radiation. Evaluating N by fitting the histogram of the far-field intensity pattern with (4.1) and having prior knowledge of the spectrum of the pulse one can estimate the duration (here defined as two times the root mean square) of the pulse as [57]

$$\tau_{pulse}^{2RMS} = N \tau_{FL}^{2RMS} \quad , \tag{4.2}$$

where τ_{FL}^{2RMS} is the Fourier limited pulse duration (two times the root mean square). For completeness, the relation between the duration of the Gaussian pulse at the full width at half-maximum (FWHM) and τ_{FL}^{2RMS} reads

$$\tau_{pulse}^{FWHM} = \sqrt{2 \ln 2} \tau_{pulse}^{2RMS} \tag{4.3}$$

This relation for the FWHM duration of the pulse can be used without changing the physical meaning of N [57]. Supposing the temporal coherence function with a Gaussian shape and a coherence time defined by the formula (3.7), then the relation between the coherence time and the Fourier limited pulse duration reads

$$\tau_{coh} = \frac{\tau_{FL}^{2RMS}}{\sqrt{2}} \quad . \tag{4.4}$$

4.2 Experimental setup of Ni-like Mo SXRL

The method suggested in the Section 4.1 was implemented to analyze the output of the transient collisionally pumped Ni-like Mo X-ray laser employing grazing incidence pumping scheme (GRIP) [58, 59]. We have used numerical simulations to evaluate the evolution of the spectral linewidth and the pulse envelope along plasma amplification.

The SXRL was realized at the PALS laboratory[1] [60] with the GRIP geometry and pumped by the time profiled laser pulse [61] (a prepulse and a main pumping pulse are included in one beam) created through control of timing Pockels cells in regenerative amplifier. The experiment was performed on the Ti:Sapphire laser system with a central wavelength of 810 nm and repetition rate of 10 Hz delivering pulses of 500 mJ total energy on target.

[1] Prague Asterix Laser System, the research unit which operates under the supervision of Institute of physics and Institute of plasma physics of the Czech Academy of Sciences

4.2.1 Pumping conditions

The gain medium was created in the Ni-like Mo plasma with the following lasing transition

$$(3d^9_{3/2}4d_{3/2})_{J=0} \rightarrow (3d^9_{5/2}4p_{3/2})_{J=1} \quad , \tag{4.5}$$

which emits at the wavelength of 18.9 nm [62]. The schematic of the experimental setup is shown in Fig. 4.1. First, the plasma is created by a 4 ns long prepulse that preionizes the medium. Immediately after the prepulse follows the main heating pulse that contains approximately 70% of the total pumping energy. The main pulse with a duration of 2 ps creates a population inversion by electron collisional excitation in the rapidly heated plasma.

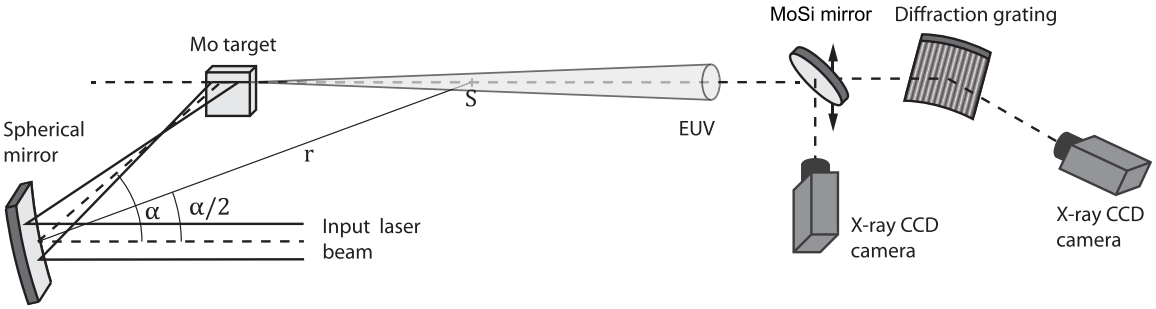

Fig. 4.1: Experimental setup of the Ni-like molybdenum SXRL with the grazing incidence pumping and diagnostics of the generated beam.

4.2.2 Line focus created by a spherical mirror

Using simplified analytical formulas for the line focus created by focusing the collimated beam of the diameter D with a spherical mirror [63], we can find the length of the line focus

$$L = \frac{D}{2} \sin \frac{\alpha}{2} \quad , \tag{4.6}$$

where α is the grazing incidence angle (Fig. 4.1), and the velocity of the traveling wave as

$$v = \frac{c}{\cos \alpha} \quad . \tag{4.7}$$

The focal line with length of 3.4 mm was created by focusing a super-Gaussian laser beam of the diameter 40 mm with a spherical mirror of radius of curvature of 1 m and incident on a Mo slab target at a grazing angle $\alpha = 20°$. Estimated intensities inside the line focus for the prepulse and the main pumping pulse were approximately $2 \cdot 10^{10}$ $\frac{W}{cm^2}$ and $1 \cdot 10^{14}$ $\frac{W}{cm^2}$, respectively.

4.2.3 EUV diagnostics of Ni-like Mo SXRL

The on-axis soft X-ray spectrum was analyzed using a flatfield spectrometer, which consists of a gold-coated grazing incidence reflection grating with variable line spacing and a back illuminated X-ray CCD camera. The infrared and visible radiation from the plasma has been blocked by a 160 nm thick Al filter. Strong lasing was achieved, as shown on a spectrogram in Fig. 4.2, where the ASE line dominates almost three orders of magnitude over the incoherent background emission from the plasma. Changing the length of the plasma column by shifting the Mo target edge along the line focus, we evaluated the small signal gain coefficient as $g_0 = 39\ cm^{-1}$. The maximum effective gain medium length was found to be only 2.9 mm long due to the focus intensity drop on the edges, resulting in a maximum gain-length product of $g_0 L = 11$. This indicates that the amplifier worked slightly below saturation [64].

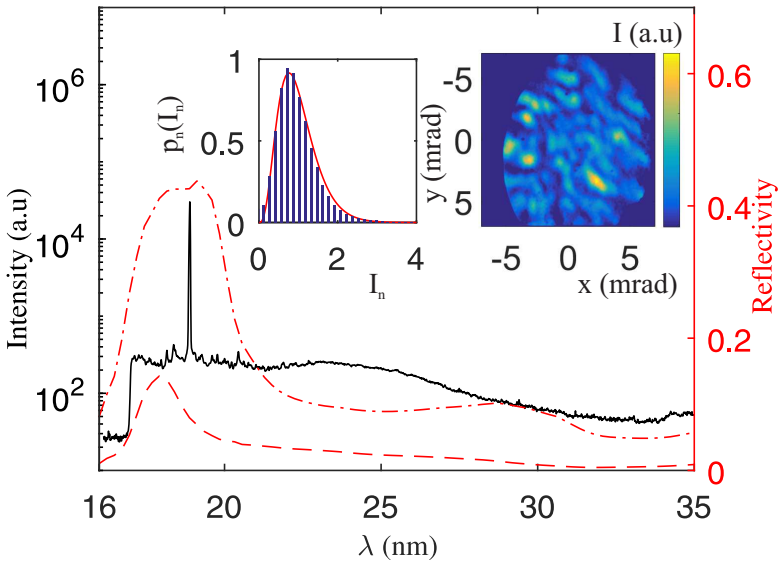

Fig. 4.2: On-axis single shot spectrum of the Ni-like molybdenum X-ray laser with the laser line at 18.9 nm (solid black line), and s-polarization (red dash and dotted line) respectively, p-polarization (red dashed line) reflectivities of the MoSi mirror used to reflect the beam on the far-field camera. Upon reflection on the MoSi mirror the lasing line is s-polarized with the polarization ratio 5:1 and represents 50% of the total energy reflected by the mirror. The typical far-field speckle pattern (false colors) and histogram of its normalized intensity statistics fitted with equation (4.1) (red solid line) are shown in the inset.

The total energy in the generated soft X-ray pulse was of the order of 0.1 μJ. The intensity profile of the generated beam was recorded by the back-illuminated X-ray CCD camera after reflection from a multilayered MoSi mirror. The total distance between the source and the camera was 2 m resulting in Fresnel number $N_F < 0.1$, which justifies the far-field approximation. Spectral reflectivities of the multilayered

mirror for different polarizations are shown in Fig. 4.2. Due to a relatively broad bandwidth reflected by this mirror, the lasing line represents approximately 50% of the total energy reflected by the mirror. The typical far-field intensity pattern with a subtracted incoherent background (see the inset of Fig. 4.2) exhibits characteristic inhomogeneities in the form of speckle pattern. This intensity speckle pattern is typical for lasers with transient population inversion, as they exhibit only a few longitudinal modes [65].

4.3 Experimental results of speckle statistics

We have studied the number of longitudinal modes N measured from the statistics of far-field intensity patterns as a function of length of the gain medium (see Fig. 4.3). In theory, we expect two main effects that are responsible for the evolution of the number of longitudinal modes. Firstly, the lasing line experiences gain narrowing during amplification. Secondly, the generated pulse shortens due to the limited gain duration and also due to the mismatch of the propagation velocity of the generated radiation and the velocity of the pumping pulse inside the gain medium. That is why we implemented a 1D radiative transfer model that solves the evolution of spectral linewidth and couple it with a 1D pulse envelope propagation code, which includes the effects of travelling wave velocity of the pumping and finite gain duration of the amplifying medium. In the radiative transfer model [66] the lineshape evolution is affected by the Doppler broadening (Gaussian function S) and natural broadening (Lorentzian function $\Phi(\nu, u)$ with frequency variable u and peak at ν). An appropriate differential equation in space-frequency domain for radiative transfer reads

$$\frac{\mathrm{d}I}{\mathrm{d}z} = \frac{J_0}{\mathcal{V}(\nu_0)}\left[1 + \frac{g_0}{J_0} I(\nu, z)\right] \int_0^\infty \frac{S(u)\Phi(\nu, u)}{1 + \int_0^\infty I(\nu')\Phi(\nu', u)\mathrm{d}\nu'} \mathrm{d}u \tag{4.8}$$

where $I(\nu, z)$ and the contribution from spontaneous emission J_0 are normalized to the saturation intensity, g_0 is a small signal gain coefficient at the line center, and $\mathcal{V}(\nu_0)$ is the height of the normalized lineshape function.

In our simulations we have used the measured value of $g_0 = 39\ cm^{-1}$, estimated ion temperature of 50 eV and other parameters typical for the lasing transition of Ni-like Mo SXRL [67]. We have observed clear gain narrowing of the lasing line without an onset of gain rebroadenning caused by saturation, as our source did not reach that point. The resulting coherence length as a function of the gain medium length (see the inset of Fig. 4.3) is in good agreement with values measured experimentally using a similar pumping configuration [42].

4.3.1 Estimation of the pulse duration

The pulse duration τ_{pulse}^{2RMS} is obtained from the 1D pulse propagation including finite gain duration with Gaussian profile and travelling wave pumping. The Gaussian gain profile is determined by the gain coefficient g_0 defining its amplitude and width τ_g^{2RMS}. The value of the gain duration was estimated by the best fit from measured number of modes when coupled to the radiative transfer data. Applying this method we found out $\tau_g^{2RMS} = 20\ ps$ and the resulting theoretical dependence of the number of modes together with the measured number of modes is displayed in Fig. 4.3 showing good agreement between the simulated and measured dependencies.

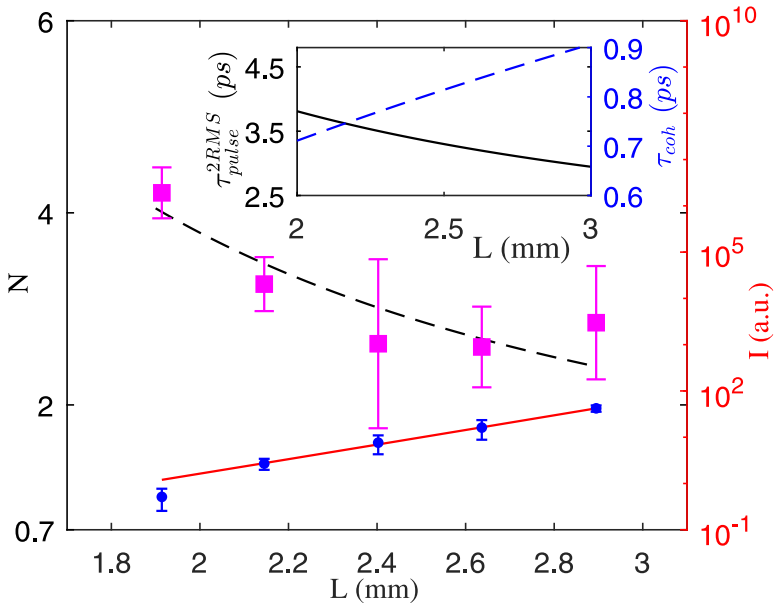

Fig. 4.3: Number of modes measured from the far-field intensity pattern by the intensity speckle statistics (pink squares), and the numerical simulation of the number modes obtained from the 1D radiative transfer and the pulse envelope propagation code (black dashed line). The gain measurement (blue dots) fitted by a Linford formula [68] with $g_0 = 39.3\ cm^{-1}$ (solid red line). The error bars indicate standard deviation of the set of measurements at each point. The duration obtained from 1D simulations of the coherence time τ_{coh} and pulse length τ_{pulse}^{2RMS} during propagation is shown in the inset.

Systematic uncertainties in the estimation of the pulse duration τ_{pulse}^{2RMS} are determined from the errors in evaluating the number of modes from the far-field intensity pattern according to equation (4.1) and from the accuracy of the evaluation of lasing lineshape. In our case, the spectral linewidth is mainly given by the ion temperature, because the Doppler effect is the dominant broadening mechanism. In the first case, we have numerically demonstrated that the error in determining the number of modes N is below 5%, if $N \leq 50$. The influence of the inaccurate value of g_0 was recognized

as negligible. On the other hand, a 10 eV deviation of the ion temperature from 50 eV has shown only 10% difference in the calculation of coherence time, so we can estimate the total relative systematic error of the measurement to be below 15 %. The method fails for very large number of modes, i.e., for pulses with poor temporal coherence, as the contrast of the speckle pattern decreases and, fitting its histogram with eq. (4.1), becomes challenging. For instance, this is the case for SXRLs employing quasi-steady state pumping schemes [65].

Considering both the statistical fluctuations and possible systematic error we can evaluate the pulse duration at the end of our amplifier estimated from the far-field intensity patterns as $\tau_{pulse}^{2RMS} = (3.0 \pm 0.6)\ ps$, which would correspond to $\tau_{pulse}^{FWHM} = (3.5 \pm 0.7)\ ps$ under an assumption of Gaussian-shaped pulse.

5 Coherent diffractive imaging (CDI)

The technique of coherent diffractive imaging is one of lensless imaging methods because there is no need for traditional imaging optics [69]. Instead, it is based on a highly coherent incident beam that produces a diffraction pattern from the sample under investigation. This diffraction pattern is typically recorded in the Fraunhofer plane using a camera and subsequently subjected to post-processing. In this approach, the role of an optical imaging element is replaced by numerical computations that incorporate certain assumptions to ensure convergence towards the original optical field of the sample, including both its amplitude and phase. That is why these algorithms are referred to as phase-retrieval algorithms. A few decades ago, in 1999, the first successful demonstration of coherent diffractive imaging was achieved with X-ray wavelengths [70].

Currently, the most commonly used algorithms for CDI reconstruction are Hybrid Input-Output (HIO) algorithm [71], Relaxed Averaged Alternating Reflections (RAAR) technique [72], and Difference Maps (DM) method [73].

The main advantages of this imaging technique include aberration-free imaging, a relatively simple experimental setup, as well as the ability to retrieve the phase information. The CDI is especially suitable technique of imaging for the spectral region discussed in this thesis due to lack of optical elements with a high reflectivity and high numerical aperture.

In this chapter, we will provide an introduction to the phase retrieval problem and discuss the methods that led to the development of the commonly used HIO algorithm by Fienup [9, 10, 71]. The implementation of the HIO algorithm was necessary for evaluating experimental results in the subsequent chapters. Moreover, we will also introduce the theoretical principles behind another diffractive-based imaging technique explored in this thesis, known as ptychographic coherent diffractive imaging.

5.1 Phase retrieval algorithms

Several phase retrieval algorithms have been developed to solve the problem of reconstructing the original optical field in the object plane [9,11,69,72,73]. These algorithms operate through an iterative process involving forward and backward field propagation between the object plane and the plane where the diffraction pattern is recorded. The optimal solution is obtained by fulfilling the constraints imposed by these two planes. Typically, the successful image reconstruction requires at least a few hundreds of iterations.

5.1.1 Error Reduction (ER) phase retrieval algorithm

One of the pioneering algorithm for the phase problem is the error reduction algorithm [10] which can be considered as a generalized Gerchberg-Saxton alghorithm [11]. The Gerchberg-Saxton was originally developed for phase retrieval from intensity measurements in two planes. In the error reduction algorithm, the propagation of the optical field is considered in the Fraunhofer approach, simplifying the propagation to a Fourier relationship between corresponding planes. The block scheme of the error reduction algorithm is illustrated in Fig. 5.1. This algorithm repeats sequentially following simple steps:

Initialization: The initial optical field $F_1(\boldsymbol{\xi})$ in the detector plane is created by combining amplitudes from the measured intensity diffraction pattern $I_{ref}(\boldsymbol{\xi})$ with a random (or approximative guess) phase φ_{rand}, mathematically this can be expressed as

$$F_1'(\boldsymbol{\xi}) = \sqrt{I_{ref}(\boldsymbol{\xi})} e^{i\varphi_{rand}(\boldsymbol{\xi})} \quad . \tag{5.1}$$

1. **Backward propagation to the object plane (real space):** The backward propagation from the detector plane to the object plane in the i-th iteration is performed by the inverse Fourier transform of the current optical field estimate.

$$f_i(\boldsymbol{x}) = \mathcal{F}^{-1}\{F_i'(\boldsymbol{\xi})\} \tag{5.2}$$

2. **Modified object plane (real space constrains):** The amplitudes of the real-space field are set to zero in regions where the sample is opaque, in order to obtain a new estimate of the real-space field. To achieve algorithm convergence, it is necessary for more than half of the image pixels to be known (zero values) in order to satisfy the oversampling[1] condition. The real space constrains are defined by an illumination probe support function $\Pi(\boldsymbol{x})$. Outside the support region, the probe field is set to zero, while inside the support region, it equals 1.

$$f_{i+1}'(\boldsymbol{x}) = f_i(\boldsymbol{x})\Pi(\boldsymbol{x}) \tag{5.3}$$

[1] The oversampling condition will be discussed later in this chapter.

3. **Forward propagation to the detector plane (reciprocal space):** The Fourier transform is applied to the current real space estimate.

$$F_{i+1}(\boldsymbol{\xi}) = \mathcal{F}\{f'_{i+1}(\boldsymbol{x})\} \tag{5.4}$$

4. **Detector plane constrains (reciprocal space constrains):** The new optical field estimate in the detector plane is created by replacing field amplitudes with the square root of the measured intensity diffraction pattern $I_{ref}(\boldsymbol{\xi})$ while field phase is preserved. Next, the algorithm goes to the first step and repeats all cycle again with the (i+1)-th iteration.

$$F'_{i+1}(\boldsymbol{\xi}) = \sqrt{I_{ref}(\boldsymbol{\xi})}\frac{F_{i+1}(\boldsymbol{\xi})}{|F_{i+1}(\boldsymbol{\xi})|} \tag{5.5}$$

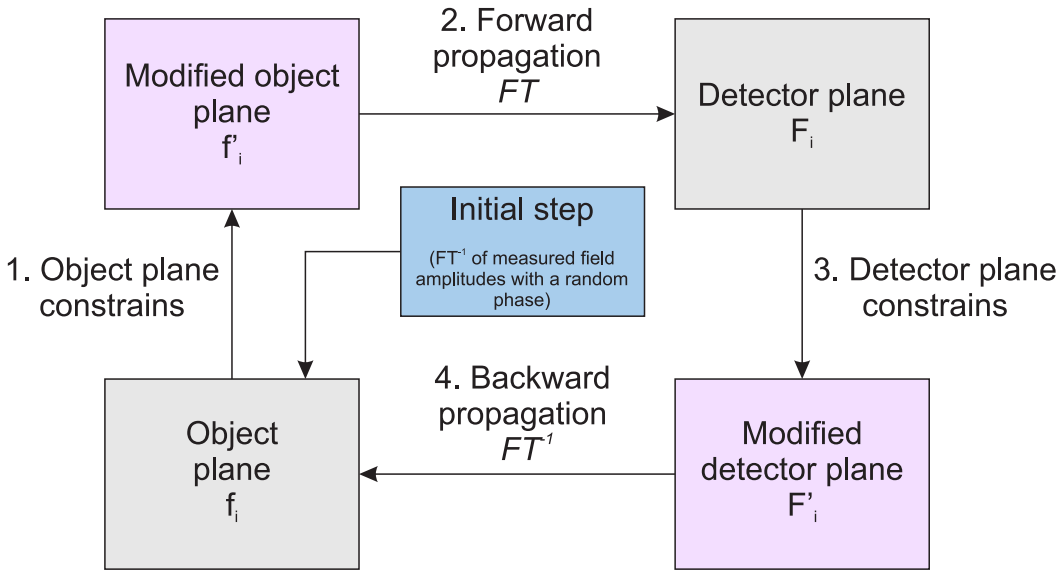

Fig. 5.1: The block diagram illustrates the error reduction algorithm.

5.1.2 Input-Output (IO) algorithm

In this algorithm and generally in other phase retrieval algorithms, the following three operations are the same as those described in the error reduction algorithm: forward propagation, satisfying the detector plane constraints, and backward propagation. These three operations can be grouped together, resulting in a nonlinear system with only input $f^{in}(\boldsymbol{x})$ and output $f^{o}(\boldsymbol{x})$ [71], both in real space (Fig. 5.2). It is evident that the output of such a system, when used as the next input, will always satisfy the detector plane constraints. Therefore, the solution is achieved when $f^{o}(\boldsymbol{x})$ also satisfies the object plane constrains. We can denote γ as the set of points where $f^{o}(\boldsymbol{x})$ satisfies these constrains. Although the considered system is nonlinear, it can

be assumed that a small changes in the input values lead to a roughly proportional changes in the output.

Obviously, no further changes are necessary for next input, in regions where $f^o(x)$ satisfies constrains. However, in regions where $f^o(\boldsymbol{x})$ does not satisfy the constrains, the next input must be adjusted to drive the output to zero (for $\boldsymbol{x} \notin \gamma$ has to be $f_i^o(\boldsymbol{x}) = 0$). As a result, the next input can be determined as follows

$$f_{i+1}^{in}(\boldsymbol{x}) = \begin{cases} f_i^{in}(\boldsymbol{x}) & \text{if } \boldsymbol{x} \in \gamma \\ f_i^{in}(\boldsymbol{x}) - \beta f_i^o(\boldsymbol{x}) & \text{if } \boldsymbol{x} \notin \gamma \end{cases}, \tag{5.6}$$

where parameter β is typically chosen from the interval $\beta \in (0, 1)$. The main benefit of this approach is that the subsequent input does not necessarily need to satisfy the constraints of the object plane. This flexibility allows for faster convergence of the algorithm and enhances its ability to avoid stagnation in local minimal solutions.

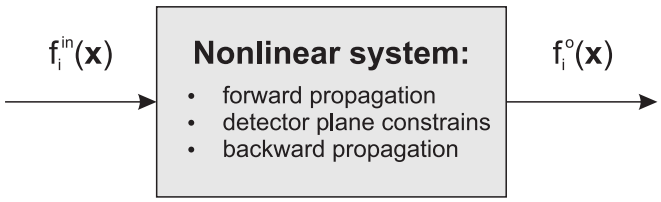

Fig. 5.2: The block diagram illustrates both propagations and detector plane constraints as one nonlinear system.

5.1.3 Output-Output (OO) algorithm

Another alternative is the Output-Output algorithm, which is based on the same idea as the IO algorithm. The only difference is that the Output-Output algorithm applies the output to generate the next input, according to following equation

$$f_{i+1}^{in}(\boldsymbol{x}) = \begin{cases} f_i^o(\boldsymbol{x}) & \text{if } \boldsymbol{x} \in \gamma \\ f_i^o(\boldsymbol{x}) - \beta f_i^o(\boldsymbol{x}) & \text{if } \boldsymbol{x} \notin \gamma \end{cases}. \tag{5.7}$$

It is important to remind that if $f_i^o(\boldsymbol{x})$ is used as the next input, its output will be the same function, since Fourier transform of $f_i^o(\boldsymbol{x})$ already satisfies the detector plane constraints.

5.1.4 Hybrid Input-Output (HIO) algorithm

The next logical choice, based on previously mentioned Input-Output and Output-Output algorithms, is to generate the next input by combining these two methods. This results in a Hybrid Input-Output algorithm defined by the following equation

$$f_{i+1}^{in}(\boldsymbol{x}) = \begin{cases} f_i^o(\boldsymbol{x}) & \text{if } \boldsymbol{x} \in \gamma \\ f_i^{in}(\boldsymbol{x}) - \beta f_i^o(\boldsymbol{x}) & \text{if } \boldsymbol{x} \notin \gamma \end{cases} . \tag{5.8}$$

5.1.5 Propagation in phase retrieval algorithms

It is worth noting that the introduced phase retrieval algorithms are not strictly restricted to Fraunhofer diffraction theory (propagation realized by Fourier transform). The described methods can be extended to other scalar propagation techniques, including those discussed in Section 3.2. As a result, the propagation can be replaced with a propagation operator $\mathcal{P}_z$ along the z-axis, allowing for the selection of the desired method based on specific requirements. This versatility enables for a wider range of applications and provides flexibility in adapting the algorithms to different experimental configurations.

5.1.6 Additional object plane constrains

The main differences between different types of phase retrieval algorithms are primarily determined by the constraints imposed on the object plane, as evident from the previously mentioned algorithms.

The simple support constraints introduced in the ER algorithm are typically quite loose, and the shrink-wrap algorithm is often employed instead [74, 75]. In this algorithm, the support is progressively updated by thresholding during the reconstruction process. Another constraint that can be applied in certain cases is the assumption that the object is a real nonnegative function [10]. This assumption is quite strong but can greatly improve the convergence of the algorithm by narrowing down the space of possible solutions.

All of the discussed constraints and algorithm can be in principal combined according to specific cases, and they can also be introduced with relaxation parameter, following a similar approach described in [76]. This relaxation means that the constraints are weakened when applied to the current object field reconstruction.

5.1.7 Oversampling

Based on the theory of Fourier analysis, a band-limited continuous signal can be fully reconstructed from an infinite sequence of samples if the sampling frequency is at least twice the highest frequency present in the original signal. This principle is known as the Nyquist-Shannon theorem and the limit sampling frequency is known as Nyquist frequency. However, in practical measurements, we often deal with continuous signals with limited support[2], resulting in a discrete spectrum of infinite frequencies. In such

[2]The limited support allows for the periodic extension of such signals.

cases, we choose a maximal sampling frequency, where higher frequencies become negligible or unimportant. This choice inevitably leads to the loss of fine details. Therefore, special attention must be paid to ensure that the loss of details does not significantly affect the accuracy of the measurements.

From another point of view [77], the phase problem is in the reality represented by performing a discrete Fourier transform on discrete arrays of values, as described by the following equation

$$|F_{(K_1,K_2,\ldots,K_m)}| = \left| \sum_{n_1=0}^{N_1-1} \cdots \sum_{n_m=0}^{N_m-1} f_{(n_1,n_2,\ldots,n_m)} e^{-i\frac{2\pi n_1}{N_1}K_1 - i\frac{2\pi n_2}{N_2}K_2 \cdots - i\frac{2\pi n_m}{N_m}K_m} \right| \quad , \tag{5.9}$$

where $\boldsymbol{k}, \boldsymbol{n}, \boldsymbol{N} \in \mathbb{N}_0^m$ and m is the dimension of the array. The equation (5.9) can be considered as a set of equations for unknown variables $f_{\boldsymbol{n}}$ at each point. Due to the absence of phase information, there are trivial ambiguities in the solution, given by relations $f_{\boldsymbol{n}+\boldsymbol{n_0}}e^{i\theta_c}$ and $f^*_{-\boldsymbol{n}+\boldsymbol{n_0}}e^{i\theta_c}$, where $\boldsymbol{n_0}$ and θ_c are constants.

Generally, for an m-dimensional array, there are $\prod_{i=0}^{m} N_i$ equations given by known values of $|F_{\boldsymbol{K}}|$ for $2\prod_{i=0}^{m} N_i$ unknown variables. The total number of unknown variables is twice as large because each variable $f_{\boldsymbol{n}}$ has both a real and an imaginary part. Let us define

$$\sigma = \frac{N_{\text{total variables}}}{N_{\text{unknow variables}}} \quad , \tag{5.10}$$

where $N_{\text{total variables}}$ and $N_{\text{unknow variables}}$ are the total number of variables and total number of unknown variables, respectively.

To ensure a solvable set of equations (5.9), the number of unknown variables needs to be reduced by incorporating partial knowledge of the object support. For instance, if it is known that certain pixels outside a specific region have zero values, this information can be utilized. The solvability of the set of equations, from analysis above, is determined by the oversampling condition $\sigma > 2$.

5.1.8 Error measurement during a phase retrieval

In this thesis, we have used the normalized sum-of-squares error [10,71,78] as a measure the progress of error evolution during the iterations of phase retrieval algorithms. By monitoring this error metric, we can assess the convergence and optimization performance of the algorithms.

5.1.8.1 Normalized sum-of-squares error in the detector plane

The equation defining the normalized error of the i-th iteration in the detector plane is given by

$$E^2_{D,i} = \frac{\int_{-\infty}^{+\infty} \left(\sqrt{I_{ref}(\boldsymbol{\xi})} - |f_i(\boldsymbol{\xi})| \right)^2 \mathrm{d}\boldsymbol{\xi}}{\int_{-\infty}^{+\infty} I_{ref}(\boldsymbol{\xi}) \mathrm{d}\boldsymbol{\xi}} \quad . \tag{5.11}$$

5.1.8.2 Normalized sum-of-squares error in the object plane

The equation defining the normalized error of the i-th iteration in the object plane is given by

$$E_{O,i}^2 = \frac{\int_{-\infty}^{+\infty} \left| f'_{i+1}(\boldsymbol{x}) - f_i(\boldsymbol{x}) \right|^2 \mathrm{d}\boldsymbol{x}}{\int_{-\infty}^{+\infty} |f_i(\boldsymbol{x})|^2 \mathrm{d}\boldsymbol{x}} \quad . \tag{5.12}$$

5.2 Ptychographic coherent diffractive imaging

Currently, ptychographic coherent diffractive imaging, often simply referred as ptychography, is becoming widely used as a coherent diffractive imaging method due to its robustness in the reconstruction process.

The first idea of ptychography was described by W. Hoppe and R. Hegerl in 1969 [79, 80], where they suggested the possibility of solving the phase problem in X-ray crystallography by combining multiple diffraction patterns. Due to limitations in computing power, the development of ptychography as a practical imaging technique took place later, in the late 1990s and the early 2000s. During that time, J. M. Rodenburg and colleagues made significant progress by introducing computational algorithms for ptychographic reconstruction [81–84]. However, currently, among the many algorithms available, the most popular and efficient ones used in ptychography are the Ptychographic Iterative Engine (PIE) [83], extended PIE (ePIE) [85], and the Difference Map algorithm (DM) [86]. These algorithms have demonstrated robustness, convergence, and the ability to handle different experimental conditions and sample types.

The basic mechanism of ptychography consists of scanning multiple diffraction patterns at different positions, and therefore the ptychography is in principal scanning coherent diffractive microscopy. The key idea is to overlap the illumination area of one scan position with the adjacent scan position. This creates real space constraints and redundancy in the information contained in recorded diffraction patterns. The redundancy in the obtained diffraction patterns replaces oversampling, in the case of CDI, and allows us to reconstruct a high-resolution image. Moreover, there are no limitations on the size of the object, and the scanning region size can be arbitrary.

Ptychography, as a coherent diffractive imaging method, offers several advantages over traditional imaging techniques discussed at the beginning of this chapter, particularly when EUV radiation is used. Furthermore, one significant advantage is the capability to retrieve the complex field of both the object and the probe, which is especially important for imaging phase objects. The main applications can be found in biology, the semiconductor industry, and nanosciences.

5.3 Ptychography algorithms

The general idea of ptychography algorithms is to express the exit optical field behind an object as the product of the object field and the probe field at n-th scanning position by the equation

$$f(\boldsymbol{x}, 0) = O(\boldsymbol{x})P(\boldsymbol{x} - \boldsymbol{x_n}) \quad , \tag{5.13}$$

where $O(\mathbf{x})$ represents the complex field of the object and $P(\boldsymbol{x} - \boldsymbol{x_n})$ represents the probe complex field shifted by the position vector $\boldsymbol{x_n}$. Next, let us denote a series of corresponding measured intensity diffraction patterns as $I_{ref,n}(\boldsymbol{x})$ at n-th scanning position. These diffraction patterns provide constraints for the reconstructed field $f(\boldsymbol{x}, 0)$, as they contain information about the interaction between the object and the probe.

This relatively general task formulation can be solved using various approaches, which can be found in [81–86]. However, for the purposes of this thesis, our focus will be on explaining the most widely used methods, as we have applied these algorithms in this study.

5.3.1 Ptychographic Iterative Engine (PIE)

The algorithm known as PIE was introduced by Rodenburg [83] in 2004. This algorithm assumes prior knowledge of the probe field $P(\boldsymbol{x})$ (sometimes equivalently called as an illumination function). The PIE algorithm is illustrated in the block scheme shown in Fig. 5.3 and can be explained in the following steps:

Initialization: The initial optical field guess $O_1(\boldsymbol{x})$ in the object plane is usually created as a free space (alternatively, an approximate guess can be used based on partial knowledge of the object field or additional knowledge of the object field constraints).

1. **Object plane (real space constrains):** The exit field behind the object is created by multiplying current object field guess by the probe field at n-th position and i-th iteration.

$$f_{i,n}(\boldsymbol{x}, 0) = O_i(\boldsymbol{x})P_i(\boldsymbol{x} - \boldsymbol{x_n}) \tag{5.14}$$

2. **Propagation to the detector plane:** The field $f_{i,n}(\boldsymbol{x}, 0)$ is propagated to the detector plane at distance z using the propagator operator $\mathcal{P}_z$, which represents a suitable scalar method introduced in Section 3.2.

$$f_{i,n}(\boldsymbol{x}, z) = \mathcal{P}_z\{f_{i,n}(\boldsymbol{x}, 0)\} \tag{5.15}$$

3. **Detector plane constrains:** The optical field of n-th position in the detector plane is corrected by replacing field amplitudes with the square root of the measured intensity diffraction pattern while optical field phase is preserved.

$$f'_{i,n}(\boldsymbol{x}, z) = \sqrt{I_{ref,n}(\boldsymbol{x})}\frac{f_{i,n}(\boldsymbol{x}, z)}{|f_{i,n}(\boldsymbol{x}, z)|} \tag{5.16}$$

4. **Backward propagation to the object plane:** Inversely to the forward propagation, the modified field at n-th position $f'_{i,n}(\boldsymbol{x}, z)$ is propagated to the object plane by the inverse propagator $\mathcal{P}_z^{-1}$.

$$f'_{i,n}(\boldsymbol{x}, 0) = \mathcal{P}_z^{-1}\{f'_{i,n}(\boldsymbol{x}, z)\} \tag{5.17}$$

5. **Modified object field:** The object field is updated for the (i+1)-th iteration according to the following equation

$$O_{i+1}(\boldsymbol{x}) = O_i(\boldsymbol{x}) + \beta\frac{|P(\boldsymbol{x}-\boldsymbol{x_n})|}{|P_{max}(\boldsymbol{x}-\boldsymbol{x_n})|}\frac{P^*(\boldsymbol{x}-\boldsymbol{x_n})}{\left(|P(\boldsymbol{x}-\boldsymbol{x_n})|^2+\alpha\right)}(f'_{i,n}(\boldsymbol{x}, 0) - f_{i,n}(\boldsymbol{x}, 0)) \quad , \tag{5.18}$$

where β, α are arbitrary chosen parameters and $|P_{max}(\boldsymbol{x})|$ is the maximum amplitude of $P(\boldsymbol{x})$. The parameter β controls the amount of feedback from the previous solution, typically chosen from the interval $\beta \in (0, 1)$, while α is introduced to prevent division by zero in the denominator.

6. **Next scan position:** The algorithm moves to the next position (n+1) where scanning probe beams overlap and repeats steps (1)-(6) with the (i+1)-th object field reconstruction. Note that once the last scanning position is reached, the algorithm returns to the original position.

During the ptychography reconstruction process, the convergence can be determined through sum-of-squares error in both the object plane and the detector plane, similar to CDI (Section 5.1.8).

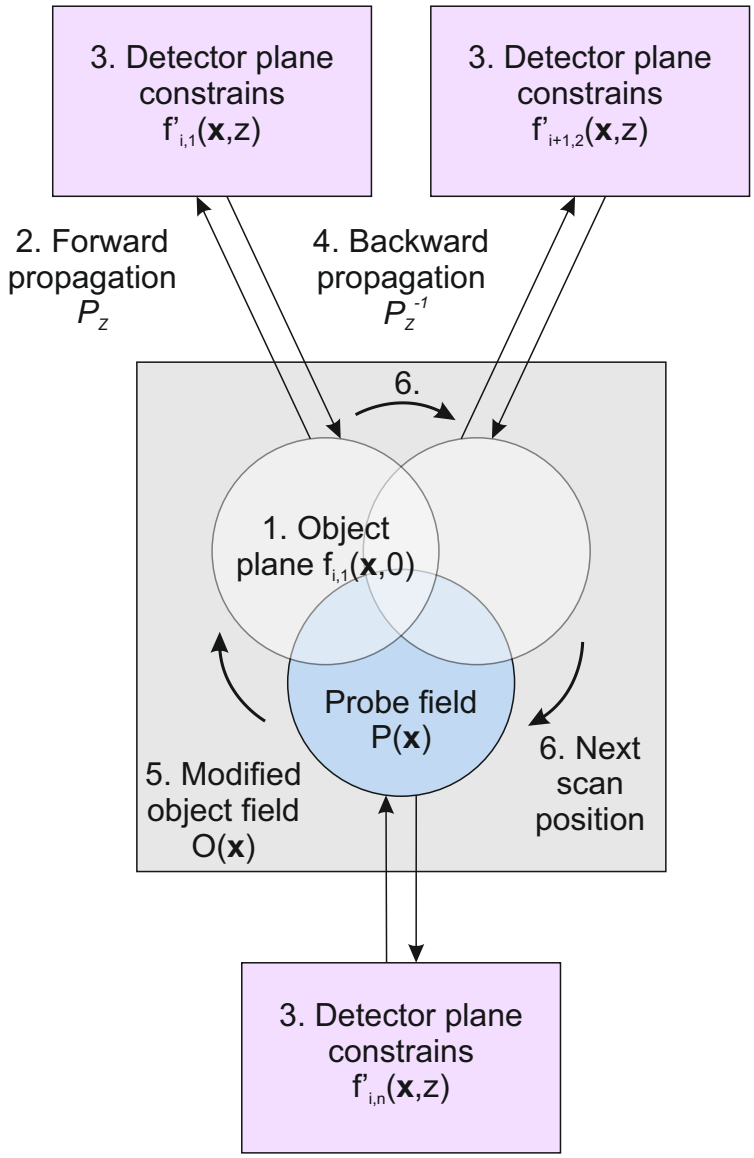

Fig. 5.3: Block diagram of PIE algorithm for ptychographic coherent diffractive imaging.

5.3.2 Extended Ptychographic Iterative Engine (ePIE)

Later, the PIE algorithm was extended in such a way that there is no need for precise knowledge of the probe field, which was firstly introduced in [85].

The initial guess of the object field O_1 is typically considered as free space, similarly to the PIE algorithm. Whereas, the guess of the probe field P_1 is typically chosen as a support function that roughly corresponds to the size of the probe beam. The ePIE algorithm follows the same steps as the PIE algorithm, with the difference being in the 5-th step, where both the object field and the probe field are updated at each iteration

using the following equations

$$O_{i+1}(\boldsymbol{x}) = O_i(\boldsymbol{x}) + \beta_1 \frac{P^*(\boldsymbol{x} - \boldsymbol{x_n})}{|P_{max}(\boldsymbol{x} - \boldsymbol{x_n})|^2}(f'_n(\boldsymbol{x}, 0) - f_n(\boldsymbol{x}, 0)) \quad , \tag{5.19}$$

$$P_{i+1}(\boldsymbol{x}) = P_i(\boldsymbol{x}) + \beta_2 \frac{O^*(\boldsymbol{x} - \boldsymbol{x_n})}{|O_{max}(\boldsymbol{x} - \boldsymbol{x_n})|^2}(f'_n(\boldsymbol{x}, 0) - f_n(\boldsymbol{x}, 0)) \quad , \tag{5.20}$$

These fields are also updated at random scan positions, which can be mathematically written as

$$n = \pi_N(i \bmod N) \quad , \tag{5.21}$$

where $(i \bmod N)$ denotes modulo operation, which returns the remainder of the division of i by N. The set π_N represents a permutation of all scan positions described by the set $\{1, 2, \cdots, N\}$, and $\pi_N(i \bmod N)$ refers to the $(i \bmod N)$-th element of the set. The permutation of the set π_N is renewed when $(i \bmod N) = 0$. The relaxation parameters β_1 and β_2 are typically chosen from the interval $(0, 1)$.

5.3.3 Scanning patterns

The scanning pattern used in ptychography plays a crucial role in the effectiveness of the measurement. The choice of scanning pattern depends on various factors, including the size of the sample, the desired spatial resolution, and the experimental constraints. Commonly used scanning patterns are raster scanning [83], concentric scanning [87], and spiral scanning [88]:

1. In raster scanning, the probe beam systematically moves in a rectangular grid. This scanning pattern ensures that the diffraction patterns are captured at regular intervals. Raster scanning is widely used and provides good spatial coverage of the sample.

2. In concentric scanning, the probe beam is sequentially positioned at a series of concentric circles or rings around a central point on the sample. The advantage of concentric scanning is that it provides a radial sampling of the sample, which can be useful for samples with radial symmetry or regions of interest concentrated around a central point.

3. Spiral scanning, on the other hand, involves the probe beam following a spiral trajectory as it moves across the sample. This scanning pattern allows for a more efficient coverage of the sample area compared to raster scanning [88]. It reduces the time required for data acquisition and can be beneficial for imaging large samples.

5.3.3.1 Probe overlap parameter

In the case of a rectangular scanning grid[3], the probe overlap parameter can be defined as the distance between the centers of two circles (representing the probe beam) [89], according to the following equation

$$o = 1 - \frac{a}{2R} \quad , \tag{5.22}$$

where $a \in [0, 2R]$ is the displacement between the two circles and R is the radius of the probe beam. Note that the overlap defined by (5.22) does not mean overlapping area of the probe beams at two scanning positions.

In the following text, we will express the values of the overlap in percentages. It has been demonstrated [85,89] that an optimal scanning probe beam overlap should be chosen around 60-70 %, while the minimal value that allows reconstruction is around 30 %. However, other non-rectangular scanning patterns can have better performance compared to the rectangular case when a lower overlap parameter is used [88].

5.3.4 Multi-color ptychography

The reconstruction of an image from diffraction patterns created by the superposition of non-interacting multiple wavelengths (incoherent sum) involves solving the phase problem for each independent field (mode) determined by its wavelength [69, 90–92].

In this thesis, we have utilized an algorithm called ptychographic information multiplexing (PIM), which is described in detail in [13,93]. There are several differences in this algorithm compared to PIE/ePIE. The first difference is that the exit field behind the object (1. step of PIE/ePIE algorithm) is given

$$f_{\lambda_m,i,n}(\boldsymbol{x}, 0) = S_{\lambda_m} O_{\lambda_m,i}(\boldsymbol{x}) P_{\lambda_m,i}(\boldsymbol{x} - \boldsymbol{x_n}) \quad , \tag{5.23}$$

where S_{λ_m} represents the spectral weights, and λ_m are discrete wavelengths with $m \in \{1, 2, \cdots, M\}$. These spectral weights are either provided by a known spectrum [69], or in the case of the PIM algorithm, they are updated at each iteration using the following relation

$$S_{\lambda_m,i} = \frac{\sqrt{\int_{-\infty}^{+\infty} |P_{\lambda_m,i}(\boldsymbol{x} - \boldsymbol{x_n})|^2 \mathrm{d}\boldsymbol{x}}}{\sqrt{\sum_m^M \int_{-\infty}^{+\infty} |P_{\lambda_m,i}(\boldsymbol{x} - \boldsymbol{x_n})|^2 \mathrm{d}\boldsymbol{x}}} \quad . \tag{5.24}$$

Next, the incoherent modes are independently propagated into the detector plane using the propagation operator $\mathcal{P}_z$ (2. step of the PIE/ePIE algorithm). In the detector plane, the modes are corrected by the measured intensity diffraction pattern (3. step

[3] For various non-uniform scanning patterns, it is important to take into account that this parameter varies across different scan positions and is not a constant value.

of the PIE/ePIE algorithm) according to

$$f'_{\lambda_m,n,i}(\boldsymbol{x},z) = \sqrt{I_{ref,n}(\boldsymbol{x})}\frac{f_{\lambda_m,n,i}(\boldsymbol{x},z)}{\sqrt{\sum_{m=1}^{M}|f_{\lambda_m,n,i}(\boldsymbol{x},z)|^2}} \quad . \tag{5.25}$$

The algorithm then proceeds with the same steps as the PIE/ePIE algorithm, which include backward propagation (4. step of the PIE/ePIE algorithm) and applying object plane constraints (5. step of the PIE/ePIE algorithm) simultaneously to each individual field. Afterward, the process is repeated for the next position (6. step of the PIE/ePIE algorithm), and this iterative procedure continues until the desired image reconstruction is achieved.

5.4 Resolution of the CDI techniques

The resolution of two points in optical microscopy [46, 47, 94] is typically described by the Rayleigh diffraction limit

$$\Delta r = \kappa\frac{\lambda}{\mathrm{NA}_{obj}+\mathrm{NA}_{cond}} \quad , \tag{5.26}$$

where κ is a coefficient that reflects the shape of the aperture (usually circular or square) and the type of illumination (coherent or incoherent illumination), NA_{obj} denotes the numerical aperture of the microscope objective, and NA_{cond} represents the numerical aperture of the condenser that concentrates light onto the sample. The numerical aperture is defined as

$$\mathrm{NA} = n\sin\theta_{max} \quad , \tag{5.27}$$

where n is refractive index of surrounding medium and θ_{max} is maximal aperture angle (half-cone angle of a light entering an optical system). The coefficient κ for the most common apertures [46, 47, 94] has the following values:

- Incoherent illumination, square aperture: $\kappa_{sq} = 1$
- Incoherent illumination, circular aperture: $\kappa_{circ} = 1.22$
- Coherent illumination, circular aperture: $\kappa_{circ}^{coh} = 1.64$

In the case of resolution of coherent diffraction imaging, the relation given by (5.26) can be used as well. However, the numerical aperture of the condenser NA_{cond} can often be neglected because the sample is typically illuminated by a plane wavefront. This occurs from the fact that the sample is usually positioned in the focal plane, where the wavefront is approximately flat and parallel. Therefore in the case of CDI techniques [47], we can write

$$\Delta r^{CDI} = \kappa\frac{\lambda}{\sin\theta_{max}} = \kappa\frac{1}{\xi_{max}} \quad , \tag{5.28}$$

where ξ_{max} is maximal Fourier spatial frequency transferred by the optical system. In paraxial approximation ξ_{max} can be expressed as

$$\xi_{max} = \frac{\sin\theta_{max}}{\lambda} \approx \frac{\tan\theta_{max}}{\lambda} = \frac{x_{max}}{z\lambda} \quad , \tag{5.29}$$

where x_{max} and z represent the lateral and longitudinal sizes defined by the angle θ_{max}.

6 Measurement of spatial coherence by a non-redundant multi-aperture arrays

Many applications of short-wavelength radiation impose strong requirements on the coherence properties of the source. However, the measurement of such properties poses a challenge, mainly due to the lack of high-quality optics and source fluctuations that often violate assumptions necessary for multi-shot or cumulative techniques.

In this chapter, we present a new method of single-shot spatial coherence measurement adapted to the soft X-ray spectral range. Our method is based on a far-field diffraction pattern from a binary transmission mask consisting of a non-redundant array of simple apertures. Unlike all currently available methods, our technique allows measuring radiation field with an arbitrary spatial coherence function without any prior assumption on intensity distribution or the model of the degree of spatial coherence. We experimentally verified the technique by retrieving the spatial coherence functions of individual shots of laser-driven zinc plasma soft X-ray laser with one- and two-dimensional masks.

6.1 Single-shot coherence retrieval method for X-ray and EUV spectral region

Up to now, several methods have been reported for investigating the spatial coherence through diffraction measurements using a binary mask in the soft X-ray spectral region. The traditional Young's double slit experiment [95] that relies on field stationarity, since multiple points of coherence function need to be measured by a varying the distance between apertures, has been directly adopted for soft X-rays [96–99]. An alternative technique for evaluating the complete coherence function involves comparing the experimental diffraction pattern obtained from a single diffraction pattern of a binary transmission mask, which contains a rich content of spatial frequencies [100], with the calculated diffraction pattern of a fully coherent field. This method has been employed in measurements of a soft X-ray laser [101]. However, both methods require knowledge

of intensity distribution, which is often approximated by homogeneous illumination of the mask.

A more advanced method of the spatial coherence measurement is based on a specially designed non-redundant mask containing an array of N identical apertures [102, 103], which allows measuring the coherence function at $\binom{N}{2}$ points from a single diffraction pattern. However, this method succeeds only if the intensity distribution on the apertures is known or if there is an assumption of rotational invariance for both the intensity and coherence function [104]. It is very challenging at the same time to measure the intensity distribution on the scattering mask and the diffraction pattern in the soft X-ray spectral region. As a result, the intensity measurement is typically replaced by a simplified model that may depart from reality.

In following paragraphs, we present a single-shot method for measuring spatial coherence without requiring prior knowledge of the intensity profile or making any assumptions about the coherence function itself. We experimentally demonstrate the method by measuring the coherence of individual shots from plasma based soft X-ray laser.

6.1.1 Designing a non-redundant array (NRA) of apertures

There are several methods for designing NRAs, such as the method of minimum moment of inertia [105]. In our case, the masks were designed on a uniform discrete grid (orthogonal in the case of two dimensional mask) with spacing of $2d$, where d is the size of the aperture. After placing the first aperture at the origin, an algorithm added apertures on the grid points only if the newly formed aperture array was non-redundant, while gradually increasing the distance from the origin.

6.1.1.1 Design of a 1D non-redundant array

There are many possibilities for choosing a non-redundant array of 1D apertures, and one such design is depicted in Fig. 6.1. In the same figure, the autocorrelation function of the mask is also shown. Additionally, Fig. 6.2 presents an image captured by an optical microscope, illustrating the manufactured non-redundant array of 1D apertures in a thin metal foil.

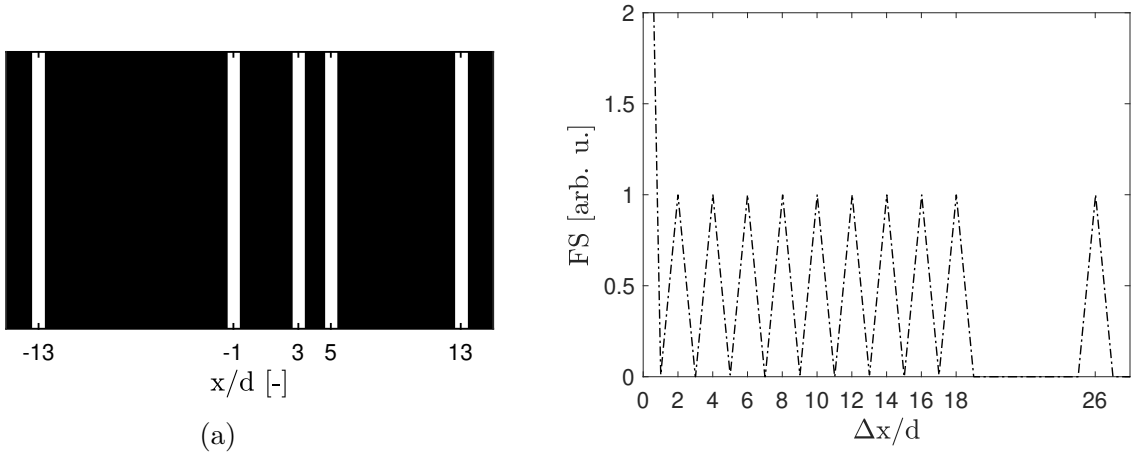

(a) (b)

Fig. 6.1: (a): The theoretical design of the non-redundant 1D array of slits. (b): Autocorrelation function of the designed 1D mask. Nonredundancy can be seen as there is no overlap between the individual autocorrelations peaks formed by two apertures.

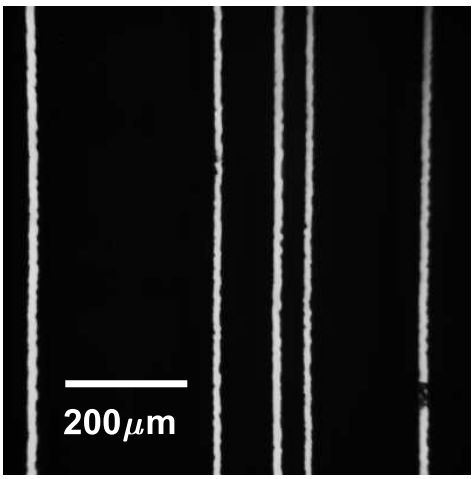

Fig. 6.2: The image obtained from an optical microscope with back surface illumination of the non-redundant array of 1D apertures that were milled by a laser in a thin steel foil.

6.1.1.2 Design of a 2D non-redundant array

Similarly to the 1D mask, the theoretical design of the 2D NRA is illustrated in Fig. 6.3. In the same figure, the autocorrelation function of the mask is also displayed. Additionally, Fig. 6.4 presents an image captured by an optical microscope, illustrating the manufactured non-redundant array of 2D apertures in a thin metal foil.

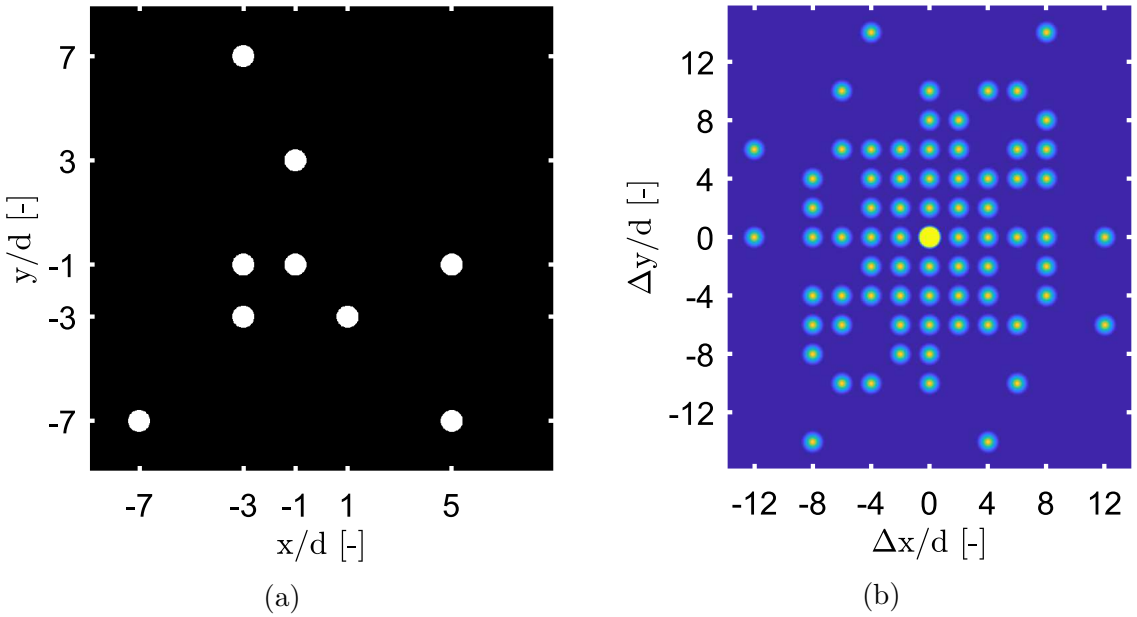

(a) (b)

Fig. 6.3: (a): The theoretical design of the non-redundant 2D array of pinholes. (b): Autocorrelation funtion of the designed 2D mask. Nonredundancy can be seen as there is no overlap between the individual autocorrelations peaks formed by two apertures.

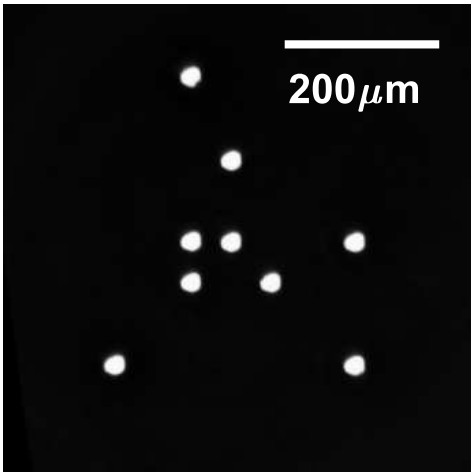

Fig. 6.4: The image obtained from an optical microscope with back surface illumination of the non-redundant array of 2D apertures that were milled by a laser in a thin steel foil.

6.1.2 Fourier analysis of the NRA

Comprehensive studies on this topic have already been performed in [103], and we can now provide a brief summary of the main result. It has been shown, that the Fourier transform of the far-field diffraction intensity pattern from NRA reads

$$\widetilde{I}(\boldsymbol{\rho}) = \Lambda(\boldsymbol{\rho}) \circledast \Big[\sum_{n=1}^{N} I_n \delta(\boldsymbol{\rho}) + \sum_{m=1}^{N-1} \sum_{n=m+1}^{N} \sqrt{I_n I_m}\{\mu_{nm}\delta(\boldsymbol{\rho} - (\boldsymbol{\rho_n} - \boldsymbol{\rho_m})) + \mu_{nm}^{*}\delta(\boldsymbol{\rho} + (\boldsymbol{\rho_n} - \boldsymbol{\rho_m}))\}\Big] \quad , \tag{6.1}$$

where the symbol $\circledast$ denotes convolution, $\Lambda(\boldsymbol{\rho})$ is the square of absolute value of the aperture Fourier transform (i.e. aperture autocorrelation function), $\boldsymbol{\rho_n} - \boldsymbol{\rho_m}$ is the position vector in the Fourier plane, I_n is the intensity in the n-th aperture, μ_{nm} is the complex degree of spatial coherence for the aperture pair nm, and δ is the delta function.

According to the relation (6.1), the resulting pattern consists of individual aperture autocorrelations determined by the $\Lambda(\boldsymbol{\rho})$ function, which is distributed in the Fourier transform of the far-field diffraction pattern with a position vector $\boldsymbol{\rho_n} - \boldsymbol{\rho_m}$. This position vector represents the separation vector between the aperture pair in the input mask. In the case where the mask contains multiple aperture pairs with the same separation vector (redundant array), the multiple aperture autocorrelations formed by individual pairs are overlapping, resulting in the sum of the complex-valued products $\mu_{nm}\sqrt{I_n I_m}$. Therefore, it is important to use a non-redundant array of apertures, which leads to the relation for the spatial coherence [103]

$$|\mu_{nm}| = \frac{|c_{nm}|}{|c_0|} \frac{\sum_j^N I_j}{\sqrt{I_n I_m}} \quad , \tag{6.2}$$

where $|c_{nm}|$ is the peak height formed by the aperture pair nm at $\widetilde{I}(\boldsymbol{\rho_n} - \boldsymbol{\rho_m})$, and $|c_0|$ is the central peak height at $\widetilde{I}(0)$. We will refer to the previous relation as the NRA equation.

6.1.2.1 Mathematical analysis of the NRA equation

In this paragraph, we will get deeper insight into range of function values of the equation (6.2). First, we will readjust the equation to

$$|\mu_{nm}| = \frac{|c_{nm}|}{|c_0|} \frac{\sum_j^N I_j}{\sqrt{I_n I_m}} = \frac{|c_{nm}|}{|c_0|} \frac{1 + \sum_{i,i\neq m}^{N} r_{im}}{\sqrt{r_{nm}}} \quad , \tag{6.3}$$

where

$$r_{im} = \frac{I_i}{I_m} \tag{6.4}$$

is the intensity ratio in the aperture i and m. Clearly, we can find

- when $I_i \leq I_m$, where $I_i \in [0, \infty)$ and $I_m \in (0, \infty) \quad \Rightarrow \quad r_{im} \in [0, 1]$

- when $I_i > I_m$, where $I_i \in [0, \infty)$ and $I_m \in (0, \infty) \quad \Rightarrow \quad r_{im} \in (1, \infty)$

Directly from the definition, the inequality

$$\frac{|c_{nm}|}{|c_0|} \leq 1 \tag{6.5}$$

is always true for any $n, m \in \{1, 2, \cdots, N\}$. Now, let us examine the expression

$$\frac{1 + \sum_{i,i\neq m}^{N} r_{im}}{\sqrt{r_{nm}}} \quad . \tag{6.6}$$

This expression can be rewritten as

$$\frac{1}{\sqrt{r_{nm}}} + \frac{r_{1m}}{\sqrt{r_{nm}}} + ... + \frac{r_{n-1m}}{\sqrt{r_{nm}}} + \sqrt{r_{nm}} + \frac{r_{n+1m}}{\sqrt{r_{nm}}} + ... + \frac{r_{Nm}}{\sqrt{r_{nm}}} \quad . \tag{6.7}$$

The minimal value of (6.7) is guaranteed when $r_{im} \in \{1, 2, \cdots, n-1, n+1, \cdots, N\}$ are equal to zero and $r_{nm} = 1$, which is situation when there are only two apertures illuminated with equal intensity. Next, we can easily find that the range of possible function values for (6.6) is $[2, \infty)$. This implies that from a mathematical point of view, there is no upper limit in the NRA equation (6.3). Therefore, when incorrect intensity values are used, e.g. assuming some model beam intensity profile, it is possible to obtain even non-physical values $|\mu_{nm}| > 1$.

6.1.3 Coherence retrieval algorithm with NRA

The method for retrieving the coherence function is based on analyzing the far-field diffraction pattern produced by a known non-redundant array of apertures. According to the theory described in the Section 3.3, the coherence function can be expressed as a sum of mutually incoherent modes, which can be independently propagated within a given space. Under these circumstances, the algorithm operates on principles analogous to the already described approach of the multi-color ptychography (Section 5.3.4).

To retrieve the coherence function, we employed an iterative algorithm similar to the one used in [8] and to coherent diffractive imaging [9–11], introduced in the Chapter 5. This iterative process allows us to obtain a self-consistent representation of the coherence function that satisfies the constraints in both the NRA mask plane and the detector plane where the intensity diffraction pattern is measured. Ultimately, this determines the degree of spatial coherence and the resulting intensity pattern in the mask plane. The algorithm for this technique consists of following steps (depicted in Fig. 6.5):

Initialization: A suitable base of independent coherent modes $\{f_1, f_2, ..., f_N\}$ in the mask plane has to be chosen. This can be e.g. a set of Hermite-Gauss polynomials with a guess of complex mode amplitudes α_n in accordance with equation (3.32).

1. **Modified mask plane:** The mask plane constrains need to be applied for each mode f_n where $n \in \{1, 2, \cdots, N\}$. These constrains (known binary mask of the NRA) can be described by a support function $\Pi(\boldsymbol{x})$ which is unitary everywhere where the mask is transparent, otherwise it is zero. The modified field of each base function, according to ER phase retrieval algorithm approach, reads

$$f'_{n,i}(\boldsymbol{x}, 0) = f_{n,i}(\boldsymbol{x}, 0)\Pi(\boldsymbol{x}) \quad , \tag{6.8}$$

   where n and i denotes the basis function and the number of iteration, respectively. Equivalently to CDI, in this step, other strategies for the next iteration can be considered, such as widely used HIO algorithm. However, it is necessary to incorporate the precise knowledge of the mask defined by $\Pi(\boldsymbol{x})$.

2. **Propagation to the detector plane:** Each modified base function is then propagated with corresponding scalar method to the detector plane. The propagation method is represented by the propagation operator $\mathcal{P}_z$ as

$$f_{n,i}(\boldsymbol{x}, z) = \mathcal{P}_z\{f'_{n,i}(\boldsymbol{x}, 0)\} \quad . \tag{6.9}$$

   Further, the calculated intensity on the detector plane in distance z from the mask is obtained by incoherent sum of all modes

$$I_i(\boldsymbol{x}, z) = \sum_{n}^{N} |f_{n,i}(\boldsymbol{x}, z)|^2 \quad . \tag{6.10}$$

3. **Detector plane constraints:**

   Let $I_{ref}(\boldsymbol{x}, z)$ denote the recorded diffraction pattern intensity. The retrieved intensity from (6.10) has to be equal to the measured one, therefore the amplitude of each mode across the plane has to be normalized according to the relation

$$f'_{n,i}(\boldsymbol{x}, z) = \sqrt{\frac{I_{ref}(\boldsymbol{x}, z)}{I_i(\boldsymbol{x}, z)}} f_{n,i}(\boldsymbol{x}, z) \quad , \tag{6.11}$$

   while the phase of each field is preserved.

4. **Backward propagation to the object plane:** Inversely to the forward propagation, each modified mode function $f'_{n,i}(\boldsymbol{x}, z)$ is propagated to the mask plane by the inverse propagator $\mathcal{P}_z^{-1}$

$$f_{n,i+1}(\boldsymbol{x}, 0) = \mathcal{P}_z^{-1}\{f'_{n,i}(\boldsymbol{x}, z)\} \quad . \tag{6.12}$$

The algorithm repeats the cycle from step 1 through step 4 in parallel for all independent fields until the calculated far-field diffraction pattern $I_i(\boldsymbol{x}, z)$ matches the measured pattern $I_{ref}(\boldsymbol{x}, z)$ with sufficient precision. A consistent result of the retrieval algorithm can be indicated by reduction of the error residual function below a certain value, analogically to standard phase retrieval algorithms. It should be noted that the condition of oversampling of the measured diffraction pattern needs to be fulfilled, in order to achieve successful convergence. In this case of reconstructing N independent modes, the oversampling condition specified in Section 5.1.7 is adjusted to $\sigma > 2N$.

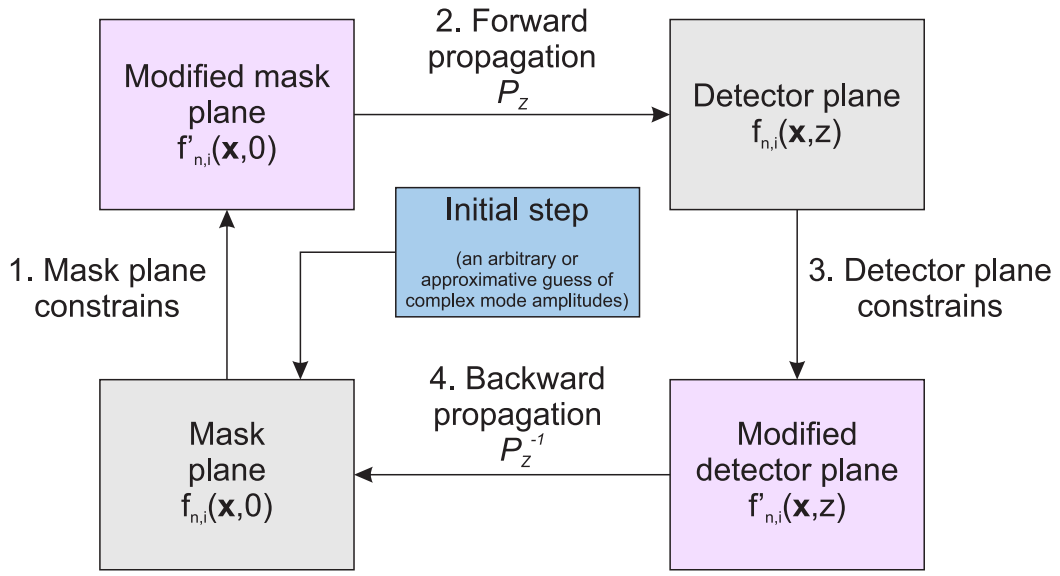

Fig. 6.5: Block diagram of the algorithm for retrieval of coherence function from the diffraction on a non-redundant array of apertures.

6.2 Coherence retrieval simulations

We have verified the proposed technique for coherence retrieval from diffraction on NRA by performing several simulations. For clarity, we present the results from 1D simulations, although 2D simulations were also successfully demonstrated.

In the first step, the theoretical intensity diffraction pattern need to be created by diffraction of spatially partially coherent light. The representation of the partial coherence of the beam at the mask plane is based on the Gaussian Schell-model, introduced in Section 3.3.4. Subsequently, the partially coherent light in modal expansion is propagated using the Fresnel approach to a normalized distance z/d. The normalization of all length dimensions together with wavelength is chosen to exclude any specific size of the aperture d, as this parameter act as a scaling factor of the diffraction task. We have assumed the following theoretical model parameters:

- Spatial coherence length: $l_{coh}/d = 13$
- Beam waist: $w_0/d = 10$
- Number of modes: $N = 10$
- Normalized wavelength-distance product (which is N_F^{-1}): $(\lambda/d)(z/d) = 500$

The resulting theoretical diffraction pattern can be seen in Fig. 6.6.

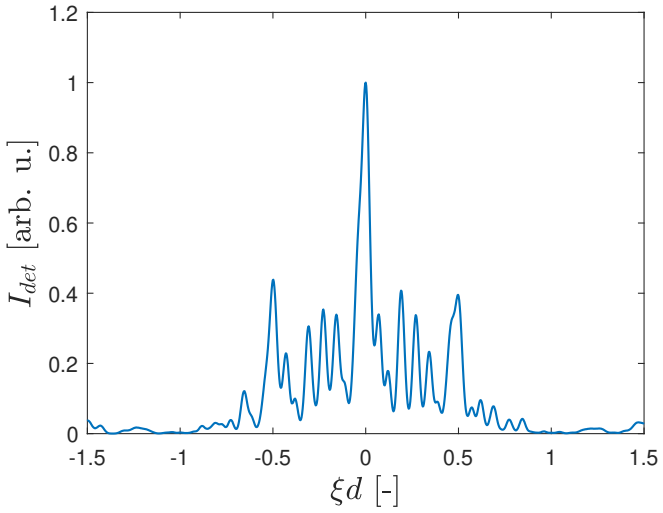

Fig. 6.6: Simulated theoretical diffraction pattern created by the diffraction of spatially partially coherent light on the 1D mask of slits. The partially coherent light is described by the Gaussian Schell-model beam with the following normalized parameters: $l_{coh}/d = 13$, $w_0/d = 10$, $N = 10$, and $(\lambda/d)(z/d) = 500$.

As the second step, the coherence function was retrieved from the obtained intensity diffraction pattern and the knowledge of experimental setup, i.e. normalized wavelength-distance product and NRA geometry. For the purpose of coherence retrieval, a new set of Hermite-Gauss polynomials was created. These modes were generated using a Gaussian Schell-model beam with a difference in the modes amplitudes, either equal or random values. Additionally, different model parameters ($l_{coh,r}$, $w_{0,r}$, and N_r) were intentionally selected for the reconstruction process. These parameters differ from those used for generating the intensity diffraction pattern and were chosen to demonstrate the robustness of the reconstruction algorithm. The parameters of the initial guess for reconstruction are as follows:

- Spatial coherence length of reconstruction modes: $l_{coh,r}/d = 40$
- Beam waist of reconstruction modes: $w_{0,r}/d = 40$

- Number of reconstruction modes: $N_r = 30$

Note that when the coherence length and beam waist were selected to be larger than their original values, it becomes important to appropriately increase the number of modes. This ensures that an adequate solution can be found by the coherence retrieval algorithm.

The theoretical diffraction pattern took into account the influence of photon noise present in the real experiment. Photon noise, given by Poisson distribution, arises from the statistical nature of photon detection and introducing fluctuations in the measured intensity values. This ensured that the coherence reconstruction simulations more accurately represented the reality of the experimental measurements. It was found by simulations that more than total number of 10^6 incident photons recorded by a detector is required for successful reconstruction. Furthermore, the coherence reconstruction algorithm employed the modified mask plane constraint according to Hybrid Input-Output approach.

The results of simulations performed with different photon noise levels are presented in Fig 6.7 and Fig. 6.8. In the figures, it can be found retrieved modulus of degree of spatial coherence, retrieved intensity distribution at the mask plane, and a comparison to the original values. By examining these simulation results, we can clearly see the impact of photon noise on the coherence reconstruction process.

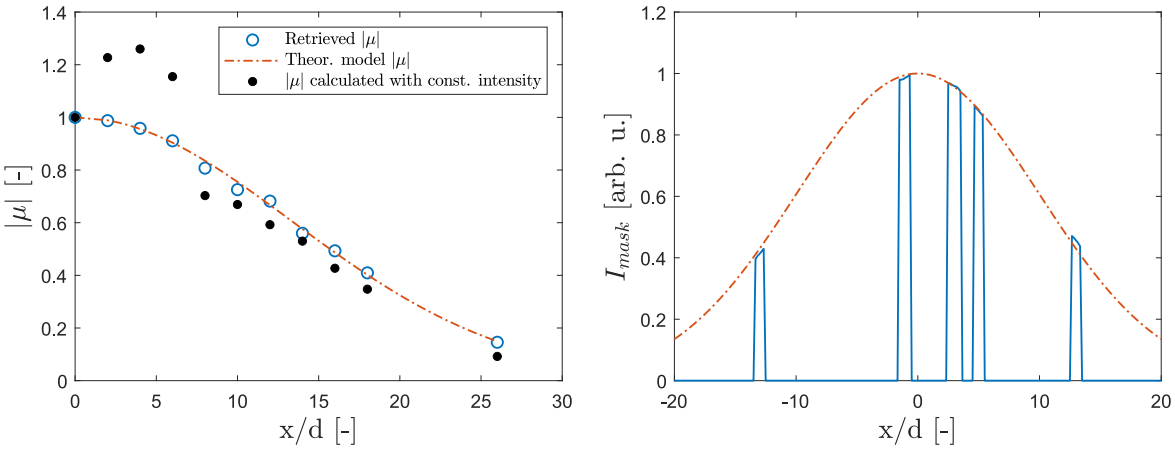

(a) (b)

Fig. 6.7: (a): Retrieved modulus of the degree of spatial coherence from a simulated intensity diffraction pattern with photon noise determined by the total photon flux of 10^8, and its comparison to expected values. (b): Retrieved intensity distribution at the mask plane (blue solid line) and comparison to the originally assumed intensity (red dash-dotted line).

In Fig. 6.7, the result of the calculated modulus of the degree of spatial coherence

assuming constant intensity distribution at the mask is additionally plotted. The calculation is based on equation (6.2). It is important to note that non-physical behavior can be observed, with a few points exceeding the value one. The reason for this behavior was investigated in Section 6.1.2.1, where a mathematical analysis of equation (6.2) was studied. The analysis revealed that mathematically, values higher than one are possible, however this indicating an incorrect (non-physical) intensity distribution at the mask used in the equation.

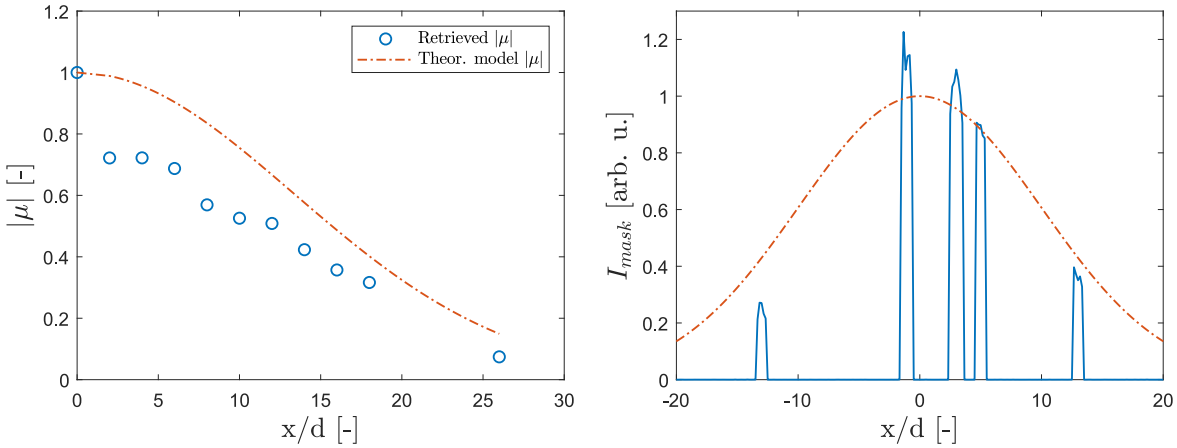

(a) (b)

Fig. 6.8: (a): Retrieved modulus of the degree of spatial coherence from a simulated intensity diffraction pattern with photon noise determined by the total photon flux of $5 \cdot 10^4$, and its comparison to expected values. (b): Retrieved intensity distribution at the mask plane (blue solid line) and comparison to the originally assumed intensity (red dash-dotted line).

6.3 Experimental measurement

In this section, we present experimental measurements utilizing specially designed 1D and 2D masks for EUV radiation (as described in Section 6.1.1). These experiments were performed using a quasi-steady state Ne-like zinc soft X-ray laser at the PALS laboratory. Subsequently, the results were evaluated using the suggested technique of spatial coherence retrieval.

6.3.1 Experimental setup of Ne-like Zn SXRL

We have characterized the beam coherence of the Ne-like Zn plasma-based soft X-ray laser (SXRL) emitting at 21.2 nm [106] by using one-dimensional and two-dimensional masks. The Zn SXRL at PALS laboratory is generating pulses with length of 150

ps in single or double pass geometry. During our experimental measurements, the SXRL source was operated in the double pass amplification by reflecting the laser radiation using a MoSi multilayer mirror placed near one end of a 3 cm long plasma column at normal incidence. The schematics of the experimental setup is depicted in Fig. 6.9, where a plasma column in Zn solid target is created by iodine laser (1.315 μm) in suitable focusing geometry. Firstly, a few Joule prepulse ionizes target and then consequently main pumping pulse with energy of 500 J heats a plasma and thus population inversion is created by electron-ion collisions in the heated plasma.

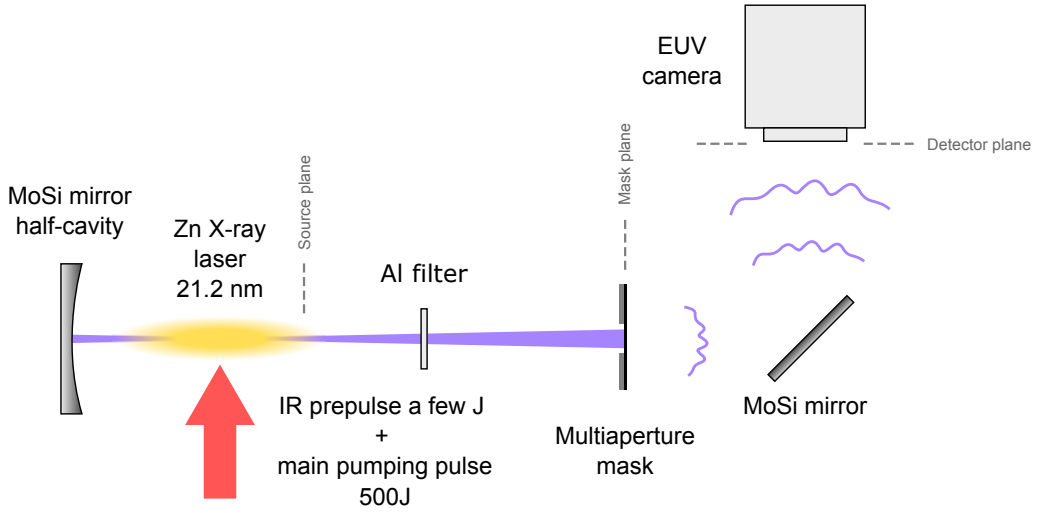

Fig. 6.9: Experimental setup of the single-shot method for the spatial coherence measurement of the Zn soft X-ray laser (21.2 nm).

The NRA consisted of slits (for the 1D measurement) or circular apertures (for the 2D measurement) was positioned 1.5 m downstream from the SXRL source. To eliminate the driving laser radiation and reflect the radiation within a narrow bandwidth centered at the SXRL lasing line, a 45-degree MoSi multilayer mirror with a thin Al filter was employed. The diffraction pattern was recorded using a back-illuminated CCD camera placed 6 meters behind the NRA.

Both 1D and 2D masks were manufactured by laser milling on a steel sheet with a thickness of a few micrometers (Section 6.1.1). The apertures in the masks had a width of $d = 25\ \mu m$ and the smallest spacing between them of $2d$, which equals 50 μm (Figs. 6.1 and 6.3).

6.3.2 Retrieved spatial coherence of Ne-like Zn SXRL

The single-shot diffraction patterns in horizontal and vertical direction for the 1D mask, as well as the diffraction pattern obtained from the 2D mask, were used to retrieve both the spatial coherence function and the ratios of intensities on the apertures employing the retrieval procedure described in the Section 6.1.3.

The Fourier transforms of the diffraction patterns which resemble the autocorrelation function of the masks are shown in Fig. 6.10 and 6.11 together with the retrieved intensity distribution on the apertures for each measurement. The degree of spatial coherence, retrieved from the recorded diffraction patterns, can be found in Fig. 6.12 and Fig. 6.13 in the case of 1D and 2D mask, respectively. It is worth noting that the intensity distribution on the apertures is an inseparable part of each measurement, as no prior assumptions are made regarding the beam intensity.

It is evident that the spatial coherence function of the beam exhibits substantial differences between the vertical and horizontal directions. This behavior is due to the asymmetry of the source, which has been previously observed directly [107]. The source asymmetry may arise from inhomogeneous pumping of the lasing medium or strong transverse plasma density gradients, affecting the propagation of soft X-ray radiation within the plasma.

To get more insight into the results, the resulting degree of spatial coherence for each measurement (corresponding to each laser shot) is fitted by a simple model assuming a coherence function of an uncorrelated radiation source consisting of two spatially separated sources with symmetrical Gaussian intensity profiles. In this case, the degree of coherence is calculated by employing the van Cittert-Zernike theorem [41]. The parameters characterizing the fitted source model are listed in Tab. 6.1 for each measurement. Although the number of data points of spatial coherence function (10 points for the 1D measurement and 36 points for the 2D measurement) could allow for a more complex model with additional degrees of freedom, we believe that our model (with 4 degrees of freedom in the 1D case and 5 degrees of freedom in the 2D case) adequately represents the coherence properties of the source. This is supported by very good agreement between the fitted model and measured coherence function data, as depicted in Figs. 6.12 and 6.13. Moreover, when 1D and 2D experimental results are compared, the spatial separation of the two sources in the vertical direction and the obtained parameters of the fitting model are illustrating similar behavior. The main differences lie in the size and relative intensity of the two Gaussian sources. These differences can be attributed to the substantial shot-to-shot fluctuations that are typical for the soft X-ray lasers.

One can notice that the measured degree of the spatial coherence shown in Fig. 6.12 and Fig. 6.13 does not asymptotically approach unity at zero separation of apertures. We believe this is due to incoherent radiation from the plasma that is still reflected by the multilayer mirror and various sources of detection noise.

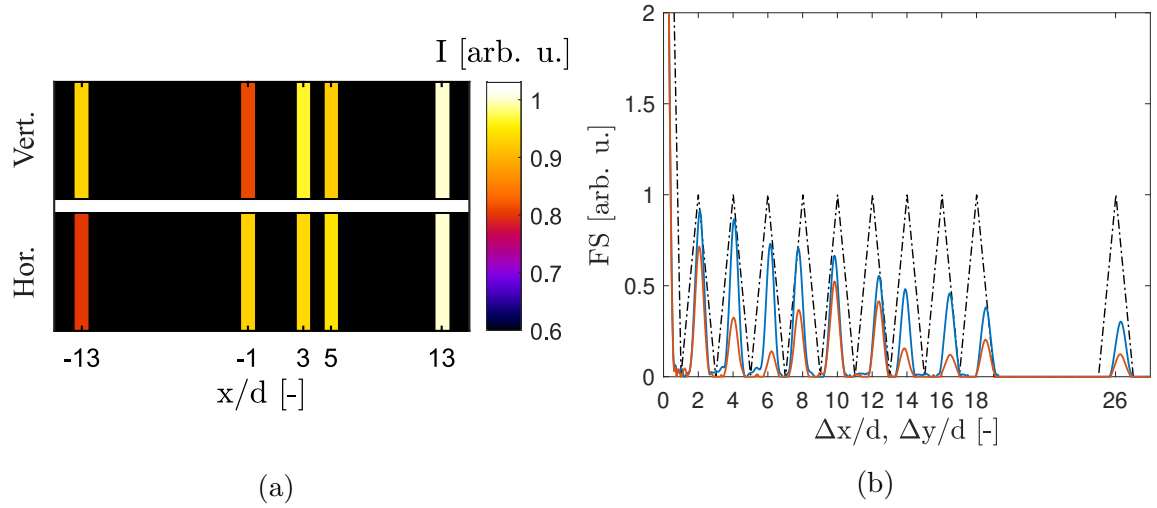

(a) (b)

Fig. 6.10: (a): The 1D mask of slits with retrieved intensity of the Zn SXRL in vertical and horizontal orientation. The aperture size is $d = 25\ \mu m$. (b): Autocorrelation function of the 1D mask of slits (dashed dotted black line) and Fourier spectrum of the measured diffraction pattern (FS) of the measurement performed in the horizontal (blue line) and the vertical orientation (red line).

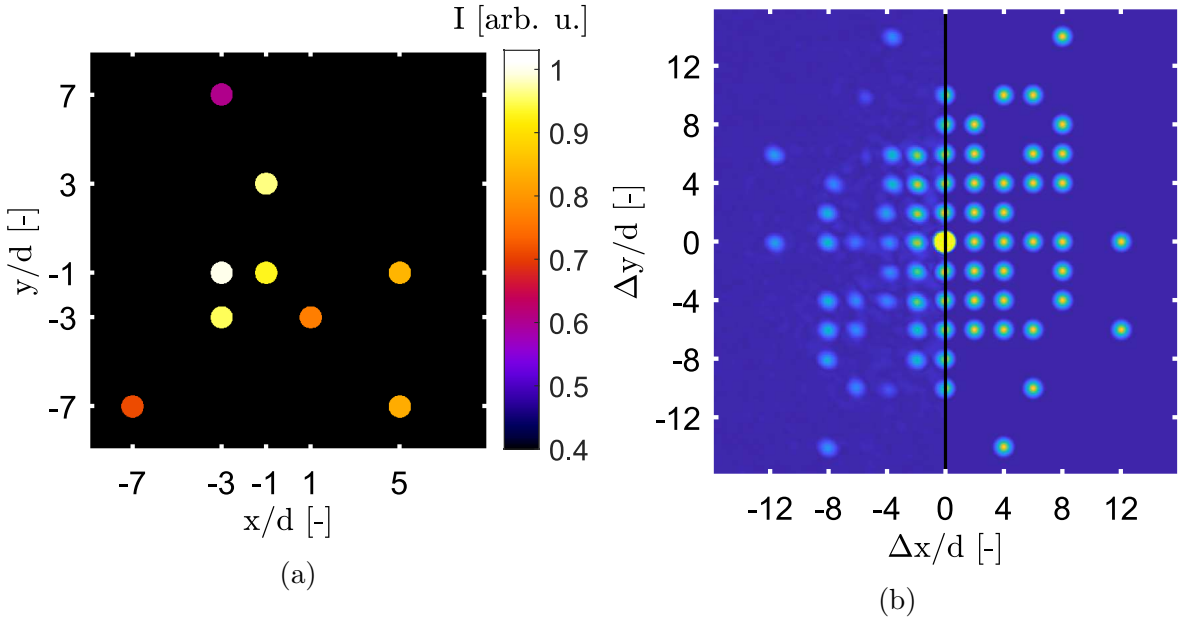

(a) (b)

Fig. 6.11: (a): The 2D mask of circular apertures with retrieved intensity of the Zn SXRL. The aperture size is $d = 25\ \mu m$. (b): Autocorrelation function of the 2D mask of circular apertures (right part of the image) and Fourier spectrum of the measured diffraction pattern (left part of the image).

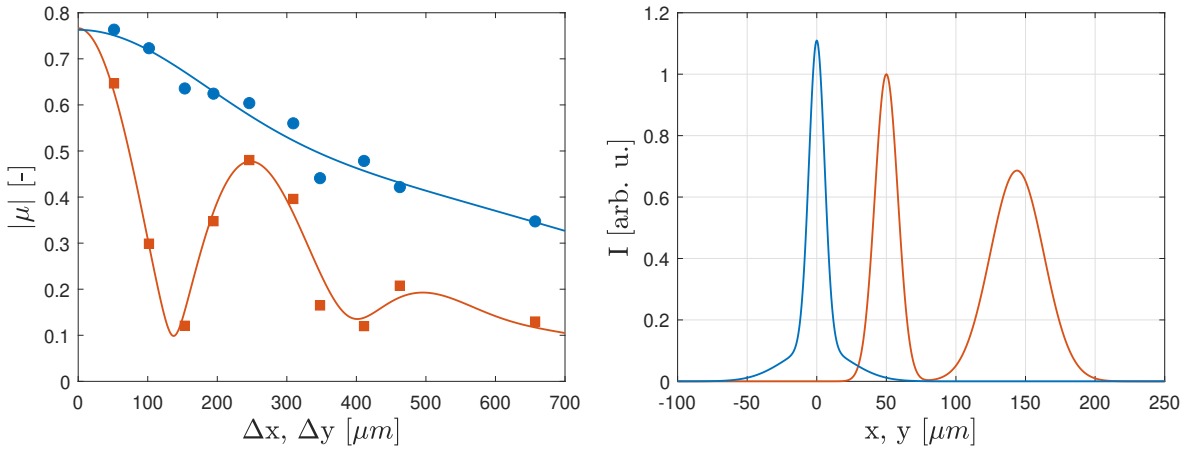

(a) (b)

Fig. 6.12: (a): Modulus of degree of spatial coherence $|\mu|$ at the mask plane of Ne-like Zn SXRL retrieved from diffraction patterns of the measurements performed in horizontal (blue circles) and vertical (red squares) orientation of the 1D mask. The retrieved values of $|\mu|$ are fitted (red and blue solid lines) by theoretical source models, which were used as inputs for the far-field van Cittert-Zernike theorem. It was used $N_{1D} = 25$ modes for the coherence retrieval algorithm. (b): 1D intensity distributions at the source plane of Ne-like Zn SXRL in vertical (red line, plotted with offset of 50 μm) and horizontal (blue line) found by fitting the $|\mu|$.

Theoretical source model		$\frac{B}{A}[-]$	w_A	w_B	x_0	y_0
1D (hor.):	$Ae^{-2\frac{x^2}{w_A^2}} + Be^{-2\frac{(x-x_0)^2}{w_B^2}}$	0.11	11	24	0.03	-
1D (vert.):	$Ae^{-2\frac{y^2}{w_A^2}} + Be^{-2\frac{(y-y_0)^2}{w_B^2}}$	0.67	17	39	-	94
2D:	$Ae^{-2\frac{x^2+y^2}{w_A^2}} + Be^{-2\frac{(x-x_0)^2+(y-y_0)^2}{w_B^2}}$	0.74	33	34	-6.3	91

Tab. 6.1: Parameters of the model source consisting of two spatially separated Gaussian sources found by fitting the degree of spatial coherence retrieved from the experimental data. The units of w_A, w_B, x_0, y_0 are in μm.

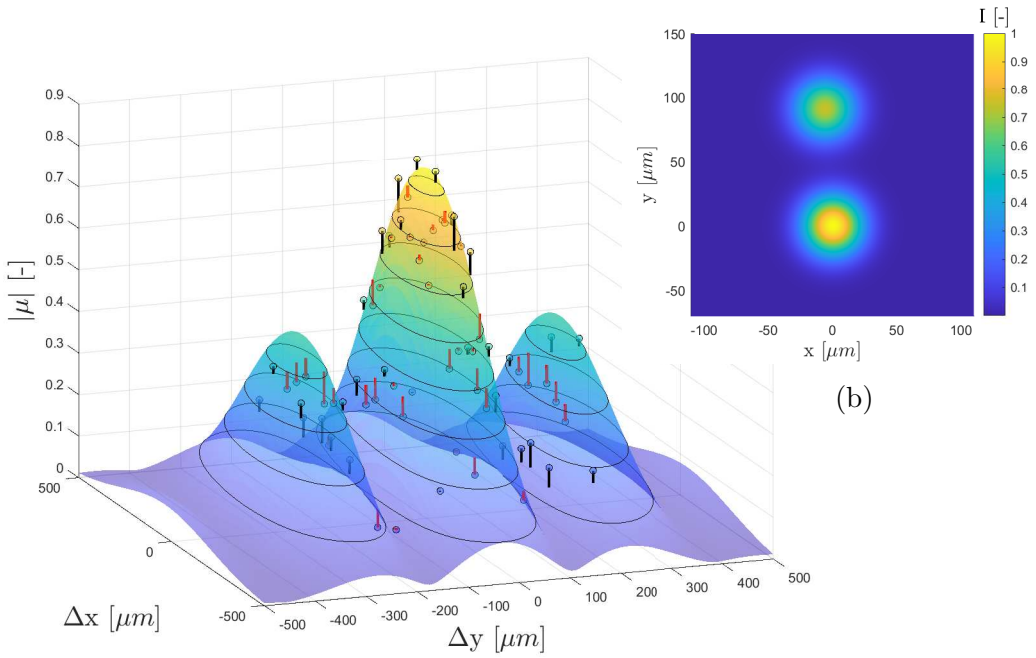

Fig. 6.13: (a): Modulus of degree of spatial coherence $|\mu|$ at the mask plane retrieved from the diffraction patterns of 2D measurement (black circles) and fitted by theoretical source model used as input for the far-field van Cittert-Zernike theorem (surface plot). Red and black lines show the differences between the measured values and the fit. It was used N_{2D} = 20x20 modes for the coherence retrieval algorithm. (b): 2D intensity distribution at the source plane of Ne-like Zn SXRL found by fitting the $|\mu|$.

7 HHG Beamline at ELI Beamlines facility

In this chapter, we provide a brief description of the user-oriented HHG Beamline at ELI Beamlines facility. For more detailed information, refer to [108]. Firstly, we describe the setup of the HHG Beamline, followed by a summary of the diagnostic methods used to characterize the generated beam. Finally in this chapter, we discuss the monochromatization of the high harmonics, which is an important feature required for many experiments performed at the beamline.

7.1 HHG Beamline setup

The HHG Beamline is producing EUV radition in a gas cell or Even-Lavie gas jet [109] through a long focusing geometry [110] which allows an enlarged interaction between noble gases and laser field during its propagation on Rayleigh range (interaction volume is increased while intensity and thence medium ionization is kept at optimal level) [111]. The main driving beam of HHG Beamline is L1 Allegra laser system based on optical parametric amplification (OPA) generating pulses of 1 kHz repetition rate, 100 mJ energy, 15 fs duration and a central wavelength of 830 nm [112]. Additional driving beam can be generated by commercial Ti:Sapphire based laser system of 1 kHz, 10 mJ, 40 fs and a central wavelength of 795 nm.

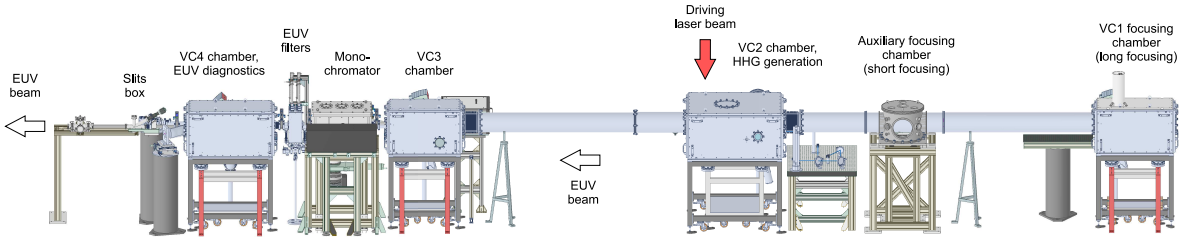

Fig. 7.1: The HHG Beamline designed for a long and short focusing geometry at ELI Beamlines.

The HHG Beamline consists of several vacuum chambers positioned in-line which is illustrated in Fig. 7.1. The driving beam enters the interaction chamber VC2

and then, in dependence of selected focal lengths from 2.5 up to 25 meters, VC1 and VC3 chambers are intended to focus or fold the beam according to the focusing spherical mirror location (VC1 or VC3). Additionally, the distance between VC1 and VC2 chamber can be changed by movable VC1 chamber. In order to maximize the versatility of the experimental setup, an auxiliary chamber for a short focusing was included later in the setup as well.

In addition, the experimental setup in the VC2 chamber shown in Fig. 7.2 of high harmonic generation is designed for two-color driving field of laser fundamental beam and its second harmonic beam.

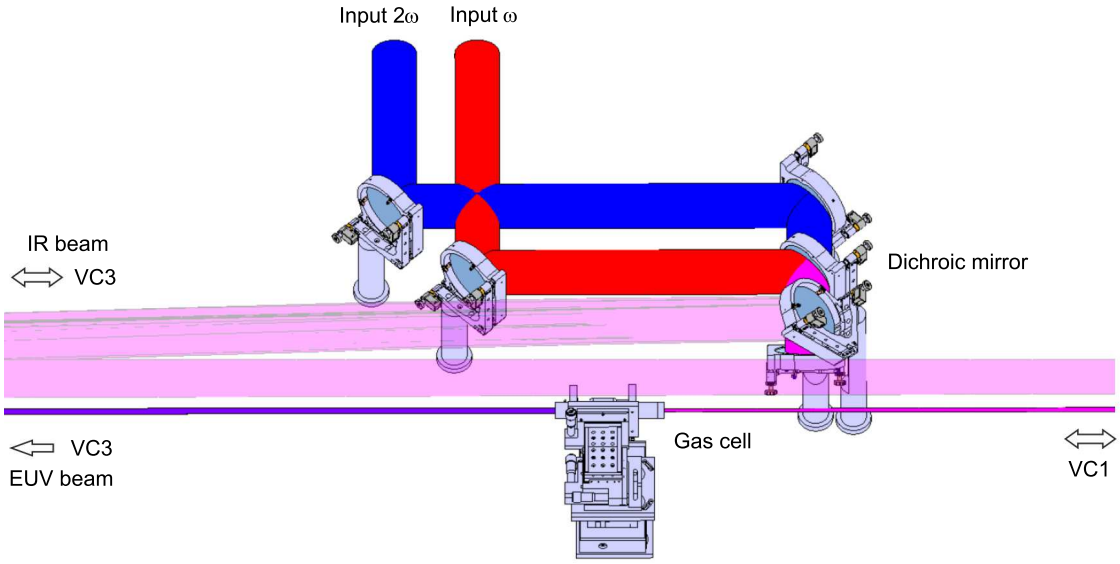

Fig. 7.2: The VC2 experimental setup with two-color HHG driving beam, gas cell and a long focusing geometry (focusing mirror is placed in VC3).

The setup in the chamber VC3 illustrated in Fig. 7.3 includes IR rejection system, folding or focusing mirror and SiC mirror which is aimed to reflect the HHG beam into VUV ellipsometer user station [113, 114]. The IR rejection system consists of three mirrors with a special coating reflecting EUV beam under grazing incidence angle, while an IR beam is transmitted and dumped. The residual IR light is blocked by a thin metallic filters located behind the monochromator. The monochromator plays a key role in experiments involving only a single harmonic beam, and its design is described in a separate section below.

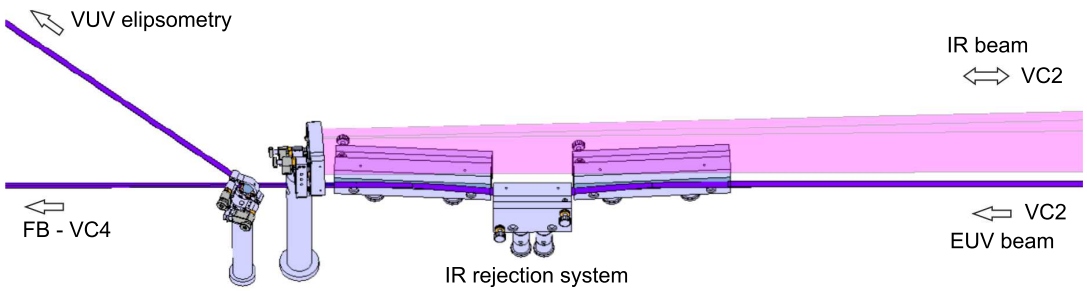

Fig. 7.3: The VC3 chamber with IR rejection system and focusing or folding mirror correspondingly to focusing configuration.

7.2 EUV beam diagnostics

Characterization of the generated harmonic beam is realized in the VC4 chamber. Key diagnostics as EUV spectrometer, EUV wavefront and energy measurement by photodiode are depicted in Fig. 7.4. The EUV beam on axis can be reflected by toroidal mirror or a flat mirror on EUV spectrometer or EUV wavefront sensor, respectively.

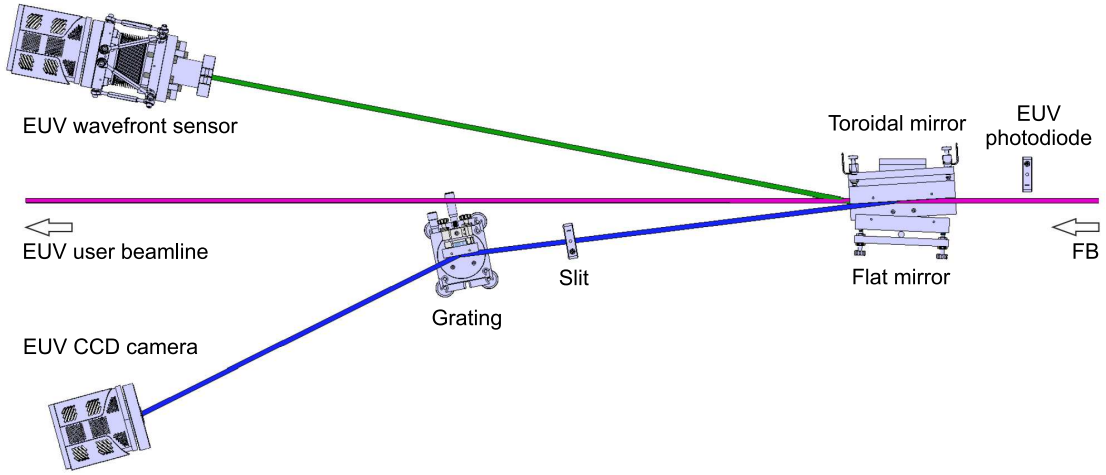

Fig. 7.4: The VC4 chamber containing EUV spectrometer, EUV wavefront sensor and photodiode for energy measurement.

7.2.1 EUV spectrometer

The EUV spectrometer is uniquely designed for achieving exceptional levels of both high resolution and high sensitivity. The total spectral range covered by this instrument is from 5 nm to 120 nm (achieved by two diffraction gratings 1200 lines/mm and 600 lines/mm which correspond to spectral range 5-60 nm and 20-120 nm, respectively). The spectrometer consists of a toroidal mirror, a motorized slit of variable width, a re-

flection grating and a back-illuminated CCD. The toroidal mirror images the incoming EUV beam onto the slit in the vertical direction. The concave grating with variable line spacing disperses the light angularly and images the slit in the horizontal direction onto the chip of the CCD.

The advantage of using the toroidal mirror is a significant increase in the photon flux per pixel, thus increasing the signal-to-noise ratio while not affecting spectral properties of the spectrometer. Furthermore, imaging with a concave spherical grating suffers from strong astigmatism which is compensated by a properly designed toroidal mirror. It was shown by ray-tracing simulation that any astigmatism was almost completely compensated and thus the flux on the CCD camera was increased by several orders of magnitude. An example of the measured HH spectrum generated in Kr gas can be seen in Fig. 7.5.

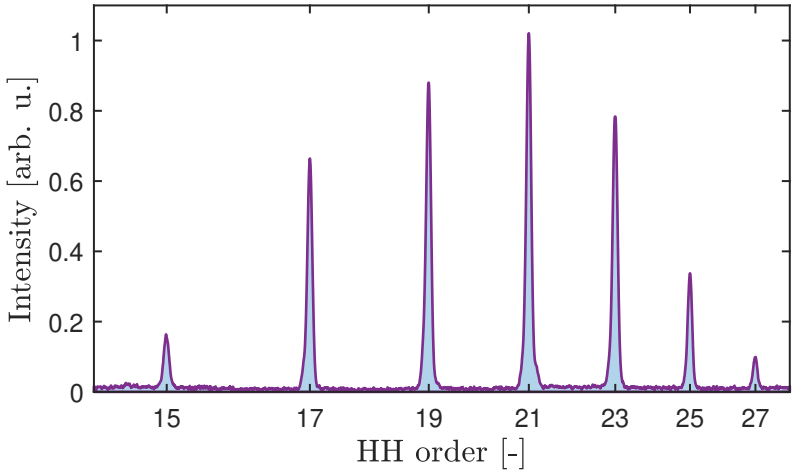

Fig. 7.5: The HH spectrum generated from Kr gas jet and driven by commercial Ti:Sapphire based laser system with a central wavelength at 795 nm. The spectrum was measured using the EUV spectrometer developed for the HHG Beamline at the ELI facility.

7.2.2 EUV wavefront sensor

Last but not least, a diagnostic tool used in the setup is a wavefront sensor mounted on the VC4 and operating under vacuum conditions. The EUV wavefront sensor follows the design principles of the Hartmann sensor, which involves an array of holes in a mask. The characterized EUV beam is diffracted by the Hartmann mask, resulting in the formation of a grid of spots on the CCD. From the positions of these spots and their corresponding intensities measured by the CCD, both the beam wavefront and intensity profile can be reconstructed. This allows for a detailed analysis and understanding of the EUV beam wavefront characteristics.

The wavefront sensor (HASO EUV HA-4627 developed by Imagine Optics) consists of a grid with 60 x 60 holes, with a pitch of 210 μm (determining the spatial sampling) and positioned 43.5 mm in front of the CCD. For diverging EUV beams, the effective number of holes is reduced to 40 x 40 holes, which is sufficient for calculating Zernike polynomials up to the order of 36. The EUV CCD camera used in the setup (Princeton PIXIS XO 1024B) has a resolution of 1024 x 1024 pixels and each pixel of the camera has a size of 13.5 μm.

The wavefront sensor is designed for the wavelength range of 5 nm to 120 nm (energies of 10-250 eV) and offers an absolute wavefront accuracy of 1.2 nm RMS. The input sensor aperture has dimensions of 13 x 13 mm and can measure beam wavefront curvatures ranging from collimated beams (infinity) to 0.45 m.

The measured intensity profile with the corresponding beam wavefront are displayed in Fig. 7.6, where the beam wavefront is plotted after subtracting the effects of tilt and curvature, which are responsible for the beam propagation direction and divergence. It can be seen in Fig. 7.6 that the beam intensity profile and wavefront demonstrate astigmatism. In the future, a deformable mirror will be employed in the optical path of the HHG Beamline driving beam to improve the beam quality and correct the most of abberations.

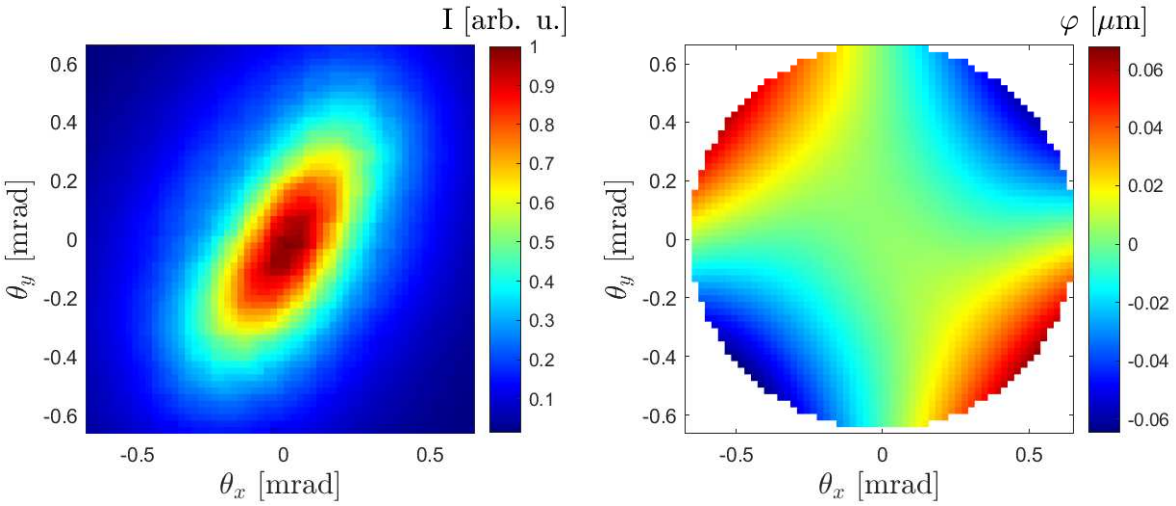

Fig. 7.6: HH intensity beam profile (a) and the beam wavefront (b). The beam intensity profile and wavefront demonstrate astigmatism. The first few evaluated Zernike coefficients at the central wavelength of HH19 are as follows (except tilts and focus): Astigmatism at 0°: 4 nm, Astigmatism at 45°: 62 nm, Coma at 0°: $<$ 1 nm, Coma at 90°: $<$ 1 nm, 3th order spherical aberration: 2 nm.

7.3 EUV monochromator

It is crucial to have the ability to select a specific high harmonic wavelength that is the most suitable for various applications such as coherent diffractive imaging, probing of electronic structures and dynamics of atomic and molecular systems on femtosecond timescales [115–117], etc.

In the HHG Beamline, a monochromator setup based on a single grating is employed. However, it is important to carefully consider the impact on the duration of the EUV pulse. In order to maintain the temporal profile of the pulse as short as possible, a nearly time-preserving design with high transmission was chosen, which is based on the design reported in [118–124]. Nevertheless, to achieve complete pulse duration preservation and temporal tuning capabilities, a monochromator setup equipped with two gratings would be necessary [125]. Unfortunately, this approach would result in a substantial reduction in the output flux of the EUV beam due to its overall low transmission.

7.3.1 Monochromator setup and its optical design

The monochromator is located between VC3 and auxiliary chamber containing EUV filters (see Fig. 7.1). The schematic of the monochromator setup is presented in Fig. 7.7 and picture of the monochromator chamber interior with EUV optics can be found in Fig. 7.8.

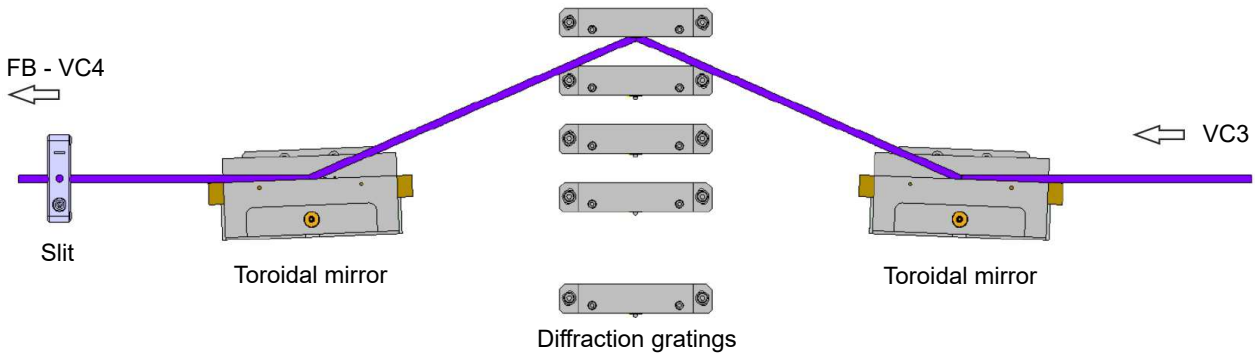

Fig. 7.7: The setup of the monochromator for the HHG Beamline consists of two toroidal mirrors and one diffraction grating with the possibility of grating selection according to the desired spectral range.

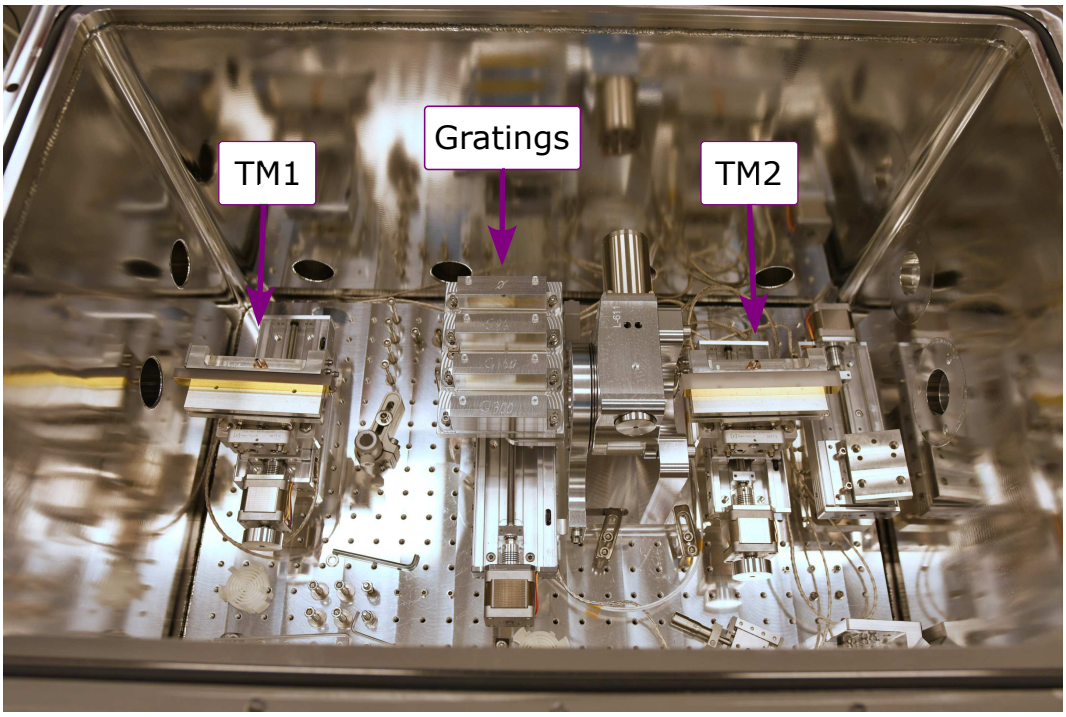

Fig. 7.8: A picture of the monochromator chamber interior. The setup of the monochromator for the HHG Beamline consists of two toroidal mirrors and one diffraction grating with the possibility of grating selection according to the desired spectral range.

First, the incoming EUV beam is collimated by grazing incidence toroidal mirror TM1 and consequently the beam is diffracted by one of four plane diffraction grating (see the list of gratings in the Tab. 8.1) with the conical diffraction geometry (grooves direction is in the plane of incidence). Next, the diffracted beam is focused by the second toroidal mirror TM2 onto a chosen slit located on the original beam axis, creating a virtual source for the refocusing optic. The desired wavelength is selected via adjusting tilt and rotation of the grating. Both gold coated toroidal mirrors are designed for grazing angle of 2.25 degrees and have focal lengths of 4.8 m and 2.4 m for collimating TM1 and second focusing TM2, respectively. Thus, there is a secondary source located at the slit plane that is two times smaller than the original source but has twice the divergence. In order to achieve the desired source size and transmitted bandwidth, slits with widths of 50, 100, 200, and 300 micrometers can be used.

The ray tracing simulations were performed to verify optical performance of the monochromator design and to find precise position of the virtual source behind the TM2. The spot diagram in the focal plane of TM2 is presented in Fig. 7.9. The precise alignment of the monochromatized EUV beam to the slits is ensured by imaging a Ce:YAG scintillator screen using a visible camera placed outside the chamber. The spatial separation of monochromatized high harmonics and spatial-spectral intensity profile of HH19 on the scintillator screen can be seen in Fig. 7.10.

Grating [lines/mm]	Spectral region [eV]	Spectral region [nm]
Grat. 1: 86	10-28	44.3-124
Grat. 2: 158	25-54	23-49.6
Grat. 3: 600	51-98	12.7-24.3
Grat. 4: 985	86-121	10.3-14.4

Tab. 7.1: List of gratings used for the monochromator setup with corresponding spectral ranges considered for their operation.

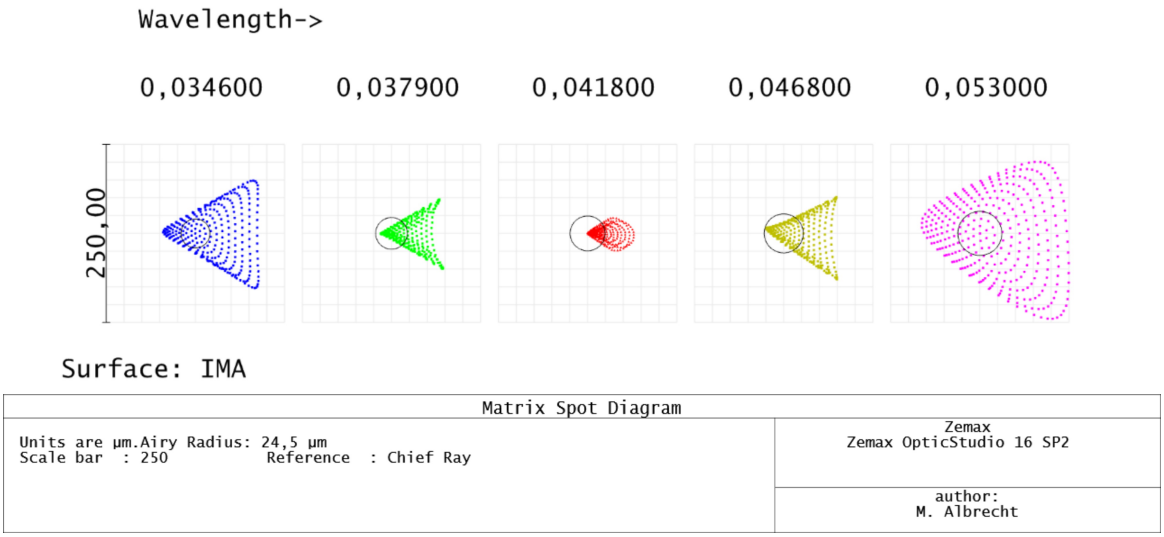

Fig. 7.9: The spot diagram of the ray tracing simulation in the TM2 focal plane with grating of 150 lines/mm. The HH19 (the value of 41.8 nm represents the wavelength of the 19-th harmonic of a fundamental laser beam with a wavelength of 795 nm) is shown in the optimal alignment on the HHG Beamline axis and therefore diffraction limit illustrated by black circle (circle of Airy radius) is reached.

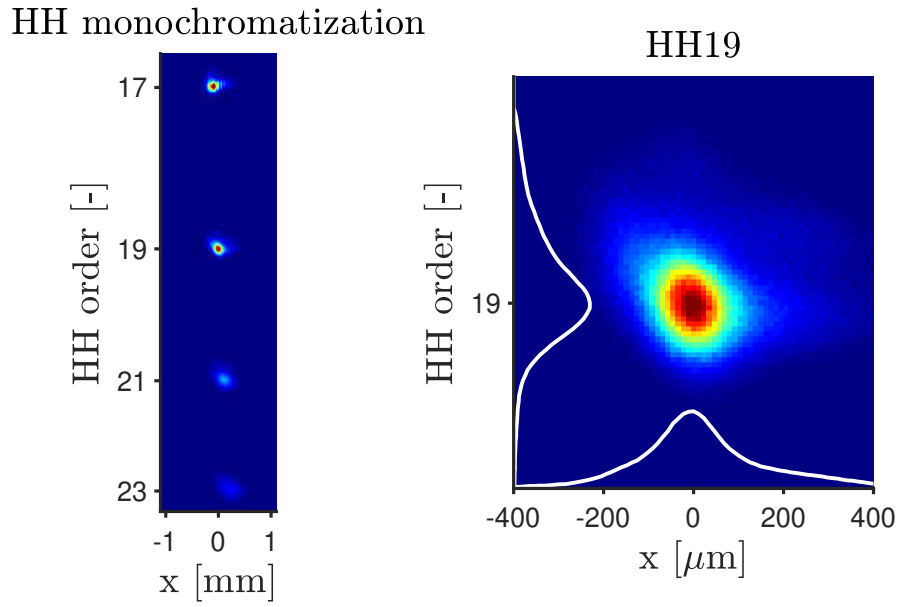

Fig. 7.10: The spatial separation of monochromatized high harmonics (on the left) and spatial-spectral intensity profile of HH19 on the scintillator screen (on the right).

7.3.2 Pulse temporal broadening by diffraction on a single grating

The diffraction through the single grating unavoidably leads to a distortion of the temporal profile of the generated ultrashort pulse. This temporal distortions need to be kept as short as possible and only slight temporal broadening can be accepted in accordance of experimental applications. Thus, time broadening effects need to be carefully considered in the design of monochromator.

The most dominant factor leading to the pulse broadening is the pulse-front tilt, arising from the reality that each ray diffracted by two adjacent grooves encounters a delay of $m\lambda$, where m represents the diffraction order. The cumulative difference in optical path is determined by $|m|\lambda N$, where N corresponds to the number of illuminated grooves. Consequently, the delay introduced by grating dispersion is given by

$$\Delta\tau_{OP} = \frac{\lambda|m|N}{c} \quad . \tag{7.1}$$

The pulse broadening at FWHM of a Gaussian-profiled beam due to the pulse-front tilt caused by diffraction on the grating [126] is described by the following relation

$$\Delta\tau_{Grat-Gauss} = \frac{2\ln 2}{\pi}\frac{\lambda|m|N}{c} \approx 0.44\frac{\lambda|m|N}{c} \quad . \tag{7.2}$$

In HHG Beamline setup, the maximal divergence of generated beam is 1 mrad, which corresponds to illuminated area perpendicular to the grooves approximately 5

mm. For instance, if we consider a grating with a line density 158 lines/mm and a wavelength of 40 nm, according to equation (7.2), the estimated minimal pulse broadening caused by the pulse-front tilt would be below 100 fs.

8 Experimental results of EUV coherent diffractive imaging and ptychography

This chapter is dedicated to the description of the experimental setup for EUV coherent diffractive imaging and ptychography, employing radiation from the HHG Beamline. To demonstrate the imaging capabilities, a simple binary test sample was designed and manufactured. Subsequently, important practical aspects, including EUV focal spot alignment diagnostics, ray-tracing optical simulations of the entire EUV setup, and the wavefront of the EUV probe beam filtered by a pinhole, are also discussed. Finally, the experimental results of coherent diffractive imaging using a monochromatized beam and the reconstruction of multi-color ptychography are presented.

8.1 Design of test samples for diffractive-based microscopy

The appropriate design of the test sample is a key factor in experimental assessment of performance of the lensless imaging setup. In our experimental research, we used binary amplitude samples. The first crucial aspect is accurately determining the material composition of the sample. Clearly, the opaque regions of the sample must be made of a highly absorptive material for the given spectral range of wavelengths. Additionally, a small sample thickness is required. In situations where the sample cannot be assumed to be thin, the asumptions of the diffraction theory expected in this thesis (boundary conditions) may be violated, resulting in noticeably blurred diffraction patterns as the sample exhibits waveguide behavior [127,128]. The sample thickness should be smaller than the theoretical depth of field in classical microscopy [129], as given by

$$T_{DoF} = \frac{n\lambda}{\mathrm{NA}^2} \quad , \tag{8.1}$$

where n is the surrounding medium refractive index and NA is the numerical aperture of the optical system. Next, a gold coating as a high EUV absorbing material with

thickness 300 nm is chosen on commonly available TEM microscopy silicon nitride (Si_3N_4) membranes. These membranes have a form of multi-frame array (MFA) on a silicon substrate of following parameters (illustrated in Fig. 8.1):

- **MFA size:** 14.0 mm x 14.0 mm, Si substrate of thickness 200 μm
- **MFA array:** 4 x 4 TEM frames
- **TEM frame size:** 2.65 mm x 2.65 mm
- **Si_3N_4 membrane size:** 0.25 mm x 0.25 mm, 75 nm thick
- **Coating:** Ti 5 nm thick, Au 300 nm thick

The presence of a 5 nm Ti layer between Si_3N_4 and Au is necessary to improve the adhesion of gold to the substrate [130]. In EUV diffractive-based experiments, the characteristic dimensions of the samples are in the micrometer range. Therefore, it is crucial to employ a suitable technique capable of creating sharp binary structures on gold coated silicon nitride membranes. Experimental measurements for diffractive-based microscopy, described in this thesis, employed samples prepared by the technique of focused ion beam (FIB) milling.

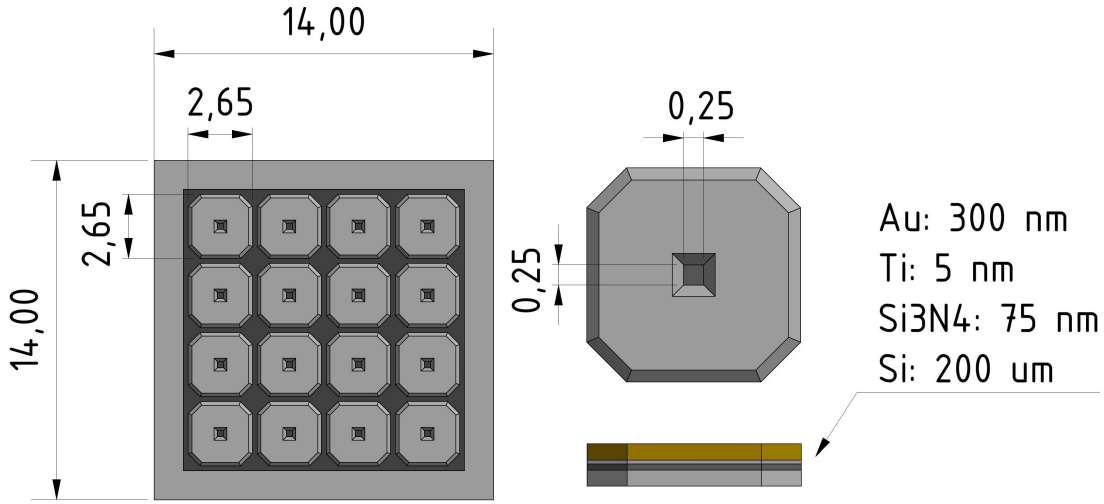

Fig. 8.1: Silicon nitride (Si_3N_4) membranes (usually used for TEM microscopy) with Au coating used for FIB milling.

8.1.1 Characterization of FIB-prepared samples

We have chosen the ELI logo of different sizes for FIB milling as the sample pattern. During the experimental measurements, we mainly focused on using the two smallest patterns. These two samples were characterized by scanning electron microscopy (SEM), and the results can be found in Figs. 8.2 and 8.3.

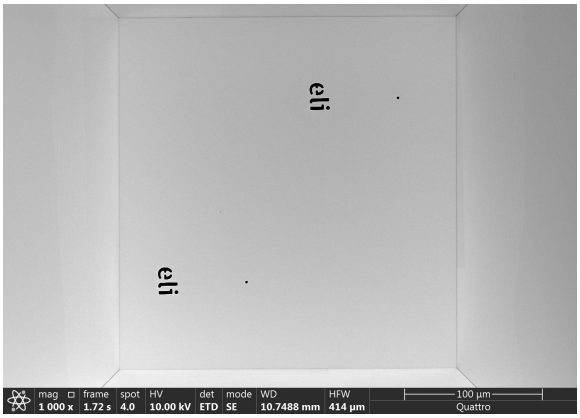

(a) Full view on the membrane.

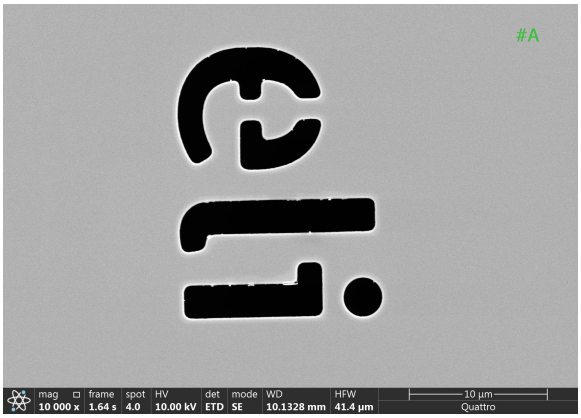

(b) Detail on a one sample.

Fig. 8.2: Binary transmission samples of ELI logo created by technique of FIB milling on silicon nitride with Au coating and characterized by SEM microscopy. The overall sample size is around 20x15 μm.

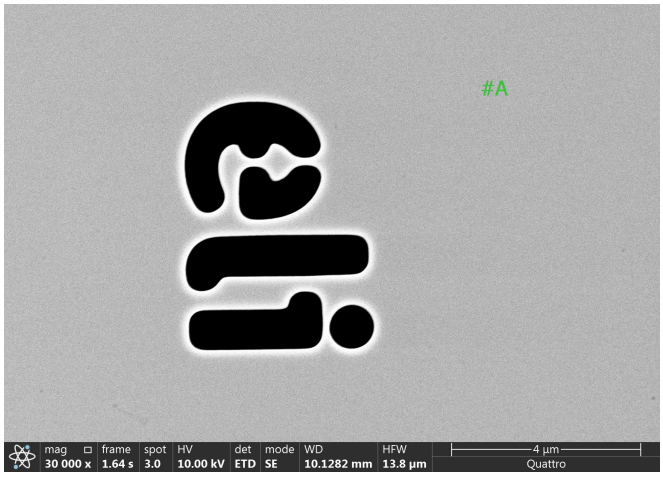

Fig. 8.3: Binary transmission sample of ELI logo created by technique of FIB milling on silicon nitride with Au coating and characterized by SEM microscopy. The overall sample size is around 6x4 μm.

8.2 Experimental setup of EUV CDI and ptychography

We have performed the experimental measurement of CDI and ptychographic imaging on the HHG Beamline at ELI Beamlines facility, which was introduced in Chapter 7. During this experimental campaign, the generation process was driven by commercial Ti:Sapphire laser system operating at a central wavelength of 795 nm, and the high

harmonics were generated in the Kr gas jet. The experimental setup scheme, illustrated in Figure 8.4, was assembled inside the user's end-station chamber located at the output of the HHG Beamline. This user chamber is designed to atomic, molecular, and optical science experiments and coherent diffraction imaging [131]. The picture of the real experimental setup is presented in Fig. 8.5, with a detailed view of the samples shown in Fig. 8.6.

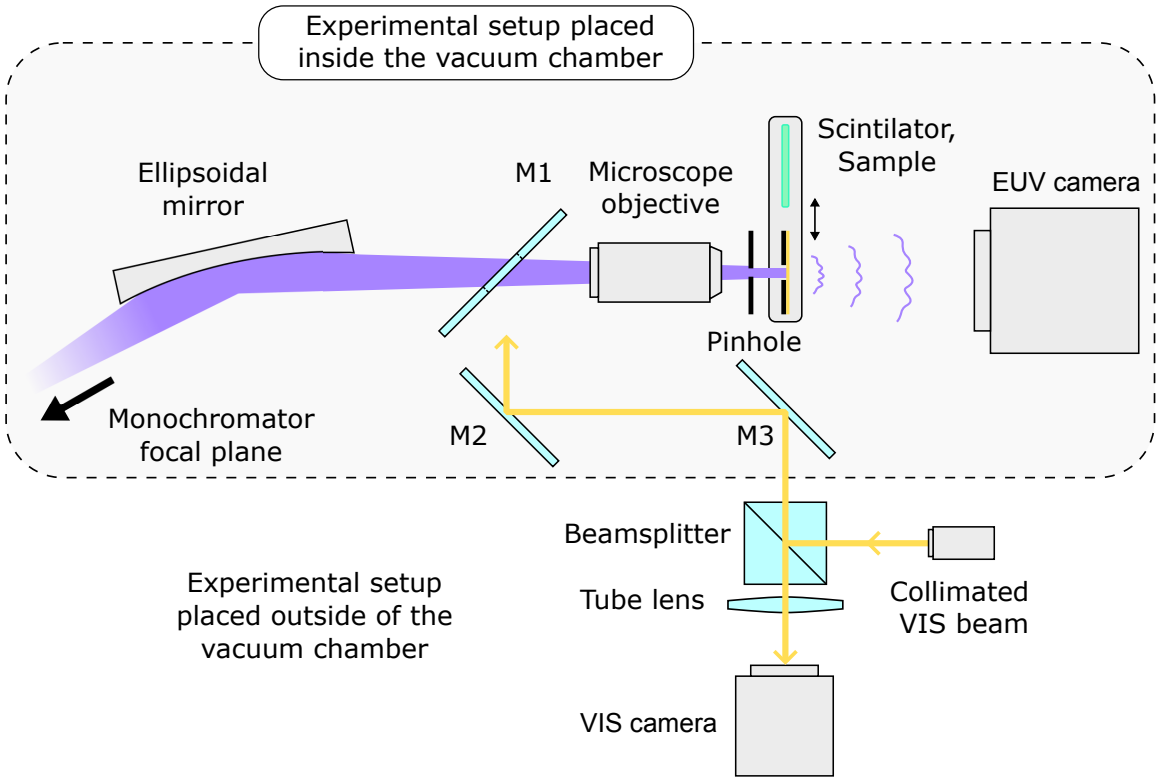

Fig. 8.4: Schematic of the experimental setup for EUV ptychography, where M1-M3 represent planar mirrors, with M1 and the microscope objective having a drilled hole.

The main optical component used to concentrate EUV light onto the sample is an ellipsoidal mirror with gold coating operating under a grazing angle of 5 degrees. This mirror is specifically designed to operate together with the monochromator. The intermediate focal plane of the monochromator is imaged onto the sample by the ellipsoidal mirror, with a demagnification ratio of 5. The sample is placed at a distance of 500 mm from the ellipsoidal mirror, at the location of its second focal distance.

As could be seen from measured HH beam wavefront in Fig. 7.6, the focal spot size of the ellipsoidal mirror is influenced by significant astigmatism in the generated HH beam. Moreover, there are additional aberrations arising from the monochromator EUV optics. Therefore, to filter the probe beam wavefront, a pinhole was positioned at the focal spot of the ellipsoidal mirror to improve a probe beam for ptychography. In the case of CDI, the pinhole was not used in the focal plane since successful reconstruction

was achieved without its presence, primarily due to the use of a much smaller sample compared to the probe beam. The need for employing a pinhole arose later during the ptychographic measurements.

Next, in order to achieve precise sample alignment on the EUV beam axis, an infinity-corrected microscope equipped with a Ce:YAG scintillator was assembled. The setup of the microscope is described in the following section.

The diffraction patterns were recorded using a back-illuminated, water-cooled vacuum EUV CCD camera (Princeton Instruments PI-MTE:2048B) with a pixel size of 13.5 μm. The camera was positioned at a distance ranging from 50 to 120 mm behind the sample. The exposure time was carefully chosen to avoid overexposure of the central part (0-th order) of the diffraction pattern. Typically, the exposure durations varied between 1 to 30 seconds.

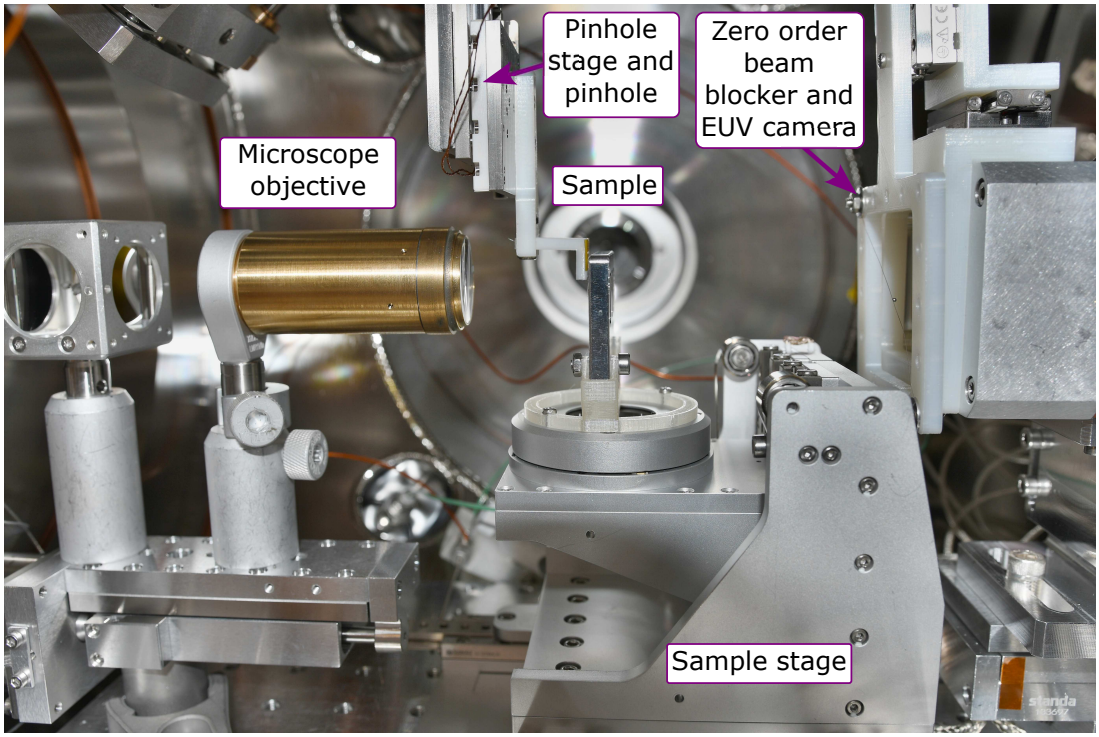

Fig. 8.5: Picture of the experimental setup for EUV coherent diffractive imaging and ptychography placed in the vacuum chamber.

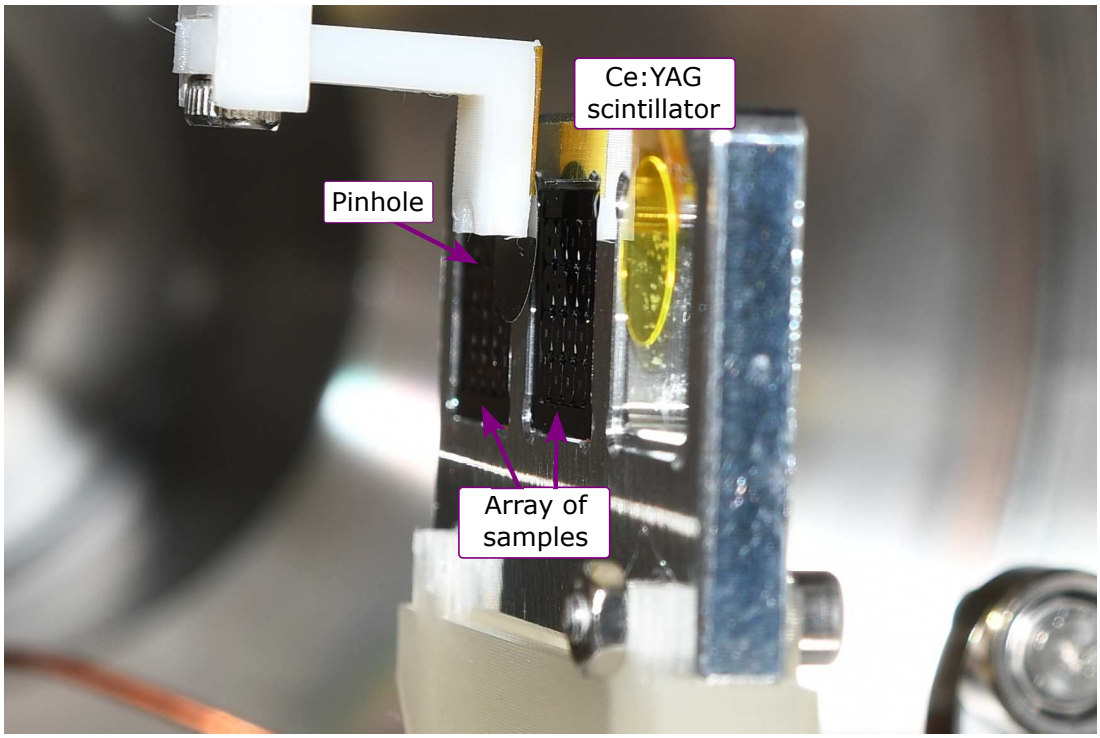

Fig. 8.6: Detail on samples, Ce:YAG scintilator, and a pinhole used for the EUV ptychography.

8.2.1 Zero-order beam block

In many experimental setups of coherent diffractive imaging, zero-order beam blocks are used to suppress low spatial frequencies [75]. This is done to prevent the camera from saturation by intense low-frequency part of the diffraction pattern. Thus, enabling a longer exposure time for image recording, which allows for the detection of higher spatial frequencies with very low intensity. This approach helps to increase the dynamic range of the camera and improve the signal-to-noise ratio. The higher spatial frequencies are essential for capturing fine image details.

8.2.2 EUV focal spot alignment diagnostic

The knowledge of the EUV focal spot intensity profile and its position is crucial for many experiments. However, the available offline methods, such as focal spot imprints [132], are rather impractical. The main challenge of EUV focal spot diagnostics lies in the extremely small size of the focal spot, typically of the order of micrometers, and the high energy density associated with it.

In this section, we present a real-time EUV focal spot diagnostic. In this technique, the EUV beam is directly focused on a Ce:YAG crystal scintillator, which converts EUV radiation into the visible spectral region. The resulting visible light is subse-

quently visualized using an infinity corrected microscope. The experimental design of the infinity-corrected microscope consists of a microscope objective and a tube lens [129], as illustrated in Fig. 8.7 and is described in detail in Appendix A. It is important to note that scintillator crystal exhibit nonlinear response, especially when saturation is reached [133].

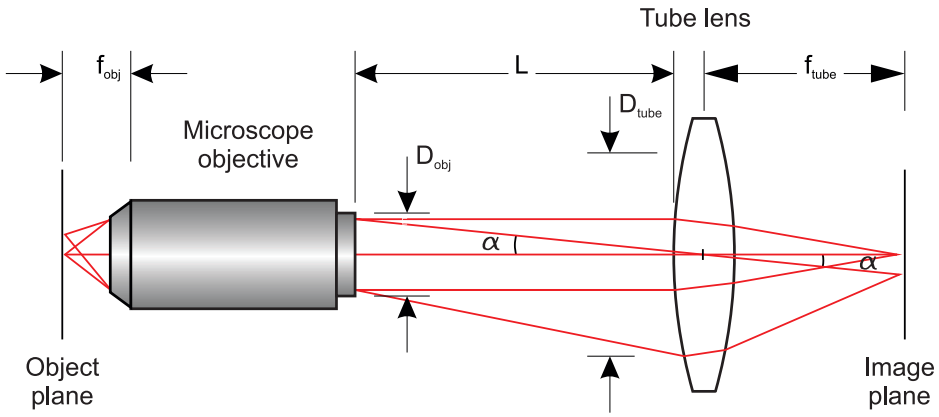

Fig. 8.7: The scheme of an infinity-corrected microscope which consists of a microscope objective and a tube lens.

In our case, we employed this diagnostics technique to accurately determine the position of the focal spot. As a result, it allowed us to align the sample precisely into the interaction region. Let us summarize, the main advantages of the infinity-corrected microscope for our purposes:

- Magnification is only given by the microscope objective focal length and the tube lens focal length.
- There is no fixed distance requirement between the microscope objective and the tube lens. This flexibility allows us to overcome mechanical constraints in the setup by placing only the microscope objective inside the vacuum chamber.
- Additional optical components can be inserted between the objective and tube lens. In our case, we have incorporated a beamsplitter to introduce the illumination beam.

8.3 The optical simulation of focusing by ellipsoidal mirror

The performance of the overall EUV optical setup, including the effects of the monochromator optics and the ellipsoidal mirror used for focusing the beam onto the sample, was investigated by ray tracing simulation. All input parameters used in the simulation

were based on the real setup described in Chapter 7. The results of the simulation are depicted in Fig. 8.8. It is evident that the focal spots meet diffraction limited imaging, even for off-axis object points that are laterally positioned 1 mm from the optical axis in the source generating high harmonics (this upper limit assumes that the source diameter is less than 2 mm). The diffraction limit of the system was found to be around 5 μm, indicating that the spot size is mainly determined by the size of the high harmonic source.

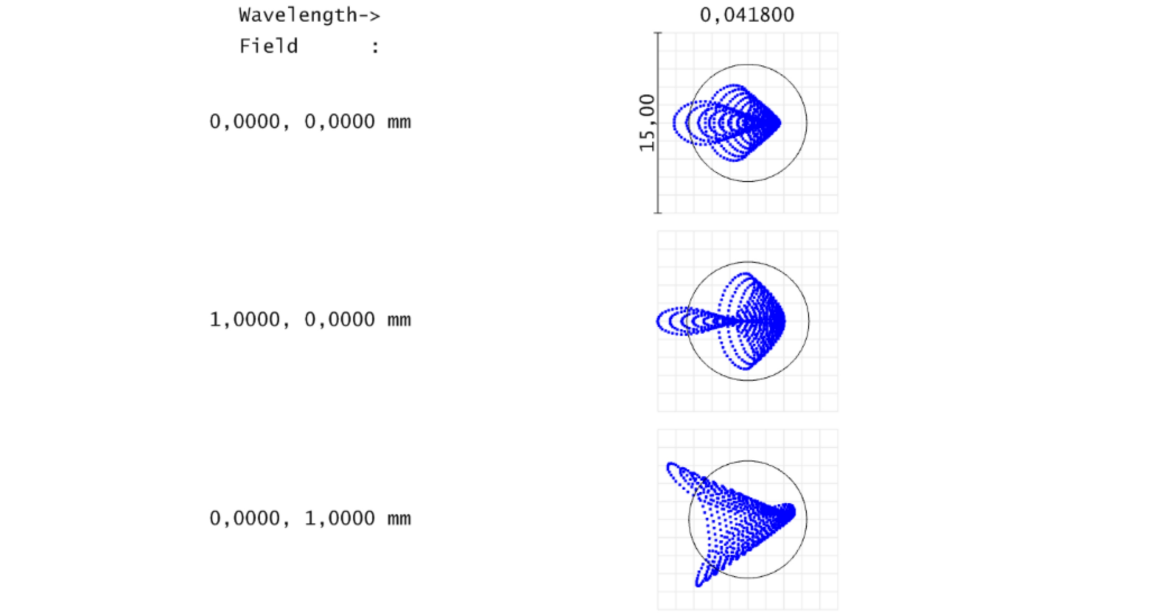

Fig. 8.8: Spot diagram in the focal plane of ellipsoidal mirror including EUV monochromator optical setup. The results are obtained by ray tracing simulations with HH19 (the value of 41.8 nm represents the wavelength of the 19-th harmonic of a fundamental laser beam with a wavelength of 795 nm).

The estimated size of the HH source is approximately 300 μm, which can be determined from the diffraction limit, equation (5.26), of the focused driving beam waist. The HHG driving beam parameters were assumed have a diameter of $D = 32$ mm and a focal length distance of $f = 5$ m. This estimate is a rather upper limit since the generation of high harmonics tends to occur predominantly close to the optical axis, rather than at the radial distance corresponding to the beam waist. Considering that the monochromator demagnification is 2.5 and the ellipsoidal mirror demagnification is 5, it can be determined that the expected upper limit for the EUV focal spot size of

the ellipsoidal mirror is approximately 24 μm. Obviously, the size of such probe beam is not suitable for ptychography imaging a sample that is, in our case, similar in size to the probe. The primary purpose of using a pinhole in the focal plane of the ellipsoidal mirror was to remove optical aberrations and subsequently enhance the quality of the probe beam for ptychography. Additionally, this also helped in slightly reducing the diameter of the probe beam.

8.4 Wavefront of the EUV probe beam filtered by pinhole

The EUV beam probe for ptychography was improved by using a pinhole with a diameter of 10 μm, positioned in the focal plane of the ellipsoidal mirror. The wavefront and intensity profile were measured by a wavefront sensor located at a distance of 690 mm behind the focal plane of the ellipsoidal mirror. The measured intensity profile with the corresponding beam wavefront are shown in Fig. 8.9, where the beam wavefront is plotted after subtracting the effects of tilts and defocus, which are responsible for the beam propagation direction and divergence. It can be observed in Fig. 8.9 that the beam intensity profile has been significantly improved, approaching a nearly Gaussian beam shape. However, the beam wavefront exhibits spherical aberration and coma as the most pronounced optical abberations.

8.4.1 Sample-pinhole distance

When using a pinhole for a beam filtering, it is important to consider the distance between the sample and the pinhole in order to achieve optimal results. Ideally, this distance should be as small as possible. However, in practice, there are technical limitations that need to be taken into account to find an optimal compromise that does not negatively affect the quality of the reconstruction. The sample-pinhole distance should be chosen in the near-field region, and it is recommended that the Fresnel number should satisfy the condition $F > 2$ [134].

In our case, when we proposed to use a pinhole with a diameter of $D = 10$ μm, we can determine the condition for the sample-pinhole distance z_p by readjusting equation (3.19) into following form

$$z_p < \frac{D^2}{2\lambda} \quad . \tag{8.2}$$

Next, by assuming the wavelength of HH19, the condition can be expressed for our particular case as $z_p < 1.2$ mm.

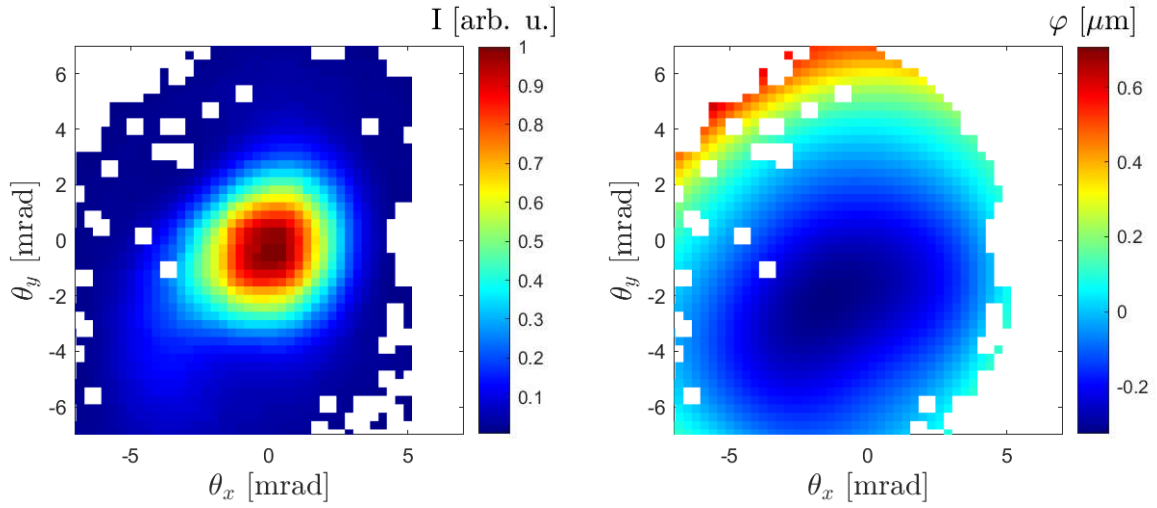

(a) (b)

Fig. 8.9: EUV probe beam intensity profile (a) and the beam wavefront (b) measured at a distance of 690 mm behind the 10 μm pinhole placed in the focal plane of the ellipsoidal mirror. The first few evaluated Zernike coefficients at the central wavelength of HH19 are as follows (except tilts and focus): Astigmatism at 0°: -0.17 μm, Astigmatism at 45°: 0.20 μm, Coma at 0°: 0.45 μm, Coma at 90°: -0.37 μm, 3th order spherical aberration: -0.31 μm.

8.5 Estimate of energy and number of photons incident on sample

We estimated the energy and number of photons incident on the sample by analyzing the intensity profile of the monochromatized EUV beam behind the focal plane of the ellipsoidal mirror. To ensure accurate measurements, we recorded the beam profile within the optimal dynamic range of the camera to avoid saturation. The total energy incident on the camera sensor over the exposure time can be estimated using the following relation

$$E_{total} = N_{counts} \frac{E_{eH} Q_{e^-}}{\mathrm{AD}_{sens} \mathrm{QE}_{\lambda}} \quad , \tag{8.3}$$

where N_{counts} is the total number of counts recorded on camera, E_{eH} is the energy for electron-hole pair creation, Q_{e^-} is the electron charge, AD_{sens} is the analog to digital converter sensitivity, given by the camera manufacturer, and QE_{λ} is the wavelength dependent quantum efficiency. Next, the total number of photons incident on the camera sensor is easily given by

$$N_{ph} = \frac{E_{total}}{E_{ph}} \quad , \tag{8.4}$$

where E_{ph} is the photon energy. The statistic over 5 acquisitions was measured with the back illuminated vacuum EUV CCD camera and evaluated results are shown in Tab. 8.1.

HH order	**Energy** $[\frac{nJ}{1000\ shots}]$ **/ Power** $[nW]$	**Number of photons** $[\frac{10^8}{s}]$
HH17	0.43 ± 0.02	1.00 ± 0.04
HH19	1.53 ± 0.16	3.20 ± 0.30
HH21	0.82 ± 0.08	1.57 ± 0.15
HH23	1.06 ± 0.07	1.84 ± 0.13

Tab. 8.1: The table showing the EUV energy per 1000 shots or EUV power and number of photons incident on the target per second. These values were estimated from the measured EUV beam intensity profile on the CCD camera.

8.6 Experimental results of CDI

In this paragraph, we present the experimental results of CDI reconstruction, which were achieved by illuminating the sample with a monochromatic beam of HH21 (λ_{H21} = 37.9 nm). For the experimental measurements, we have used the ELI logo with approximate dimensions of 6x4 μm (Fig. 8.3). The sample was precisely positioned at the focal spot of the ellipsoidal mirror, and the diffraction patterns were recorded by a detector placed 64 mm behind the sample.

In order to obtain a diffraction pattern with high dynamic range, the zero-order beam stop was utilized. Diffraction patterns were acquired with and without the beam stop, using different exposures to capture both the central part and a good signal at higher spatial frequencies. These acquired patterns were then processed, and a single diffraction pattern was created by combining them, as illustrated in Fig. 8.10. The typical exposure time for the acquiring diffraction patterns with the zero-order beam stop was of the order of seconds, while the exposure time for the diffraction patterns without the beam stop was roughly five times shorter. This technique resulted in a substantial improvement in the dynamic range of the measured diffraction patterns, increasing it by almost one order of magnitude.

The maximal spatial frequency obtained by the system, according to the relation 5.29, was roughly 5600 lines/mm. Therefore, the expected theoretical resolution from relation 5.28 should be roughly 180 nm.

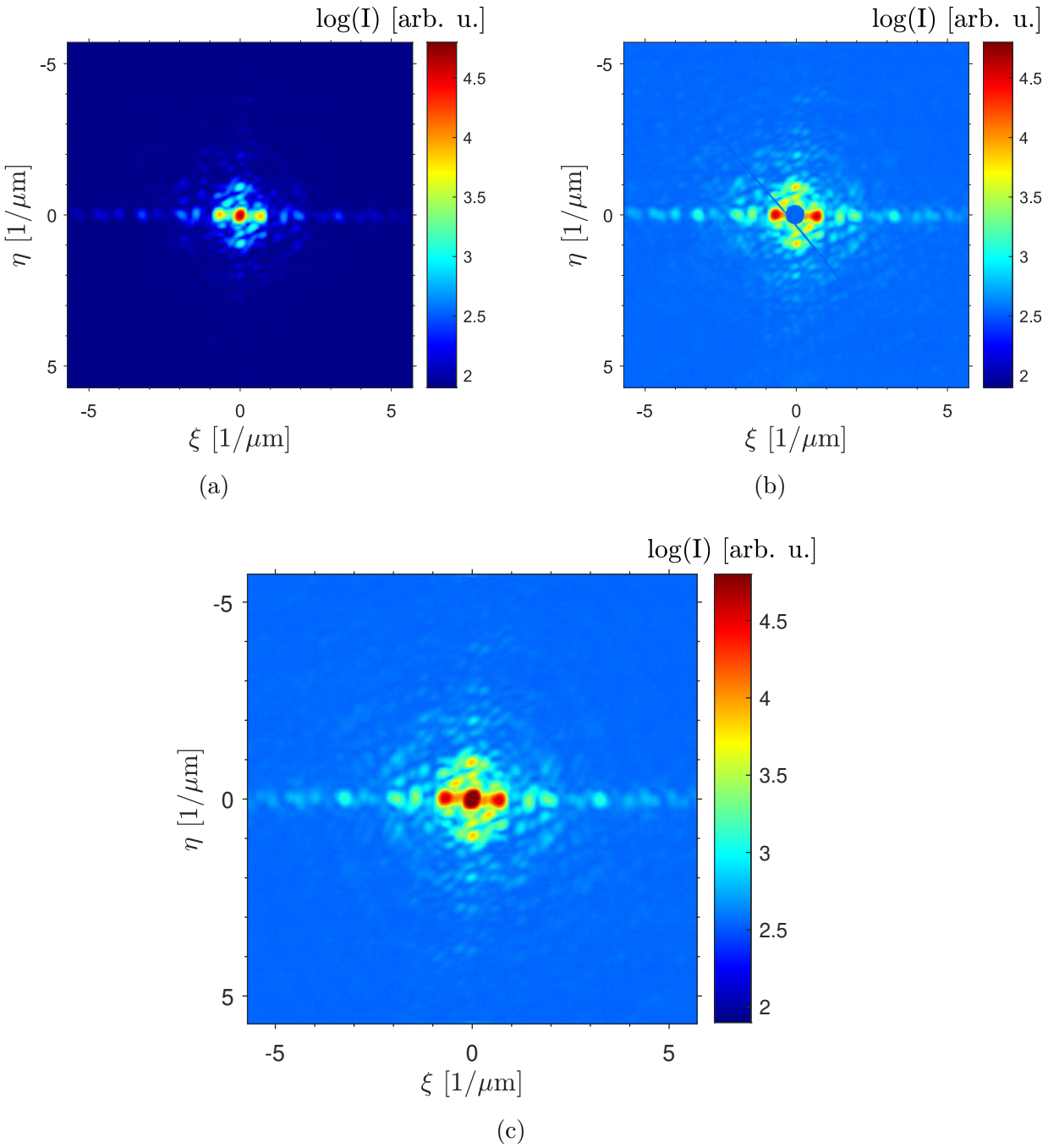

Fig. 8.10: Diffraction patterns observed from the diffraction of the HH21 beam on the ELI logo with approximate dimensions of 6x4 μm (Fig. 8.3). (a): Diffraction pattern recorded without the zero-order beam block and short exposure time. (b): Diffraction pattern recorded with the zero-order beam block and long exposure time. (c): The resulting diffraction pattern with high dynamic range obtained by combining (a) and (b).

The image reconstruction was carried out using the Hybrid Input-Output phase

retrieval algorithm implemented by the author of this thesis, as described in Chapter 5. It was found that successful reconstruction required applying the shrink-wrap algorithm strategy (Section 5.1.6) for support constraints and using diffraction pattern with high dynamic range. The resulting image reconstruction reveals a clearly recognizable ELI logo with some imperfections, as can be seen in Fig. 8.11. Obtaining more accurate reconstruction would probably require an even higher dynamic range of the input diffraction pattern.

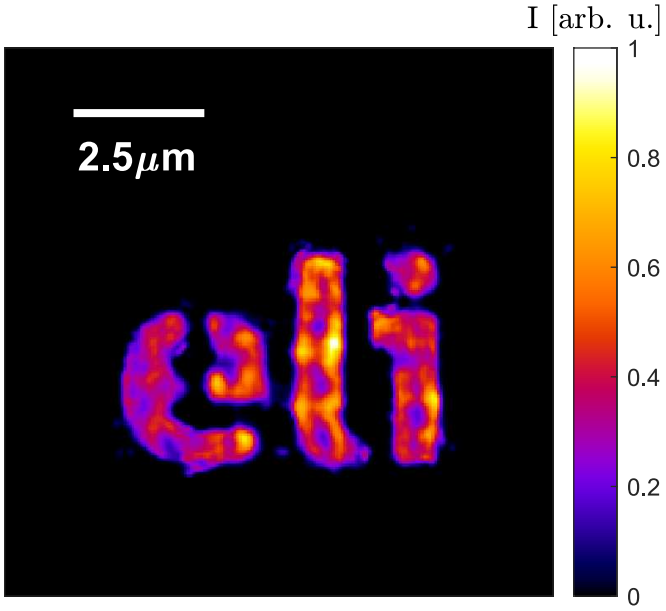

Fig. 8.11: Image retrieved using the HIO algorithm from the diffraction pattern with high dynamic range (two diffraction patterns with short and long exposure were combined). The test sample was irradiated with the HH21 beam ($\lambda_{H21} = 37.9$ nm).

8.7 Experimental results of multi-color EUV ptychography

In the multi-color EUV ptychographic measurements, a rectangular scanning pattern was chosen, and different scanning parameters were tested. The ptychographic scans were also performed without using the zero-order beam block. The best reconstruction was achieved using the following parameters:

- **Rectangular scanning grid size:** 12x12 steps
- **Step size in x-axis:** 2 μm
- **Step size in y-axis:** 2 μm
- **Sample-pinhole distance:** 1170 μm
- **Sample-detector distance:** 95 mm
- **Sample:** ELI logo with approximate dimensions of 20x15 μm (Fig. 8.2)

This configuration allows for a total area coverage of 24x24 μm. The probe scanning overlap in this specific case can be determined from equation (5.22) as 80-87 %, where the probe beam diameter is assumed in the range of 10-15 μm. This value of overlap is rather higher than recommended one, and the main explanation for this is that the success of the reconstruction was not mainly determined by the scanning pattern parameters. Instead, noisy factors that were observed during the scans played a more significant role in the quality of the reconstruction.

Since the ellipsoidal mirror was the main focusing element creating a probe beam together with the pinhole, the relay imaging optics of the monochromator were also necessarily included for the experimental setup of the multi-color ptychography. This is due to the imaging design of the ellipsoidal mirror which required an intermediate focal spot formed by the two toroidal mirrors. To achieve proper imaging without monochromatizing the beam, either the zero-order of a grating or plane mirror with gold coating replacing a grating was used in the monochromator setup.

8.7.1 Scanning pattern

The scanning process involved precise movement of the sample using closed-looped high-precision x-y stages (SmarAct, SLC-24150-D-S-HV). This approach simplifies the experimental setup by allowing for scanning the sample while keeping the probe beam fixed. The readout scan positions obtained from translation stages are depicted in Fig. 8.12, showing a 12x12 grid scanning pattern with a step size of 2 μm. At a closer look, it can be seen that the readout positions, in some cases, do not exactly correspond

to the desired step size of 2 μm. This discrepancy could be caused by factors such as the performance of the in-house developed control system or inappropriate parameter settings for the stage controlling.

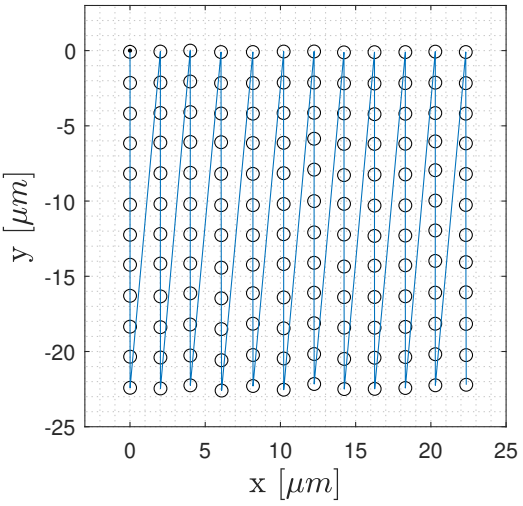

Fig. 8.12: The scanning pattern for EUV ptychography was plotted using the readout positions from closed-loop translation stages. The scanning process started at the coordinate origin.

8.7.2 Image reconstruction

The measured experimental multi-color diffraction patterns were subjected to processing and reconstruction. For the multi-color reconstruction, we utilized the PIM algorithm based on a variant of the ePIE, which was developed at the University of California (UCLA) [12, 13].

After optimizing the necessary parameters and precisely adjusting the sample-detector distance, the best result for multi-color reconstruction was achieved by using modes from HH15 to HH23. These modes correspond to discrete wavelengths of $\lambda_{H23} = 34.7$ nm, $\lambda_{H21} = 37.9$ nm, $\lambda_{H19} = 41.8$ nm, $\lambda_{H17} = 46.8$ nm, and $\lambda_{H15} = 53.2$ nm (in the case of the fundamental driving beam of 795 nm). The retrieved results are presented in Figs. 8.13, 8.14, 8.15, 8.16, and 8.17.

The best image reconstructions was achieved with the central mode HH19, which can be attributed to its high flux compared to the other modes. This result shows the importance of the intensity of each mode in multi-color ptychographic reconstructions. The low intensity modes have a very poor contribution to the resulting superimposed diffraction pattern, which means that the signal-to-noise ratio for these individual modes is low.

The theoretical resolution expected with the wavelength of HH19 from relation 5.28 should be approximately 290 nm for the maximum spatial frequency of 3500 lines/mm,

as determined by the setup geometry and derived from equation 5.29.

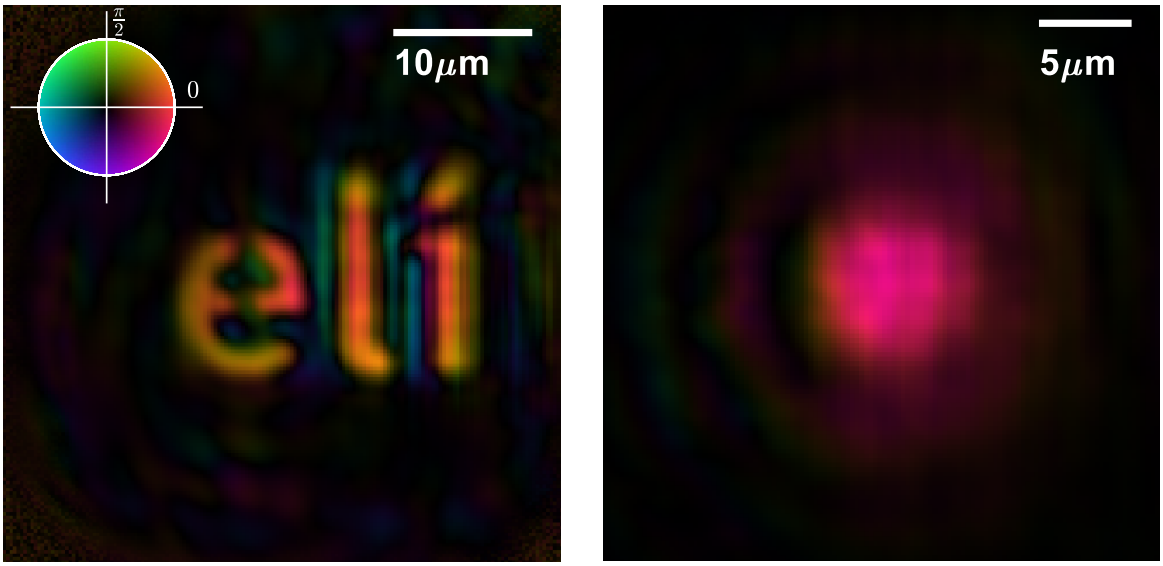

(a) (b)

Fig. 8.13: Multi-color ptychographic image (a) and probe beam (b) reconstruction of the ELI logo sample in the complex representation with the color wheel same for both images. The result obtained using the HH23 mode at the wavelength $\lambda_{H23} = 34.7$ nm.

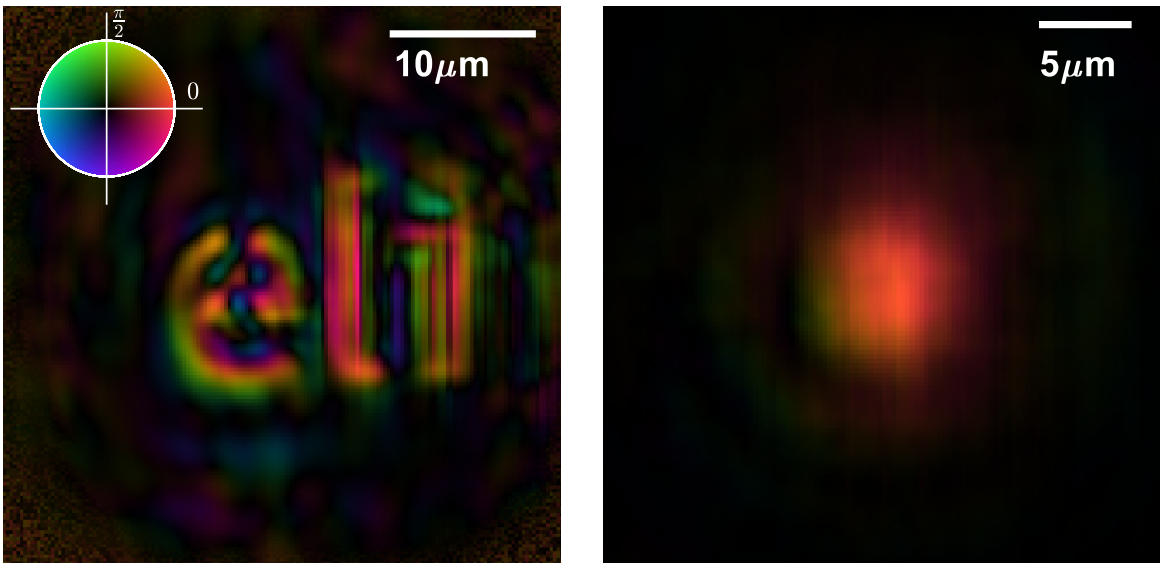

(a) (b)

Fig. 8.14: Multi-color ptychographic image (a) and probe beam (b) reconstruction of the ELI logo sample in the complex representation with the color wheel same for both images. The result obtained using the HH21 mode at the wavelength $\lambda_{H21} = 37.9$ nm.

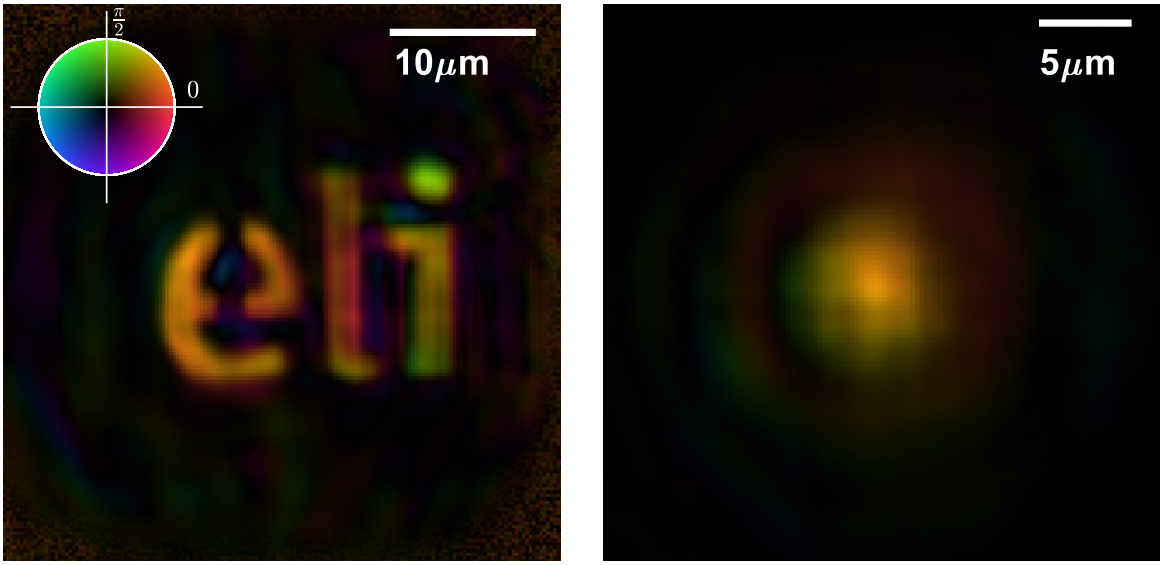

(a) (b)

Fig. 8.15: Multi-color ptychographic image (a) and probe beam (b) reconstruction of the ELI logo sample in the complex representation with the color wheel same for both images. The result obtained using the HH19 mode at the wavelength $\lambda_{H19} = 41.8$ nm.

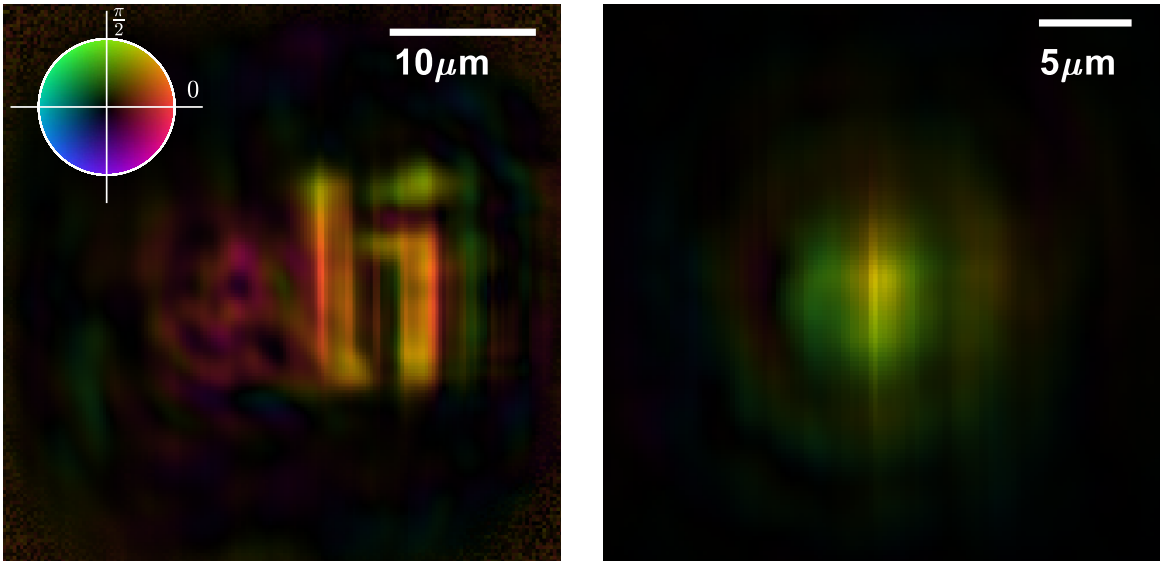

(a) (b)

Fig. 8.16: Multi-color ptychographic image (a) and probe beam (b) reconstruction of the ELI logo sample in the complex representation with the color wheel same for both images. The result obtained using the HH17 mode at the wavelength $\lambda_{H17} = 46.8$ nm.

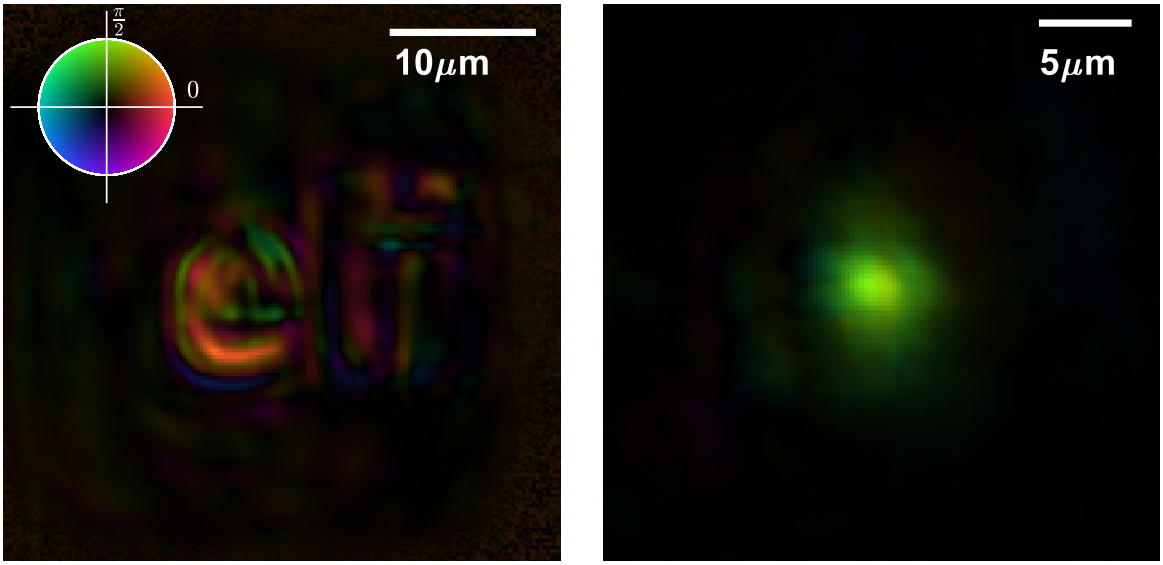

(a) (b)

Fig. 8.17: Multi-color ptychographic image (a) and probe beam (b) reconstruction of the ELI logo sample in the complex representation with the color wheel same for both images. The result obtained using the HH15 mode at the wavelength $\lambda_{H15} = 53.2$ nm.

8.7.3 Retrieved spectral weights

In Fig. 8.18, the retrieved spectral weights of HH15 to HH23 are presented, along with a comparison to the measured HH spectrum. While the reconstructed spectrum does not perfectly match the measured spectrum, the overall shape is roughly correct, demonstrating the proof of principle of the multi-color ptychographic reconstruction method.

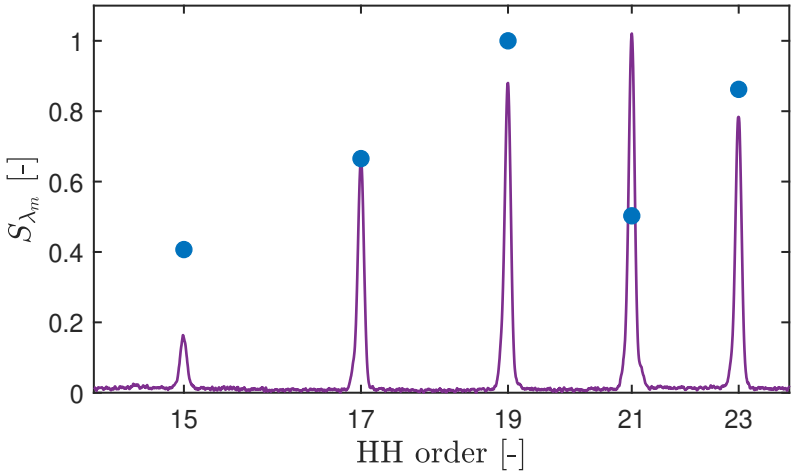

Fig. 8.18: Retrieved spectral weights (blue circles) of multi-color ptychographic reconstruction with a comparison to the measured HH spectrum by the in-built EUV spectrometer (solid purple line).

8.8 Discussion of potential errors in experimental results of EUV CDI and ptychography

During the experimental measurement and data treatment, several potential errors were observed that could limit the accuracy of the reconstruction.

- **Low dynamic range of the camera**, the central high-intensity region caused overexposure and loss of information, specifically the low-intensity high-angle diffracted signals, in the recorded diffraction patterns. One potential solution could be to use recently introduced scientific CMOS detectors designed for soft X-ray applications [135]. These detectors offer both a high dynamic range and a high signal-to-noise ratio.

- **Fluctuations in the source**, both in terms of intensity and positions, could have introduced changes in the recorded diffraction patterns, leading to potential artifacts in the reconstruction. The longtime drift during the data acquisition, lasting for more than 2 hours, was observed.

- **Coupling of the optical breadboard with the vacuum chamber**, which could have resulted in unwanted vibrations or drifts, affecting the stability and consistency of the recorded diffraction patterns.

- **Aberrations introduced by EUV optics** could significantly impact the resulting EUV beam wavefront. These aberrations can arise due to imperfections in the optical components or misalignments in the overall setup. This mainly affects CDI, where perfect wavefront of the probe beam is required.

- **Imprecise positions of sample stages** (ptychography), leading to slight misalignment in the experimental setup and affecting the accuracy of the reconstructed image. One potential way to improve the reconstruction would be to use an algorithm that is capable of correcting positional noise [136, 137].

- **The large size of the probe beam** (ptychography), this size was comparable to the sample size and could cause problems with the reconstructions.

9 Conclusions and future perspectives

This doctoral thesis covered coherence studies of short-wavelength radiation sources using newly proposed techniques. Besides, the thesis aimed to demonstrate the potential applications of this coherent radiation in the field of coherent diffractive imaging techniques.

In the introductory sections, we briefly discussed the most commonly used partially coherent EUV sources for the research concerning short wavelength light-matter interaction. Additionally, we introduced the theory of coherence of electromagnetic radiation, the free-space propagation of both fully and partially coherent light, and the theory of coherent diffractive imaging, which were essential for the objectives of this thesis. We can summarize the achieved experimental results of this thesis in the following main conclusions.

9.1 EUV pulse duration studies of SXRL

We have presented a novel method, which was published in [7], for estimating the pulse duration of partially coherent soft X-ray pulses. It was demonstrated that the far-field intensity patterns contain fruitful information about the properties of partially coherent radiation sources. Despite significant shot-to-shot fluctuations of a plasma-based soft X-ray laser that operated below saturation, a clear dependence of the number of longitudinal modes on the gain medium length has been observed. This behavior can be explained by the gain narrowing during amplification, together with pulse shortening because of the speed of travelling wave of pumping pulse and finite gain duration.

By employing a 1D model of radiative transfer and pulse envelope propagation, we successfully disentangled the evolution of both the coherence length and the pulse duration. These values, obtained in a single shot and using our simple method, exhibit strong agreement with those obtained through direct measurements from sources employing the same lasing scheme and similar pumping conditions. While the method was initially tested on the output of a specific transient SXRL, we are confident in its potential effectiveness for any partially coherent source of radiation.

9.2 Spatial coherence by a non-redundant multi-aperture arrays

Next, we proposed and experimentally verified another new method for the single-shot measurement of spatial coherence, with results being currently submitted for publication. The method eliminates the need for any a priori assumptions about coherence or intensity distribution. To achieve this, we developed a spatial coherence retrieval algorithm that was tested through simulations and subsequently applied for evaluating experimental results.

We demonstrated the efficiency of this method through the measurement of both 1D and 2D degrees of spatial coherence for a plasma-based soft X-ray laser. The significant asymmetry observed in the spatial coherence function of the beam demonstrated that the commonly used Gaussian Schell beam model is not a sufficiently accurate description. It is believed that this method can measure the spatial coherence of X-ray radiation sources with high intensity profile fluctuations which was not achievable yet.

9.3 EUV coherent diffractive imaging and ptychography

In Chapter 8, we have described the experimental realization and results of EUV lensless imaging methods. The reconstruction of the microscopic test sample was successfully achieved using both coherent diffractive imaging technique and multi-color ptychography with the EUV beam generated by the HHG Beamline. In the context of the CDI imaging technique, the integration of the monochromator into the HHG Beamline setup was crucial.

The lensless imaging methods and their results presented in this work represented the first experimental implementation at ELI Beamlines. This demonstration confirmed the feasibility of using HHG Beamlines at this unique facility as a convenient source for such imaging methods.

9.4 Future perspectives

The main future perspective relies on demonstrated imaging techniques of coherent diffractive imaging and ptychography in the EUV spectral region. Firstly, some improvements to the current experimental setup are necessary to enhance the quality of the reconstructed images. Notably, enhancing the accuracy and reliability of sample positioning emerges as a critical aspect. It is essential to mitigate the influence of vibrations by decoupling the experimental setup from the vacuum chamber. Additionally, to improve the quality of ptychographic imaging, a smaller probe beam and an

enhanced signal-to-noise ratio would be necessary.

In the near future, we believe that the ongoing development of laboratory sources, such as the HHG, could potentially serve as suitable sources for advanced EUV coherent diffractive imaging and ptychography. These techniques, in conjunction with the HHG Beamline, could show potential in fields such as materials science and biology, and they could even find application in implementing pump-probe imaging experiments.

Bibliography

[1] D. Attwood, *Soft X-Rays and Extreme Ultraviolet Radiation: Principles and Applications*, Cambridge University Press, Cambridge, 1999.

[2] B. J. Rice, *Extreme ultraviolet (EUV) lithography*, Nanolithography, Woodhead Publishing, Oxford, pp. 42–79, 2014.

[3] F. Paresce, S. Kumar, and C. S. Bowyer, *Continuous Discharge Line Source for the Extreme Ultraviolet*, Applied Optics, Vol. 10, No. 8, p. 1904, 1971.

[4] B. W. J. McNeil and N. R. Thompson, *X-ray free-electron lasers*, Nature Photonics, Vol. 4, No. 12, pp. 814–821, 2010.

[5] J. J. Rocca, *Table-top soft x-ray lasers*, Review of Scientific Instruments, Vol. 70, No. 10, pp. 3799–3827, 1999.

[6] H. Daido, *Review of soft x-ray laser researches and developments*, Reports on Progress in Physics, Vol. 65, No. 10, p. 1513, 2002.

[7] M. Albrecht, M. Kozlova and J. Nejdl, *Pulse duration of a partially coherent soft X-ray laser estimated from far-field speckle statistics*, Optics Letters, Vol. 43, No. 19, pp. 4586–4589, 2018.

[8] Ch. Rydberg and J. Bengtsson, *Numerical algorithm for the retrieval of spatial coherence properties of partially coherent beams from transverse intensity measurements*, Optics Express, Vol. 15, No. 21, p. 13613, 2007.

[9] J. R. Fienup, *Phase retrieval algorithms: a comparison*, Applied Optics, Vol. 21, No. 15, p. 2758, 1982.

[10] J. R. Fienup, *Reconstruction of an object from the modulus of its Fourier transform*, Optics Letters, Vol. 3, No. 1, pp. 27–29, 1978.

[11] R. W. Gerchberg and W. O. Saxton, *A Practical Algorithm for the Determination of Phase from Image and Diffraction Plane Pictures*, Optik, Vol. 35, No. 2, pp. 237–246, 1972.

[12] N. Pham, A. Rana, J. Miao, and S. Osher, *Semi-implicit relaxed Douglas-Rachford algorithm (sDR) for ptychography*, Optics Express, Vol. 27, No. 22, pp. 31246–31260, 2019.

[13] A. Rana, J. Zhang, M. Pham, A. Yuan, Y. H. Lo, H. Jiang, S. J. Osher, and J. Miao, *Potential of Attosecond Coherent Diffractive Imaging*, Physical Review Letters, Vol. 125, No. 8, p. 086101, 2020.

[14] C. Evain, C. Szwaj, E. Roussel, J. Rodriguez, M. Le Parquier, M.-A. Tordeux, F. Ribeiro, M. Labat, N. Hubert, J.-B. Brubach, P. Roy, and S. Bielawski, *Stable coherent terahertz synchrotron radiation from controlled relativistic electron bunches*, Nature Physics, Vol. 15, pp. 635–639, 2019.

[15] K. Wille, *Synchrotron radiation sources*, Reports on Progress in Physics, Vol. 54, No. 8, pp. 1005–1067, 1991.

[16] M. Eriksson, J. Friso van der Veen, and Ch. Quitmann, *Diffraction-limited storage rings – a window to the science of tomorrow*, Journal of Synchrotron Radiation, Vol. 21, No. 5, pp. 837–842, 2014.

[17] S. Shin, *New era of synchrotron radiation: fourthgeneration storage ring*, AAPPS Bulletin, Vol. 31, No. 21, 2021.

[18] C. Pellegrini, *X-ray free-electron lasers: from dreams to reality*, Physica Scripta, Vol. T169, p. 014004, 2016.

[19] G. Dattoli, M. Del Franco, M. Labat, P. L. Ottaviani and S. Pagnutti, *Introduction to the Physics of Free Electron Laser and Comparison with Conventional Laser Sources*, Free Electron Lasers, Intech Publisher, Croatia, 2012.

[20] R. Huang, W. Li, Z. Zhao, H. Li, J. Wang, T. Ma, Q. Huang, Z. He, Q. Jia, L. Wang, and Y. Lu, *Design of a Pre-Bunched THz Free Electron Laser*, Particles, Vol. 1, No. 1, pp. 267–278, 2018.

[21] B. McNeil, *First light from hard X-ray laser*, Nature Photonics, Vol. 3, No. 7, pp. 375–377, 2009.

[22] E. Allaria, R. Appio, L. Badano, W. A. Barletta, S. Bassanese, S. G. Biedron, A. Borga, E. Busetto, D. Castronovo, P. Cinquegrana, S. Cleva, D. Cocco, M. Cornacchia, P. Craievich, I. Cudin, G. D'Auria, M. Dal Forno, M. B. Danailov, R. De Monte, G. De Ninno, et al., *Highly coherent and stable pulses from the FERMI seeded free-electron laser in the extreme ultraviolet*, Nature Photonics, Vol. 6, No. 10, pp. 699–704, 2012.

[23] S. Ghimire, D. DiChiara, E. Sistrunk, P. Agostini, L. F. DiMauro, and D. A. Reis, *Observation of high-order harmonic generation in a bulk crystal*, Nature Physics, Vol. 7, No. 2, pp. 138–141, 2011.

[24] P. B. Corkum, *Plasma Perspective on Strong-Field Multiphoton Ionization*, Physical Review Letters, Vol. 71, No. 13, pp. 1994–1997, 1993.

[25] P. Gibbon, *Short Pulse Laser Interactions with Matter*, Imperial College Press, London, 2005.

[26] J. L. Krause, K. J. Schafer, and K. C. Kulander, *High-order harmonic generation from atoms and ions in the high intensity regime*, Physical Review Letters, Vol. 68, No. 24, pp. 3535–3538, 1992.

[27] P. B. Corkum, *Plasma Perspective on Strong-Field Multiphoton Ionization*, Physical Review Letters, Vol. 71, No. 13, pp. 1994–1997, 1993.

[28] J. Higuet, *Études structurelles et dynamiques de systèmes atomiques ou moléculaires par génération d'harmoniques d'ordre élevé*, PhD thesis, Université Bordeaux, 2010.

[29] O. Finke, J. Vábek, M. Nevrkla, N. Bobrova, O. Hort, L. Jurkovičová, M. Albrecht, A. Jančárek, F. Catoire, S. Skupin, and J. Nejdl, *Phase-matched high-order harmonics generation in pre-ionized noble gases*, Scientific Reports, Vol. 12, No. 7715, 2022.

[30] A. Paul, R. A. Bartels, R. Tobey, H. Green, S. Weiman, I. P. Christov, M. M. Murnane, H. C. Kapteyn, and S. Backus, *Quasi-phase-matched generation of coherent extreme-ultraviolet light*, Nature, Vol. 421, No. 6918, pp. 51–54, 2003.

[31] V. V. Strelkov and R. A. Ganeev, *Quasi-phase-matching of high-order harmonics in plasma plumes: theory and experiment*, Optics Express, Vol. 25, No. 18, pp. 21068–21083, 2017.

[32] T. H. Maiman, *Optical and Microwave-Optical Experiments in Ruby*, Physical Review Letters, Vol. 4, No. 11, pp. 564–566, 1960.

[33] D. L. Matthews, P. L. Hagelstein, M. D. Rosen, M. J. Eckart, N. M. Ceglio, A. U. Hazi, H. Medecki, B. J. MacGowan, J. E. Trebes, B. L. Whitten, E. M. Campbell, C. W. Hatcher, A. M. Hawryluk, R. L. Kauffman, L. D. Pleasance, G. Rambach, J. H. Scofield, G. Stone, and T. A. Weaver, *Demonstration of a Soft X-Ray Amplifier*, Physical Review Letters, Vol. 54, No. 2, pp. 110–113, 1985.

[34] R. C. Elton, *X-Ray Lasers*, Academic Press, Boston, 1990.

[35] G. J. Tallents, *The physics of soft x-ray lasers pumped by electron collisions in laser plasma*, Journal of Physics D: Applied Physics, Vol. 36, p. 259, 2003.

[36] O. Guilbaud, A. Klisnick, K. Cassou, S. Kazamias, D. Ros, G. Jamelot, D. Joyeux, and D. Phalippou, *Origin of microstructures in picosecond X-ray laser beams*, Europhysics Letters, Vol. 74, No. 5, p. 823, 2006.

[37] Y. V. Afanas'ev and V. N. Shlyaptsev, *Formation of a population inversion of transitions in Ne-like ions in steady-state and transient plasmas*, Soviet Journal of Quantum Electronics, Vol. 19, No. 12, pp. 1606–1612, 1989.

[38] P. V. Nickles, V. N. Shlyaptsev, M. Kalachnikov, M. Schnürer, I. Will, and W. Sandner, *Short Pulse X-Ray Laser at 32.6 nm Based on Transient Gain in Ne-like Titanium*, Physical Review Letters, Vol. 78, No. 14, pp. 2748–2751, 1997.

[39] M. P. Kalachnikov, P. V. Nickles, M. Schnürer, W. Sandner, V. N. Shlyaptsev, C. Danson, D. Neely, E. Wolfrum, J. Zhang, A. Behjat, A. Demir, G. J. Tallents, P. J. Warwick, and C. L. S. Lewis, *Saturated operation of a transient collisional x-ray laser*, Physical Review A, Vol. 57, No. 6, pp. 4778–4783, 1998.

[40] E. Oliva, M. Fajardo, L. Li, S. Sebban, D. Ros, and P. Zeitoun, *Soft x-ray plasma-based seeded multistage amplification chain*, Optics Letters, Vol. 37, No. 20, p. 4341, 2012.

[41] L. Mandel and E. Wolf, *Optical coherence and quantum optics*, Cambridge University Press, New York USA, 1995.

[42] L. M. Meng, D. Alessi, O. Guilbaud, Y. Wang, M. Berrill, B. M. Luther, S. R. Domingue, D. H. Martz, D. Joyeux, S. De Rossi, J. J. Rocca, and A. Klisnick, *Temporal coherence and spectral linewidth of an injection-seeded transient collisional soft x-ray laser*, Optics Express, Vol. 19, No. 13, pp. 12087–12092, 2011.

[43] O. Guilbaud, F. Tissandier, J-P. Goddet, M. Ribière, S. Sebban, J. Gautier, D. Joyeux, D. Ros, K. Cassou, S. Kazamias, A. Klisnick, J. Habib, P. Zeitoun, D. Benredjem, T. Mocek, J. Nejdl, S. de Rossi, G. Maynard, B. Cros, A. Boudaa, and A. Calisti, *Fourier-limited seeded soft x-ray laser pulse*, Optics Letters, Vol. 35, No. 9, pp. 1326–1328, 2010.

[44] J. W. Goodman, *Speckle Phenomena in Optics: Theory and Applications*, Roberts and Company Publishers, Greenwood village, Colorado, 2007.

[45] M. Born and E. Wolf, *Principles of Optics*, Pergamon Press, London, England, 1980.

[46] P. Fiala and I. Richter, *Fourierovská optika a optické zpracování signálů*, Czech technical university, Faculty of Nuclear Science and Physical Engineering, Prague, 2003.

[47] J. W. Goodman, *Introduction to Fourier Optics*, McGraw-Hill, San Francisco, 1996.

[48] X. Yu, T. Xiahui, Q. Y. Xiong, P. Hao, and W. Wei, *Wide-window angular spectrum method for diffraction propagation in far and near field*, Optics Letters, Vol. 37, No. 23, p. 4943, 2012.

[49] K. Matsushima and T. Shimobaba, *Band-Limited Angular Spectrum Method for Numerical Simulation of Free-Space Propagation in Far and Near Fields*, Optics Express, Vol. 17, No. 22, pp. 19662–19673, 2009.

[50] M. Zhong, *Propagation of partially coherent light in optical systems*, Dissertation, Friedrich-Schiller-Universität, 2017.

[51] A. Starikov and E. Wolf, *Coherent-mode representation of Gaussian Schell-model sources and of their radiation fields*, Journal of the Optical Society of America, Vol. 72, No. 7, pp. 923–928, 1982.

[52] F. Gori, *Collett–Wolf Sources and Multimode Lasers*, Optics Communications, Vol. 34, No. 3, pp. 301–305, 1980.

[53] C. Gutt, P. Wochner, B. Fischer, H. Conrad, M. Castro-Colin, S. Lee, F. Lehmkühler, I. Steinke, M. Sprung, W. Roseker, D. Zhu, H. Lemke, S. Bogle, P. H. Fuoss, G. B. Stephenson, M. Cammarata, D. M. Fritz, A. Robert, and G. Grübel, *Single Shot Spatial and Temporal Coherence Properties of the SLAC Linac Coherent Light Source in the Hard X-Ray Regime*, Physical Review Letters, Vol. 108, No. 2, p. 024801, 2012.

[54] J. W. Goodman, *Statistical Optics 2nd Ed.*, John Wiley & Sons, Canada, 2015.

[55] J. C. Dainty, *The Statistics of Speckle Patterns*, Progress in Optics, Vol. 14, pp. 1–46, 1977.

[56] K. A. Janulewicz, C. M. Kim, and H. Stiel, *Speckle statistics and transverse coherence of an x-ray laser with fluctuations in its active medium*, Optics Express, Vol. 21, No. 3, pp. 3225–3234, 2013.

[57] A. Le Marec, O. Guilbaud, O. Larroche, and A. Klisnick, *Evidence of partial temporal coherence effects in the linear autocorrelation of extreme ultraviolet laser pulses*, Optics Letters, Vol. 41, No. 14, pp. 3387–3390, 2016.

[58] V. N. Shyaptsev, J. Dunn, S. Moon, R. Smith, R. Keenan, J. Nilsen, K. B. Fournier, J. Kuba, A. L. Osterheld, J. J. Rocca, B. Luther, Y. Wang, and M. Marconi, *Numerical studies of transient and capillary x-ray lasers and their applications*, SPIE Proceedings, Soft X-Ray Lasers and Applications V, Vol. 5197, pp. 221–228, 2003.

[59] R. Keenan, J. Dunn, P. K. Patel, D. F. Price, R. F. Smith, and V. N. Shlyaptsev, *High-Repetition-Rate Grazing-Incidence Pumped X-Ray Laser Operating at 18.9 nm*, Physical Review Letters, Vol. 94, No. 10, p. 103901, 2005.

[60] J. Hřebíček, B. Rus, J. C. Lagron, J. Polan, T. Havlíček, T. Mocek, J. Nejdl, and M. Pešlo, *25TW Ti:Sapphire laser chain at PALS*, SPIE Proceedings, SPIE Optics + Optoelectronics, Vol. 8080, p. 80800U, 2011.

[61] J. Tümmler, K. A. Janulewicz, G. Priebe, and P. V. Nickles, *10-Hz grazing-incidence pumped Ni-like Mo x-ray laser*, Physical Review E, Vol. 72, p. 037401, 2005.

[62] J. Nilsen, *Design of a picosecond-laser-driven Ni-like Mo x-ray laser near 20 nm*, Journal of the Optical Society of America B, Vol. 14, No. 6, pp. 1511–1514, 1997.

[63] D. Bleiner, J. E. Balmer, and F. Staub, *Line focusing for soft x-ray laser-plasma lasing*, Applied Optics, Vol. 50, No. 36, pp. 6689–6696, 2011.

[64] L. W. Casperson, *Threshold characteristics of mirrorless lasers*, Journal of Applied Physics, Vol. 48, No. 1, pp. 256–262, 1977.

[65] O. Guilbaud, A. Klisnick, K. Cassou, S. Kazamias, D. Ros, G. Jamelot, D. Joyeux, and D. Phalippou, *Origin of microstructures in picosecond X-ray laser beams*, Europhysics Letters, Vol. 74, No. 5, p. 3387, 2006.

[66] J. A. Koch, B. J. MacGowan, L. B. Da Silva, D. L. Matthews, J. H. Underwood, P. J. Batson, R. W. Lee, R. A. London, and S. Mrowka, *Experimental and theoretical investigation of neonlike selenium x-ray laser spectral linewidths and their variation with amplification*, Physical Review A, Vol. 50, No. 2, pp. 1877–1898, 1994.

[67] J. Nilsen, Y. Li, J. Dunn, T. W. Barbee, and A. L. Osterheld, *Modeling and demonstration of a saturated Ni-like Mo X-ray laser*, Journal de Physique IV France, Vol. 11, p. 67, 2001.

[68] G. J. Linford, E. R. Peressini, W. R. Sooy, and M. L. Spaeth, *Very Long Lasers*, Applied Optics, Vol. 13, No. 2, pp. 379–390, 1974.

[69] H. M. Quiney, *Coherent diffractive imaging using short wavelength light sources*, Journal of Modern Optics, Vol. 57, No. 13, pp. 1109–1149, 2010.

[70] J. Miao, P. Charalambous, J. Kirz, and D. Sayre, *Extending the methodology of X-ray crystallography to allow imaging of micrometre-sized non-crystalline specimens*, Nature, Vol. 400, No. 6742, pp. 342–344, 1999.

[71] J. R. Fienup, *Iterative method applied to image reconstruction and to computer-generated holograms*, Optical Engineering, Vol. 19, No. 3, pp. 297–305, 1980.

[72] D. R. Luke, *Relaxed averaged alternating reflections for diffraction imaging*, Inverse Problems, Vol. 21, No. 1, pp. 37–50, 2005.

[73] V. Elser, I. Rankenburg, and P. Thibault, *Searching with iterated maps*, Proceedings of the National Academy of Sciences, Vol. 104, No. 2, pp. 418–423, 2007.

[74] S. Marchesini, H. He, H. N. Chapman, S. P. Hau-Riege, A. Noy, M. R. Howells, U. Weierstall, and J. C. H. Spence, *X-ray image reconstruction from a diffraction pattern alone*, Physical Review B, Vol. 68, No. 14, p. 140101, 2003.

[75] T. Latychevskaia, *Iterative phase retrieval in coherent diffractive imaging: practical issues*, Applied Optics, Vol. 57, No. 25, p. 7187, 2018.

[76] M. Odstrcil, P. Baksh, S. A. Boden, R. Card, J. E. Chad, J. G. Frey, and W. S. Brocklesby, *Ptychographic coherent diffractive imaging with orthogonal probe relaxation*, Optics Express, Vol. 24, No. 8, p. 8360, 2016.

[77] J. Miao, D. Sayre, and H. N. Chapman, *Phase retrieval from the magnitude of the Fourier transforms of nonperiodic objects*, Journal of the Optical Society of America A, Vol. 15, No. 6, pp. 1662–1669, 1998.

[78] J. R Fienup, *Invariant error metrics for image reconstruction*, Applied Optics, Vol. 36, No. 32, p. 8352, 1997.

[79] W. Hoppe, *Beugung im Inhomogenen Primärstrahlwellenfeld. I. Prinzip einer Phasenmessung von Elektronenbeugungsinterferenzen*, Acta Crystallographica A, Vol. 25, pp. 495–501, 1969.

[80] R. Hegerl and W. Hoppe, *Dynamische Theorie der Kristallstrukturanalyse durch Elektronenbeugung im inhomogenen Primärstrahlwellenfeld*, Berichte der Bunsengesellschaft für physikalische Chemie, Vol. 74, No. 11, pp. 1148–1154, 1970.

[81] P. D. Nellist and J. M. Rodenburg, *Electron Ptychography I: Experimental Demonstration Beyond the Conventional Resolution Limits*, Acta Crystallographica A, Vol. 54, pp. 49–60, 1998.

[82] T. Plamann and J. M. Rodenburg, *Electron Ptychography II: Theory of Three-Dimensional Propagation Effects*, Acta Crystallographica A, Vol. 54, pp. 61–73, 1998.

[83] J. M. Rodenburg and H. M. Faulkner, *A phase retrieval algorithm for shifting illumination*, Applied Physics Letters, Vol. 85, No. 20, pp. 4795–4797, 2004.

[84] H. M. L. Faulkner and J. M. Rodenburg, *Movable Aperture Lensless Transmission Microscopy: A Novel Phase Retrieval Algorithm*, Physical Review Letters, Vol. 93, No. 2, p. 023903, 2004.

[85] A. M. Maiden and J. M. Rodenburg, *An improved ptychographical phase retrieval algorithm for diffractive imaging*, Ultramicroscopy, Vol. 109, No. 10, pp. 1256–1262, 2009.

[86] P. Thibault, M. Dierolf, A. Menzel, O. Bunk, Ch. David, and F. Pfeiffer, *High-Resolution Scanning X-ray Diffraction Microscopy*, Science, Vol. 321, No. 5887, pp. 379–382, 2008.

[87] M. Dierolf, P. Thibault, A. Menzel, C. M. Kewish, K. Jefimovs, I. Schlichting, K. von König, O. Bunk, and F. Pfeiffer, *Ptychographic coherent diffractive imaging of weakly scattering specimens*, New Journal of Physics, Vol. 12, No. 3, p. 035017, 2010.

[88] X. Huang, H. Yan, R. Harder, Y. Hwu, Ian K. Robinson, and Yong S. Chu, *Optimization of overlap uniformness for ptychography*, Optics Express, Vol. 22, No. 10, pp. 12634–12644, 2014.

[89] O. Bunk, M. Dierolf, S. Kynde, I. Johnson, O. Marti, and F. Pfeiffer, *Influence of the overlap parameter on the convergence of the ptychographical iterative engine*, Ultramicroscopy, Vol. 108, No. 5, pp. 481–487, 2008.

[90] R. A. Dilanian, B. Chen, G. J. Williams, H. M. Quiney, K. A. Nugent, S. Teichmann, P. Hannaford, L. V. Dao, and A. G. Peele, *Diffractive imaging using a polychromatic high-harmonic generation soft-x-ray source*, Journal of Applied Physics, Vol. 106, No. 023110, 2009.

[91] B. Abbey, L. W. Whitehead, H. M. Quiney, D. J. Vine, G. A. Cadenazzi, C. A. Henderson, K. A. Nugent, E. Balaur, C. T. Putkunz, A. G. Peele, G. J. Williams, and I. McNulty, *Lensless imaging using broadband X-ray sources*, Nature Photonics, Vol. 5, No. 7, pp. 420–424, 2011.

[92] E. Malm, H. Wikmark, B. Pfau, P. Villanueva-Perez, P. Rudawski, J. Peschel, S. Maclot, M. Schneider, S. Fisebitt, A. Mikkelsen, A. L'Huillier, and P. Johnsson, *Singleshot polychromatic coherent diffractive imaging with a high-order harmonic source*, Optics Express, Vol. 28, No. 1, pp. 394–404, 2020.

[93] D. J. Batey, D. Claus, J. M. Rodenburg, *Information multiplexing in ptychography*, Ultramicroscopy, Vol. 138, pp. 13–21, 2014.

[94] M. Born, E. Wolf, A. B. Bhatia, P. C. Clemmow, D. Gabor, A. R. Stokes, A. M. Taylor, P. A. Wayman, and W. L. Wilcock, *Principles of optics: Electromagnetic theory of propagation, interference and diffraction of light*, Cambridge University Press, 1999.

[95] T. Young, *Experimental Demonstration of the General Law of the Interference of Light*, Philosophical Transactions of the Royal society of London, Vol. 94, pp. 1–16, 1804.

[96] Y. Liu, Y. Wang, M. A. Larotonda, B. M. Luther, J. J. Rocca, and D. T. Attwood, *Spatial Coherence Measurements of a 13.2 nm Transient Nickel-like Cadmium Soft X-ray Laser Pumped at Grazing Incidence*, Optics Express, Vol. 14, No. 26, pp. 12872–12879, 2006.

[97] I. A. Vartanyants, A. Singer, A. P. Mancuso, O. M. Yefanov, A. Sakdinawat, Y. Liu, E. Bang, G. J. Williams, G. Cadenazzi, B. Abbey, H. Sinn, D. Attwood, K. A. Nugent, E. Weckert, T. Wang, D. Zhu, B. Wu, C. Graves, A. Scherz, J. J. Turner, W. F. Schlotter, M. Messerschmidt, J. Lüning, Y. Acremann, P. Heimann, D. C. Mancini, V. Joshi, J. Krzywinski, R. Soufli, M. Fernandez-Perea, S. Hau-Riege, A. G. Peele, Y. Feng, O. Krupin, S. Moeller, and W. Wurth, *Coherence Properties of Individual Femtosecond Pulses of an X-Ray Free-Electron Laser*, Physical Review Letters, Vol. 107, No. 14, p. 144801, 2011.

[98] A. Singer, F. Sorgenfrei, A. P. Mancuso, N. Gerasimova, O. M. Yefanov, J. Gulden, T. Gorniak, T. Senkbeil, A. Sakdinawat, Y. Liu, D. Attwood, S. Dziarzhytski, D. D. Mai, R. Treusch, E. Weckert, T. Salditt, A. Rosenhahn, W. Wurth, and I. A. Vartanyants, *Spatial and temporal coherence properties of single free-electron laser pulses*, Optics Express, Vol. 20, No. 16, p. 17480, 2012.

[99] A. Singer, I. A. Vartanyants, M. Kuhlmann, S. Duesterer, R. Treusch, and J. Feldhaus, *Transverse-Coherence Properties of the Free-Electron-Laser FLASH and DESY*, Physical Review Letters, Vol. 101, No. 25, p. 254801, 2008.

[100] K. A. Nugent and J. E. Trebes, *Coherence measurement technique for short-wavelength light sources*, Review of Scientific Instruments, Vol. 63, No. 4, pp. 2146–2151, 1992.

[101] J. E. Trebes, K. A. Nugent, S. Mrowka, R. A. London, T. W. Barbee, M. R. Carter, J. A. Koch, B. J. MacGowan, D. L. Matthews, L. B. Da Silva, G. F. Stone, and M. D. Feit, *Measurement of the Spatial Coherence of a Soft-X-Ray Laser*, Physical Review Letters, Vol. 68, No. 5, pp. 588–591, 1992.

[102] A. I. González and Y. Mejía, *Nonredundant array of apertures to measure the spatial coherence in two dimensions with only one interferogram*, Journal of the Optical Society of America A, Vol. 28, No. 6, p. 1107, 2011.

[103] Y. Mejía and A. I. González, *Measuring spatial coherence by using a mask with multiple apertures*, Optics Communications, Vol. 273, No. 2, pp. 428–434, 2007.

[104] J. Duarte, A. I. González, R. Cassin, R. Nicolas, M. Kholodstova, W. Boutu, M. Fajardo, and H. Merdji, *Single-shot spatial coherence characterization of x-ray ultrafast sources*, Optics Letters, Vol. 46, No. 7, pp. 1764–1767, 2021.

[105] M. J. E. Golay, *Point arrays having compact, nonredundat autocorrelations*, Journal of the Optical Society of America, Vol. 61, No. 2, pp. 272–273, 1971.

[106] B. Rus, T. Mocek, A. R. Präg, M. Kozlová, G. Jamelot, A. Carillon, D. Ros, D. Joyeux, and D. Phalippou, *Multimillijoule, highly coherent x-ray laser at 21 nm operating in deep saturation through double-pass amplification*, Physical review A, Vol. 66, No. 6, p. 063806, 2002.

[107] J. Polan, T. Mocek, M. Kozlová, P. Homer, and B. Rus, *Spatial and Temporal Profiles of the 21.2-nm Saturated X-Ray Laser Output*, X-Ray Lasers 2006, Springer Proceedings in Physics, Vol. 115, pp. 139–147, 2006.

[108] O. Hort, M. Albrecht, V. E. Nefedova, O. Finke, D. D. Mai, S. Reyné, F. Giambruno, F. Frassetto, L. Poletto, J. Andreasson, J. Gautier, S. Sebban, and J. Nejdl, *High-flux source of coherent XUV pulses for user applications*, Optics Express, Vol. 27, No. 6, pp. 8871–8883, 2019.

[109] U. Even, *The Even-Lavie valve as a source for high intensity supersonic beam*, EPJ Techniques and Instrumentation, Vol. 2, No. 1, 2015.

[110] V. Nefedova, M. Albrecht, and J. Nejdl, *Development of high-flux XUV source based on high-order harmonic generation*, Journal of Electron Spectroscopy and Related Phenomena, Vol. 220, pp. 9–13, 2017.

[111] C. Heyl, H. Coudert-Alteirac, M. Miranda, M. Louisy, K. Kovács, V. Tosa, E. Balogh, K. Varjú, A. L'Huillier, A. Couairon, and C. L. Arnold, *Scale-invariant nonlinear optics in gases*, Optica, Vol. 3, No. 1, pp. 75–81, 2016.

[112] F. Batysta, R. Antipenkov, J. Novák, J. T. Green, J. A. Naylon, J. Horácek, M. Horácek, Z. Hubka, R. Boge, T. Mazanec, B. Himmel, P. Bakule, and B. Rus, *Broadband OPCPA system with 11 mJ output at 1 kHz, compressible to 12 fs*, Optics Express, Vol. 24, No. 16, pp. 17843–17848, 2016.

[113] E. Shirly, G. Neuber, Ch. D. Brooks, B. Besner, M. Hashemi, M. Rübhausen, and J. Andreasson, *User oriented end-station on VUV pump-probe magneto-optical ellipsometry at ELI beamlines*, Applied Surface Science, Vol. 421, pp. 378–382, 2017.

[114] S. Espinoza, F. Samparisi, F. Frassetto, S. Richter, M. Rebarz, O. Finke, M. Albrecht, L. Jurkovičová, O. Hort, N. Fabris, A. Zymaková, D.-D. Mai, R. Antipenkov, J. Nejdl, L. Poletto, and J. Andreasson, *Characterization of the high harmonics source for the VUV ellipsometer at ELI Beamlines*, Journal of Vacuum Science & Technology B, Vol. 38, No. 2, p. 024005, 2020.

[115] A. H. Roos, Z. Hoque, E. Klimešová, L. B. Ltaief, C. Medina, L. Jurkovičová, M. Albrecht, O. Finke, O. Hort, J. Nejdl, M. Mudrich, J. Andreasson, and M. Krikunova, *Electron correlation dynamics in atomic Kr excited by XUV pulses and controlled by NIR laser pulses of variable intensity*, New Journal of Physics, Vol. 25, No. 1, p. 013038, 2023.

[116] A. D. Shiner, B. E. Schmidt, C. Trallero-Herrero, H. J. Wörner, S. Patchkovskii, P. B. Corkum, J.-C. Kieffer, F. Légaré, and D. M. Villeneuve, *Probing collective multi-electron dynamics in xenon with high-harmonic spectroscopy*, Nature Physics, Vol. 7, pp. 464–467, 2011.

[117] F. Calegari, D. Ayuso, A. Trabattoni, L. Belshaw, S. D. Camillis, S. Anumula, F. Frassetto, L. Poletto, A. Palacios, P. Decleva, J. B. Greenwood, F. Martin, and M. Nisoli, *Ultrafast electron dynamics in phenylalanine initiated by attosecond pulses*, Science, Vol. 346, No. 6207, pp. 336–339, 2014.

[118] F. Frassetto, C. Cacho, Ch. A. Froud, I. C. Edmund Turcu, P. Villoresi, W. A. Bryan, E. Springate, and L. Poletto, *Single-grating monochromator for extreme-ultraviolet ultrashort pulses*, Optics Express, Vol. 19, No. 20, pp. 19169–19181, 2011.

[119] L. Poletto, and F. Frassetto, *Single-Grating Monochromators for Extreme-Ultraviolet Ultrashort Pulses*, Applied Sciences, Vol. 3, No. 1, pp. 1–13, 2013.

[120] L. Poletto, and F. Frassetto, *Temporal Response of Ultrafast Grating Monochromators*, Applied Sciences, Vol. 8, No. 1, p. 5, 2018.

[121] L. Poletto, F. Frassetto, and P. Villoresi, *Ultrafast Grating Instruments in the Extreme Ultraviolet*, IEEE Journal of Selected Topics in Quantum Electronics, Vol. 18, No. 1, pp. 467–478, 2012.

[122] L. Poletto, P. Villoresi, E. Benedetti, F. Ferrari, S. Stagira, G. Sansone, and M. Nisoli, *Intense femtosecond extreme ultraviolet pulses by using a time-delay-compensated monochromator*, Optics Letters, Vol. 32, No. 19, pp. 2897–2899, 2007.

[123] L. Poletto, P. Villoresi, F. Frassetto, F. Calegari, F. Ferrari, M. Lucchini, G. Sansone, and M. Nisoli, *Time-delay compensated monochromator for the spectral*

selection of extreme-ultraviolet high-order laser harmonics, Review of Scientific Instruments, Vol. 80, No. 12, p. 123109, 2009.

[124] L. Poletto and F. Frassetto, *Time-preserving grating monochromators for ultrafast extreme-ultraviolet pulses*, Applied Optics, Vol. 49, No. 28, pp. 5465–5473, 2010.

[125] L. Poletto, P. Miotti, F. Frassetto, C. Spezzani, C. Grazioli, M. Coreno, B. Ressel, D. Gauthier, R. Ivanov, A. Ciavardini, M. de Simone, S. Stagira, and G. De Ninno, *Double-configuration grating monochromator for extreme-ultraviolet ultrafast pulses*, Applied Optics, Vol. 53, No. 26, pp. 5879–5888, 2014.

[126] J. Wang, F. Chen, M. Pan, S. Xu, R. Lv, J. Liu, Y. Li, S. Fang, Y. Chen, J. Zhu, D. Zhang, T. Qian, Ch. Yun, K. Zhao, H. Ding, and Z. Wei, *High-flux wavelength tunable XUV source in the 12-40.8 eV photon energy range with adjustable energy and time resolution for Tr-ARPES applications*, Optics Express, Vol. 31, No. 6, pp. 9854–9871, 2023.

[127] M. Golshani and M. Motamedifar, *Impact of aperture thickness on a Fraunhofer diffraction pattern*, Journal of Optics, Vol. 21, No. 4, p. 045605, 2019.

[128] H. N. Chapman, A. Barty, S. Marchesini, A. Noy, and S. P. Hau-Riege, *High-resolution ab initio three-dimensional x-ray diffractoin microscopy*, Journal of the Optical Society of America A, Vol. 23, No. 5, pp. 1179–1200, 2006.

[129] T. S. Tkaczyk, *Field Guide to Microscopy*, SPI PRESS, Bellingham, Washington USA, 2010.

[130] M. Todeschini, A. B. da S. Fanta, F. Jensen, J. B. Wagner, and A. Han, *Influence of Ti and Cr Adhesion Layers on Ultrathin Au Films*, ACS Applied Materials & Interfaces, Vol. 9, No. 42, pp. 37374–37385, 2017.

[131] E. Klimešová, O. Kulyk, Z. Hoque, A. H. Roos, K. P. Khakurel, M. Rebarz, L. Jurkovičová, M. Albrecht, O. Finke, R. Lera, O. Hort, D.-D. Mai, J. Nejdl, M. Sokol, R. B. Fink, L. Ben, D. Westphal, A. Wolf, T. Laštovička, F. Frassetto, L. Poletto, J. Andreasson, and M. Krikunova, *Multipurpose End-Station for Atomic, Molecular and Optical Sciences and Coherent Diffractive Imaging at ELI Beamlines*, The European Physical Journal Special Topics, Vol. 230, No. 23, pp. 4183–4194, 2021.

[132] J. Chalupský, J. Krzywinski, L. Juha, V. Hájková, J. Cihelka, T. Burian, L. Vyšín, J. Gaudin, A. Gleeson, M. Jurek, A. R. Khorsand, D. Klinger, H. Wabnitz, R. Sobierajski, M. Störmer, K. Tiedtke, and S. Toleikis, *Spot size characterization of focused non-Gaussian X-ray laser beams*, Optics Express, Vol. 18, No. 26, pp. 27836–27845, 2010.

[133] J. Krzywinski, A. Andrejczuk, M. Bionta, T. Burian, J. Chalupský, M. Jurek, M. Kirm, V. Nagirnyi, R. Sobierajski, K. Tiedtke, S. Vielhauer, and L. Juha, *Saturation of a Ce:Y3Al5O12 scintillator response to ultra-short pulses of extreme ultraviolet soft X-ray and X-ray laser radiation*, Optical Materials Express, Vol. 7, No. 3, pp. 665–675, 2017.

[134] A. Parsons, *Coherent Diffraction Imaging using a High Harmonic Source at 40 eV*, PhD thesis, University of Southampton, 2014.

[135] C. Léveillé, K. Desjardins, H. Popescu, B. Vondungbo, M. Hennes, R. Delaunay, E. Jal, D. De Angelis, M. Pancaldi, E. Pedersoli, F. Capotondic, and N. Jaouena, *Single-shot experiments at the soft X-FEL FERMI using a back-side-illuminated scientific CMOS detector*, Journal of synchrotron radiation, Vol. 29, No. 1, pp. 103–110, 2022.

[136] A. Maiden, M. Humphry, M. Sarahan, B. Kraus, and J. Rodenburg, *An annealing algorithm to correct positioning errors in ptychography*, Ultramicroscopy, Vol. 120, pp. 64–72, 2012.

[137] F. Zhang, I. Peterson, J. Vila-Comamala, A. Diaz, F. Berenguer, R. Bean, B. Chen, A. Menzel, I. K. Robinson, and J. M. Rodenburg, *Translation position determination in ptychographic coherent diffraction imaging*, Optics Express, Vol. 21, No. 11, p. 13592, 2013.

A Design of the infinity-corrected microscope

The key components of the experimental design of an infinity-corrected microscope consist of a microscope objective and a tube lens [129], as depicted in Fig. A.1. In this design, an object is placed in the focal plane of a specially designed objective, which images the object into infinity. The collimated beam is then focused by the tube lens to create an image in its focal plane where the detector is located.

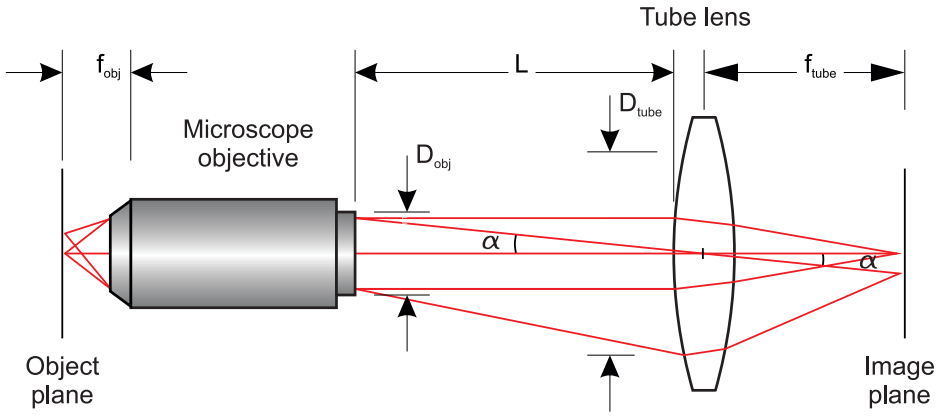

Fig. A.1: The scheme of an infinity-corrected microscope which consists of a microscope objective and a tube lens.

When designing an infinity-corrected microscope, it is crucial to carefully consider the impact of the distance between the microscope objective and the tube lens. If this distance is too large, it can lead to limitations in the field of view due to vignetting. To determine the distance at which vignetting is limited, we need to realize that the object is placed in the focal plane of the microscope objective. In this configuration, all rays behind the objective are parallel but have different angles, which are determined by imaging off-axis points. The maximum angle accepted by the tube lens is determined by the relation

$$\tan \alpha = \frac{D_{tube} - D_{obj}}{2L} \tag{A.1}$$

where D_{tube} is the entrance pupil diameter of the tube lens, D_{obj} is the exit pupil

diameter of the microscope objective, and L is the distance between the tube lens and the microscope objective. Next, one of the parallel rays at an angle α passing through the lens center can be used to determine the relationship for the limit diameter D_{image} in the image plane of the tube lens without vignetting, as follows

$$D_{image} = 2f_{tube} \tan \alpha \quad , \tag{A.2}$$

where f_{tube} is the focal distance of the tube lens. By utilizing the relations above (A.1) and (A.2), we can obtain

$$L \leq \frac{D_{tube} - D_{obj}}{D_{image}} f_{tube} \quad . \tag{A.3}$$

Additionally, we can find the exit pupil diameter of the microscope objective from the definition of numerical aperture

$$D_{obj} = 2f_{obj}\mathrm{NA}_{\mathrm{obj}} \quad . \tag{A.4}$$

The experimental setup of the infinity-corrected microscope used for EUV ptychography is depicted in Fig. 8.4, and a picture of the setup is shown in Fig. 8.5. In our setup, where the sample is observed from the front, a hole has been drilled through the microscope objective to allow the EUV beam to pass through. This configuration enables to observe the EUV focal spot on the Ce:YAG scintillator and keeping the objective fixed in position during the acquisition of diffraction patterns. Additionally, a picture of the part of the experimental setup placed outside the vacuum chamber is presented in Fig. A.2.

The setup of the infinity corrected microscope was designed with the following parameters:

- **Microscope objective:** 10x M Plan Apo Long Working Distance Infinity Corrected, Edmund Optic, NA = 0.28, working distance 33.5 mm
- **Tube lens:** Widefield imaging tube lens TTL200-A, Thorlabs, $f_{tube} = 200$ mm
- **Visible camera:** Monochromatic CCD Allied Vision Manta G-125B 1/3", CCD diagonal of 6 mm, pixel size of 3.75 μm

By considering these parameters, we can calculate the maximum allowable distance between the objective and tube lens according to equation (A.3). It can be shown that the maximal allowable distance is approximately 0.5 m.

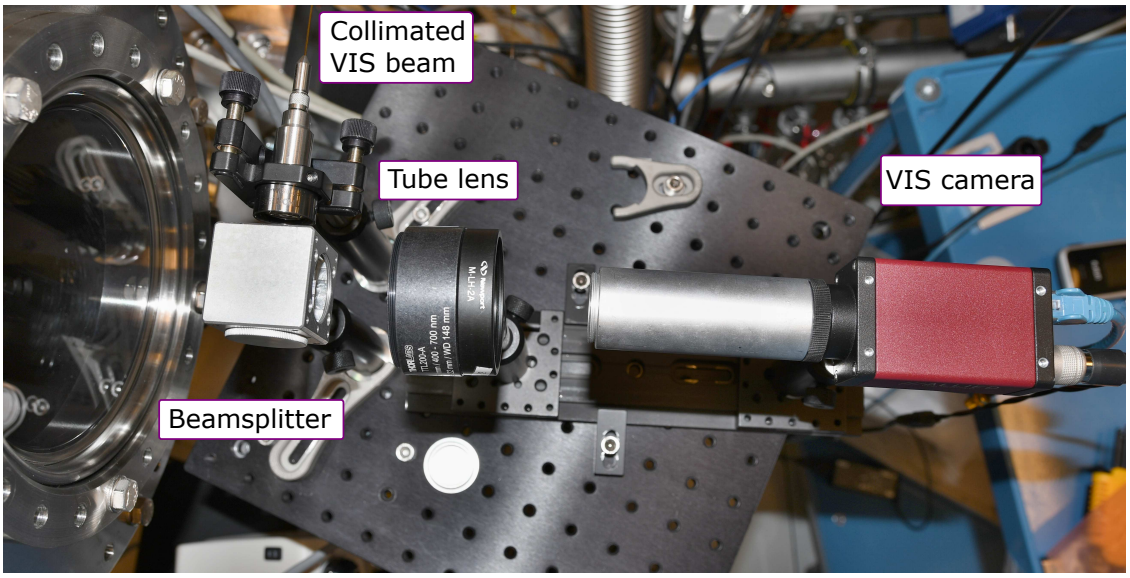

Fig. A.2: Picture of the part of the infinity-corrected microscope placed outside the vacuum chamber.

B List of author's publications

B.1 Publications in peer-reviewed journals

[1] **M. Albrecht**, M. Kozlová, and J. Nejdl, *Pulse duration of a partially coherent soft X-ray laser estimated from far-field speckle statistics*, Optics Letters, Vol. 43, No. 19 , pp. 4586-4589, 2018.

[2] (Submitted article) **M. Albrecht**, O. Hort, M. Kozlová, and J. Nejdl, *Beyond Young's double-slit experiment: Spatial coherence of a soft X-ray source measured in a single-shot*, 2023.

[3] V. Nefedová, **M. Albrecht**, and J. Nejdl, *Development of a high-flux XUV source based on high-order harmonic generation*, Journal of Electron Spectroscopy and Related Phenomena, Vol. 220, pp. 9-13, 2017.

[4] V. E. Nefedová, M. F. Ciappina, O. Finke, **M. Albrecht**, J. Vábek, M. Kozlová, N. Suárez, E. Pisanty, M. Lewenstein, and J. Nejdl, *Determination of the spectral variation origin in high-order harmonic generation in noble gases*, Physical Review A, Vol. 98, No. 3, p. 33414, 2018.

[5] V. E. Nefedová, M. F. Ciappina, O. Finke, **M. Albrecht**, M. Kozlová, and J. Nejdl, *Efficiency control of high-order harmonic generation in gases using driving pulse spectral features*, Applied Physics Letters, Vol. 113, No. 19, p. 191101, 2018.

[6] O. Hort, **M. Albrecht**, V. E. Nefedová, O. Finke, D.-D. Mai, S. Reyné, F. Giambruno, F. Frassetto, L. Poletto, J. Andreasson, J. Gautier, S. Sebban, and J. Nejdl, *High-flux source of coherent XUV pulses for user applications*, Optics Express, Vol. 27, No. 6, pp. 8871-8883, 2018.

[7] J. Nejdl, J. Vančura, K. Boháček, **M. Albrecht**, and U. Chaulagain, *Imaging Michelson interferometer for a low-density gas jet characterization*, Review of Scientific Instruments, Vol. 90, No. 6, 2019.

[8] S. Espinoza, F. Samparisi, F. Frassetto, S. Richter, M. Rebarz, O. Finke, **M. Albrecht**, L. Jurkovičová, O. Hort, N. Fabris, A. Zymaková, D.-D. Mai, R. Antipenkov, J. Nejdl, L. Poletto, and J. Andreasson, *Characterization of the high harmonics source for the VUV ellipsometer at ELI Beamlines*, Journal of Vacuum Science & Technology B, Vol. 38, No. 2, p. 024005, 2020.

[9] E. Klimešová, O. Kulyk, Z. Hoque, A. H. Roos, K. P. Khakurel, M. Rebarz, L. Jurkovičová, **M. Albrecht**, O. Finke, R. Lera, O. Hort, D.-D. Mai, J. Nejdl, M. Sokol, R. B. Fink, L. B. Ltaief, D. Westphal, A. Wolf, T. Laštovička, F. Frassetto, L. Poletto, J. Andreasson, and M. Krikunová, *A Multipurpose End-Station for Atomic, Molecular and Optical Sciences and Coherent Diffractive Imaging at ELI Beamlines*, The European Physical Journal Special Topics, Vol. 230, pp. 4183-4194, 2021.

[10] A. Zymaková, **M. Albrecht**, R. Antipenkov, A. Špaček, S. Karatodorov, O. Hort, J. Andreasson, and J. Uhlig, *First experiments with a water-jet plasma X-ray source driven by the novel high-power-high-repetition rate L1 Allegra laser at ELI Beamlines*, Journal of Synchrotron Radiation, Vol. 28, No. 6, pp. 1778-1785, 2021.

[11] O. Finke, J. Vábek, M. Nevrkla, N. Bobrová, O. Hort, L. Jurkovičová, **M. Albrecht**, A. Jančárek, F. Catoire, S. Skupin, and J. Nejdl, *Phase-matched high-order harmonics generation in pre-ionized noble gases*, Scientific Reports, Vol. 12, No. 7715, 2022.

[12] A. H. Roos, Z. Hoque, E. Klimešová, L. B. Ltaief, C. Medina, L. Jurkovičová, **M. Albrecht**, O. Finke, O. Hort, J. Nejdl, M. Mudrich, J. Andreasson, and M. Krikunová, *Electron correlation dynamics in atomic Kr excited by XUV pulses and controlled by NIR laser pulses of variable intensity*, New Journal of Physics, Vol. 25, No. 013038, 2023.

[13] C. Medina, A. Lægdsmand, L. B. Ltaief, Z. Hoque, A. H. Roos, L. Jurkovičová, O. Hort, O. Finke, **M. Albrecht**, J. Nejdl, F. Stienkemeier, J. Andreasson, E. Klimešová, M. Krikunová, A. Heidenreich, and M. Mudrich, *Long-lasting XUV activation of helium nanodroplets for avalanche ionization*, New Journal of Physics, Vol. 25, No. 053030, 2023.

[14] (Submitted article) L. Jurkovičová, L. B. Ltaief, A. H. Roos, O. Hort, O. Finke, **M. Albrecht**, Z. Hoque, E. Klimešová, A. Sundaralingam, R. Antipenkov, A. Grenfell, A. Špaček, W. Szuba, M. Krikunová, M. Mudrich, J. Nejdl, and J. Andreasson, *Bright continuously-tunable VUV source for ultrafast spectroscopy*, 2023.

[15] (Submitted article) O. Finke, J. Vábek, M. Dvořáček, L. Jurkovičová, **M. Albrecht**, H. Ovcharenko, O. Hort, and J. Nejdl, *Monochromatic high-order harmonic generation by Bessel-Gauss beam in periodically modulated media*, 2023.

B.2 Publications in conference proceedings

[16] **M. Albrecht**, M. Kozlova, and J. Nejdl, *Radiation Properties of Ni-like Molybdenum X-ray Laser at PALS*, Proceedings of SPIE, Vol. 10243, p. 1024310, 2017.

[17] K. Boháček, M. Kozlová, U. Chaulagain, V. Horný, M. Krůs, **M. Albrecht**, and J. Nejdl, *Generation of laser-driven femtosecond electron beams for secondary photon sources with 7 TW Ti-sapphire laser system at PALS*, Proceeding of the 43rd EPS Conference on Plasma Physics, paper P1.079, 2016.

[18] M. Kozlová, J. Nejdl, **M. Albrecht**, S. Sebban, J. Gautier, K. Ta Phuoc, A. Klisnick, A. Le Marec, and F. Tissandier, *Overview of Development of Laser Driven Secondary Sources at PALS and ELI*, X-Ray Lasers 2014, Vol. 169, p. 35, 2016.

[19] J. Nejdl, V. Nefedová, **M. Albrecht**, V. Horny, M. Kozlová, S. Sebban, K. Ta-Phuoc, J. Gautier, and G. Korn, *Laser-driven Short-wavelength Sources at PALS and ELI Beamlines*, High-Brightness Sources and Light-Driven Interactions, Optical Society of America, paper ET2A.4, 2016.

[20] J. Nejdl, M. Kozlová, V. Nefedová, **M. Albrecht**, M. Krůs, J. Gautier, and S. Sebban, *Overview of Laser-Driven Coherent Short-Wavelength Sources at PALS and ELI Beamlines*, Springer Proceedings in Physics, Vol. 202, pp. 3-10, 2018.

[21] J. Nejdl, V. E. Nefedová, D.-D. Mai, N. Nowak, **M. Albrecht**, O. Finke, M. Kozlova, M. F. Ciappina, O. Hort, J. Gautier, S. Sebban, and G. Korn, *User-oriented kHz laser driven sources of XUV and X-rays at ELI Beamlines*, Compact EUV & X-ray Light Sources, paper EW2B.6, 2018.

[22] J. Nejdl, D.-D. Mai, U. Chaulagain, O. Hort, O. Finke, **M. Albrecht**, M. Jurkovič, R. Lera, S. Karatodorov, M. Lamač, J. Vančura, K. Boháček, S. Espinoza, S. Richter, M. Rebarz, E. Klimešová, M. Krikunová, M. Kozlová, R. Antipenkov, F. Batysta, J. Novák, J. T. Green, J. Andreasson, and G. Korn, *Progress on laser-driven X-ray sources at ELI Beamlines*, Proceedings of SPIE, X-ray Lasers and Coherent X-ray Sources: Development and Applications, paper ETh5A.6, 2019.

[23] O. Finke, O. Hort, **M. Albrecht**, V. E. Nefedová, D.-D. Mai, F. Giambruno, S. Reyne, L. Poletto, F. Frassetto, J. Gautier, S. Sebban, R. Antipenkov, F. Batysta, R. Boge, J. Naylon, Z. Hubka, T. Green, P. Bakule, and J. Nejdl, *User-oriented*

high-harmonic source at ELI beamlines, OSA High-brightness Sources and Light-driven Interactions Congress, paper EM2A.2, 2020.

[24] O. Hort, **M. Albrecht**, O. Finke, M Jurkovič, R. Lera, D.-D. Mai, E. Klimešová, S. Espinoza, S. Richter, R. Antipenkov, F. Batysta, J. Novák, J. T. Green, J. Andreasson, M. Krikunová, and J. Nejdl, *ELI beamlines user oriented high-harmonic beamline*, OSA High-brightness Sources and Light-driven Interactions Congress, paper EM2A.2, 2020.

[25] J. Nejdl, U. Chaulagain, O. Hort, D.-D. Mai, R. Lera, S. Karatodorov, **M. Albrecht**, M. Jurkovič, O. Finke, M. Lamač, R. Raclavský, and J. Vábek, *New generation of laser-driven X-ray sources at ELI beamlines*, OSA High-brightness Sources and Light-driven Interactions Congress, paper ETh5A.6, 2020.

[26] S. Espinoza, F. Samparisi, M. Zahradnik, **M. Albrecht**, O. Finke, R. Antipenkov, O. Hort, M. Rebarz, M. Jurkovič, L. Poletto, J. Nejdl, and J. Andreasson, *XUV Reflection and Ellipsometry Experiments at ELIBeamlines*, OSA High-brightness Sources and Light-driven Interactions Congress, paper JW1A.23, 2020.

[27] J. Nejdl, U. Chaulagain O. Hort, D.-D. Mai, **M. Albrecht**, L. Jurkovičová, O. Finke, S. Karatodorov, M. Raclavský, M. Lamač, E. Klimešová, Z. Hoque, A. H. Roos, M. Krikunová, and J. Andreasson, *Update on laser-driven X-ray sources at ELI Beamlines*, Proceedings of SPIE, Vol. 11886, p. 1188608, 2020.

[28] U. Chaulagain, S. Karatodorov, M. Raclavský, S. Lorenz, M. Lamač, **M. Albrecht**, V. Tomkus, J. Dudutis, M. MacKevičiute, P. Gečys, and J. Nejdl, *Tomographic characterization of gas jets for laser-plasma acceleration with increased sensitivity*, Proceedings of SPIE, Vol. 11886, No. 118860A, 2021.

[29] J. Nejdl, U. Chaulagain, O. Hort, D.-D. Mai, **M. Albrecht**, M. Jurkovič, O. Finke, S. Karatodorov, M. Raclavský, M. Lamač, E. Klimešová, Z. Hoque, A. H. Roos, M. Krikunová, and J. Andreasson *Update on laser-driven X-ray sources at ELI Beamlines*, Proceedings of SPIE, Vol. 11886, No. 1188608, 2021.

[30] J. Nejdl, U. Chaulagain, D.-D Mai, O. Hort, M. Lamač, M. Raclavský, **M. Albrecht**, M. Jurkovič, O. Finke, J. Vábek, Y. Pulnova, and S. V. Bulanov, *Update on Laser-driven X-ray Sources at ELI Beamlines*, Optica High-brightness Sources and Light-driven Interactions Congress, paper ETh5A.6, 2022.

[31] O. Finke, J. Vábek, M. Nevrkla, N. Bobrova, O. Hort, M. Jurkovič, **M. Albrecht**, A. Jančárek, F. Catoire, S. Skupin, and J. Nejdl, *Phase-matched absorption-limited HHG using pre-ionization*, The International Conference on Ultrafast Phenomena (UP), paper Th4A.21, 2022.

[32] M. Jurkovič, O. Hort, O. Finke, **M. Albrecht**, A. H. Roos, Z. Hoque, K. Shaw, E. Klimešová, L. B. Ltaief, J. Andreasson, M. Krikunová, M. Mudrich, R. Antipenkov, A. Grenfell, A. Špaček, W. Szuba, and J. Nejdl, *Continuously tunable UV-driven high-intensity HHG source for user applications*, The International Conference on Ultrafast Phenomena (UP), paper Th4A.23, 2022.